



UNIVERSITÀ DEGLI STUDI DI MILANO

FACOLTÀ DI SCIENZE E TECNOLOGIE

Laurea Magistrale in Fisica

Young magnetars: our limited neighborhood UHECR accelerators

Relatore:

Dr. Lorenzo Caccianiga

Correlatore:

Dr. Federico Maria Mariani

Prof. Lino Miramonti

Elaborato di:
Lorenzo Apollonio
Matricola: **08425A**

Anno accademico 2022/2023

Introduction

The *Ultra-High Energy Cosmic Rays* (UHECRs) are the most energetic particles produced in the Universe, with energies higher than 10^{18} eV. One of the main open question in the UHECR physics is what could produce such energetic particles and how. The modern data analyses point out that UHECRs are probably accelerated by astrophysical objects with a optimal combination of magnetic field intensity and dimension. The most likely UHECR accelerators are Active Galactic Nuclei (AGN) and starburst galaxies (SBGs). AGNs are galaxies with an accreting supermassive black hole while SBGs are galaxies with an high rate of star formation and thus of star *death*. This leads to an important density of compact objects, such magnetars, which are a peculiar type of neutron stars with the right features to accelerate UHECRs.

From the data of the Pierre Auger Observatory, which is the largest observatory in the world for UHECR analyses, we know that UHECRs are mostly coming from outside our Galaxy. Despite that, if the acceleration of UHECRs is linked to compact objects, there would be a fraction of UHECRs coming from the Milky Way. With this thesis we analyze the maximum flux which could have been produced by magnetars inside of our Galaxy and detected by the Pierre Auger Observatory during all its lifetime. In order to complete this, we focus this project on different acceleration models in time and energy, and study the propagation of cosmic rays with the latest models of Galactic magnetic fields.

This project is divided in the following sections:

- in the first chapter I explain the main features of cosmic rays, with an excursus on the UHECR physics;
- in the second chapter I show the experimental features of the Pierre Auger Observatory and its main results;
- the third chapter is dedicated to the physics of neutron star in general, with an highlight on magnetars;
- in the fourth chapter I present the basis of this work, explaining how the candidate magnetars has been selected and how the simulation frame has been set;
- in the fifth chapter I develop the analyses on the maximum flux of the magnetars using the Pierre Auger Observatory data;

- with the sixth chapter I expand the analysis on the upper limits from the galactic magnetars to the extra-galactic ones, deducing their contribution to the cosmic ray flux;
- in the seventh chapter I present the conclusion of my work;

Contents

1	Cosmic rays	1
1.1	Cosmic ray spectrum	1
1.2	Cosmic ray composition	3
1.3	Cosmic ray propagation	4
1.3.1	Magnetic fields	4
1.3.2	Cosmic ray interactions	6
1.4	Cosmic ray emission	7
1.4.1	Acceleration mechanism	7
1.5	UHECRs	9
1.5.1	UHECR sources	10
1.5.2	Extensive Air Shower (EAS)	12
1.5.3	UHECR detection techniques	16
2	The Pierre Auger Observatory	19
2.1	The Surface Detector (SD)	19
2.1.1	Station description	20
2.1.2	Triggers and reconstruction	21
2.2	The Fluorescence Detector (FD)	23
2.3	Auger results	25
3	Magnetars	30
3.1	Neutron Stars	30
3.2	Classification of Neutron Stars	33
3.3	Magnetars	34
3.4	Pulsar and magnetar age	35
3.5	Magnetars as UHECR accelerators	38
4	Framework	43
4.1	Magnetars selection	43
4.1.1	Swift J1818.0-1607	44
4.1.2	SGR 1806-20	45
4.1.3	PSR J1846-0258	45
4.1.4	1E 1547.0-5408	45
4.2	Simulation	46
4.3	Analysis	47
4.3.1	Analysis on Arons model	50
4.3.2	Analysis on multiple emission models	51

5	Results	53
5.1	Arons model	53
5.2	Swift J1818.0-1607 ($\tau_c = 265 \pm 1$ yr)	55
5.3	Complete results	60
6	Limits on extra-galactic magnetars	68
6.1	Auger results	68
6.2	Magnetar rate	69
7	Conclusion	74
Bibliography		80
Acnowledgements		86

Chapter 1

Cosmic rays

The study of cosmic rays, started in 1912 by Victor Hess [1], has been central in the development of our knowledge in particle physics. Muons, pions, kaons, whose discovery has been one of the basis in the creation of the Standard Model, are just some of the particles firstly seen in cosmic ray showers.

Although the knowledge in cosmic ray physics improved with time, there are still some open questions we are not capable of answering at the moment, mainly regarding what are the sources of such particles.

A better understanding of the characteristic of their sources could open new scenarios in the astrophysics world and to cosmic ray astronomy.

With this chapter I highlight what is our current knowledge in cosmic rays: I start by explaining the experimental features observed in the spectrum, then I follow back the cosmic rays journey in the Galaxy, depicting the interactions which could happen to the particles, and finally I describe how they are generated.

Since this work focuses on Ultra-High Energy Cosmic Rays (UHECRs), which are cosmic rays with energy above 10^{18} eV, on the last part of this chapter I make an excursus regarding UHECR physics. I start by describing which are the candidate sources, then I describe the interactions they made once they enter the atmosphere and how they affect the detection techniques adopted to observe UHECRs.

1.1 Cosmic ray spectrum

The cosmic ray spectrum measured at Earth can be described as a power law:

$$\frac{dN}{dE} \propto E^{-\gamma}, \quad (1.1)$$

where the value of γ , the spectral index, fluctuates over the energy range. Its changes are linked to effects in the emission sources, in the emission mechanism or in the propagation of cosmic rays.

The first change is at $E_{\text{knee}} \sim 10^{15}$ eV, where γ passes from ≈ 2.7 to ≈ 3.1 , while another change is at $E_{\text{ankle}} \sim 3 \times 10^{18}$ eV, where the spectral index soften to ≈ 2.7 . This two changes of slope are usually called *knee* and *ankle*, due to the resemblance

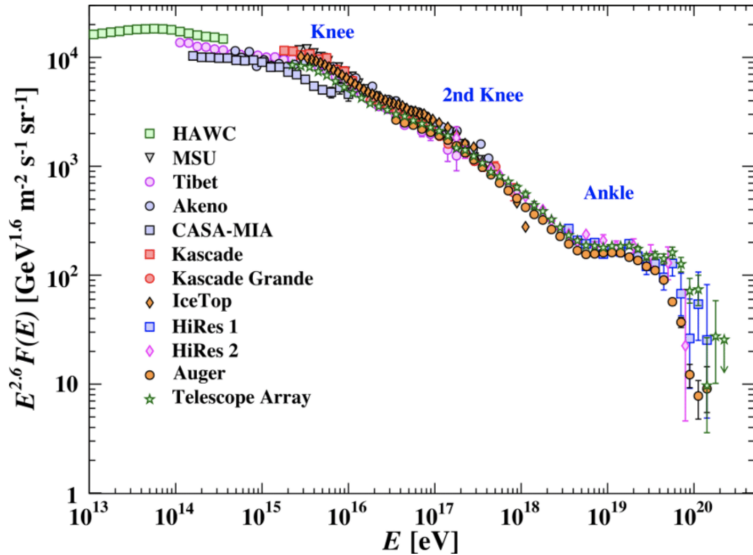


Figure 1.1: Plot of the cosmic ray flux multiplied by $E^{2.6}$ in order to highlight the changes in the spectral index, taken from [2]

of the cosmic ray flux plotted in a logarithmic scale to a human leg, as it can be seen in fig. 1.1.

At $E_{\text{second knee}} \sim 8 \times 10^{16} \text{ eV}$ it has been observed a little change in the slope called *second knee*.

The last change in the spectral index happens at $E_{\text{cut-off}} \sim 4.5 \times 10^{19} \text{ eV}$, where it has been observed a strong cut-off with a factor of $\gamma \approx 5.1$.

Despite having studied the cosmic rays for over a century we are still not able to explain the origin of all the changes in their spectrum. The most promising hypothesis for cosmic rays below the *knee* is being accelerated by Supernova Remnants (SNRs) [3, 4], and the change in the slope is formed since they can not accelerate further. The *ankle* is formed by a switch in the cosmic ray sources, passing from a galactic component to an extra-galactic one, which is confirmed by the detection of a dipole structure in the arrival directions of the cosmic rays [5]. Some hypotheses have been proposed on what causes the cut-off at 45 EeV (1 EeV = 10^{18} eV): it could be linked to the sources not being able to accelerate further or to the interactions that the cosmic rays could have with the background radiations (probably it is a combination of the two effects).

The cosmic ray spectrum spans over 30 orders of magnitude in flux and over 10 orders of magnitude in energy, starting from $10^4 \text{ m}^{-2} \text{ sr}^{-1} \text{ s}^{-1} \text{ GeV}^{-1}$, which is equal to 1 particle per m^2 per s, at $\sim 10^9 \text{ eV}$ to $10^{-28} \text{ m}^{-2} \text{ sr}^{-1} \text{ s}^{-1} \text{ GeV}^{-1}$, which is approximately 1 particle per km^2 per century, at $\sim 10^{20} \text{ eV}$. This radical differences in intensity between low energy cosmic rays and high energy cosmic rays force us to adopt different experimental techniques to detect them. At low energies, up to $\sim 10^{14} \text{ eV}$ the flux is enough high to be studied directly via satellite experiments or balloon experiments. At higher energies, the flux of cosmic rays is so low that, to

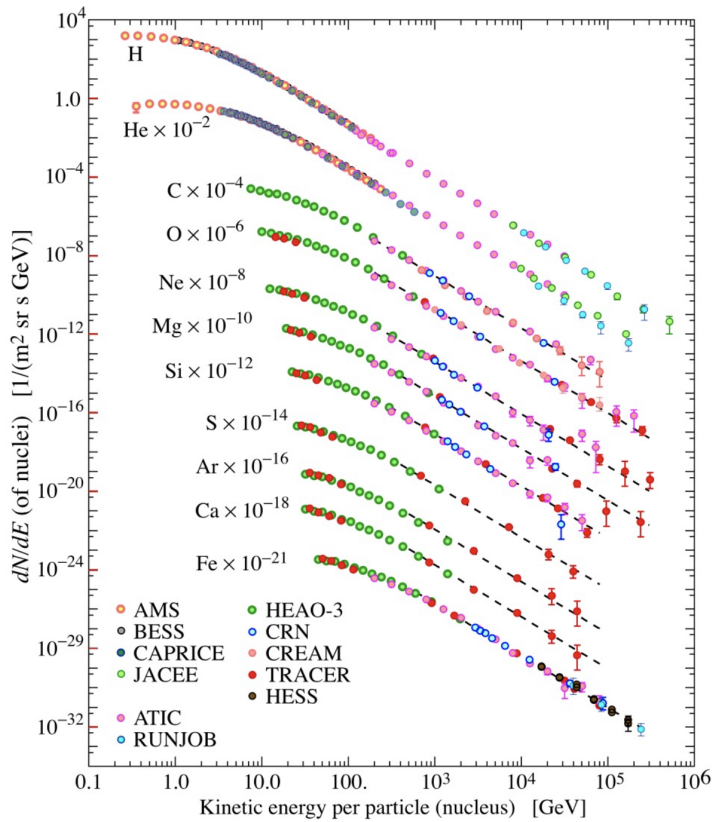


Figure 1.2: Plot reporting the mass composition of the cosmic rays at low energies. At these energies it can be studied directly using spectrometers inside balloon experiments or satellite experiments

collect enough data, we have to cover great areas. This can not be achieved with balloons or satellites, but it can be completed only at the ground. However, as it is explained in section 1.5.2, cosmic rays interact with the nuclei inside of the atmosphere, generating shower of secondary particles. At energies higher than $\sim 10^{14}$ eV, cosmic rays are not detected directly, but their information are reconstructed from the detection of the secondary particles of the showers.

1.2 Cosmic ray composition

Apart from studying the evolution of cosmic rays over the energy, we are also interested in knowing what they are composed of. Cosmic rays are mostly nuclei and, just as the spectrum, their composition changes over the energy.

At low energies, when the cosmic rays are detected directly, we can infer their mass using spectrometry technique. The main component at these energies is the proton one ($\sim 89\%$), with an important helium component ($\sim 10\%$) and less abundant composition of heavier nuclei (the mass composition is summarized in fig. 1.2).

The mass composition is similar to the element abundance inside the Solar System, with some important differences in the fraction of the light component (Li, Be and B) over the medium component (C, N and O) [6, 7]. These differences are symptoms of the deflections of cosmic rays inside of our Galaxy and their interactions with the interstellar medium [8].

At higher energies we cannot measure directly the composition of the cosmic rays, but we can infer it by the study of the showers of secondary particles, formed by the interaction with nuclei in the atmosphere (for a detailed description of the showers see section 1.5.2). By the showers some mass-dependent observables can be measured, two of the most important one are: the number of muons inside the shower and the depth where the shower reaches the maximum number of particles. At energies between E_{knee} and E_{ankle} the number of muons is the mainly used technique. However, above the *ankle*, the uncertainties on the hadronic interaction model of the cosmic rays with the nuclei inside of the atmosphere become really important, and the simulations of the atmospheric showers do not reproduce the number of muons correctly anymore. At these energies, the number of muons is not a suitable observable anymore and the mass studies are carried on reconstructing the maximum depth of the showers inside the atmosphere collecting the fluorescence light emitted by the showers, using the so-called fluorescence detectors. The number of muons is the preferable mass-deriving technique below the *ankle* also because the fluorescence light produced in the showers is very fleeble and cannot be collected using fluorescence detectors.

1.3 Cosmic ray propagation

Before being detected over the atmosphere or at the ground the cosmic rays have traveled inside of our Galaxy and, for some energies, also outside of it. Since they are mostly charged particle, they have been deflected by the magnetic field. Furthermore at the highest energies the cosmic rays could also interact with the photon backgrounds, mainly the Cosmic Microwave Background (CMB).

1.3.1 Magnetic fields

The cosmic rays are mainly nuclei, so they are deflected by the galactic and the extra-galactic magnetic fields. The deflection can be described using the Lorentz law

$$m\Gamma \frac{d\mathbf{v}}{dt} = q\mathbf{v} \times \mathbf{B}, \quad (1.2)$$

where Γ stands for the Lorentz factor.

By last equation we can find the curvature radius of the deflected particle. Considering \mathbf{v} and \mathbf{B} perpendicular to each other, in order to ignore the vectorial product, and imposing that the Lorentz force is equal to the centrifugal acceleration, we have

$$R = \frac{m\Gamma v^2}{qB} = \frac{E}{ZeB}. \quad (1.3)$$

The curvature radius is directly proportional to the energy of the cosmic ray and inversely proportional to its charge and to the strength of the magnetic field. At the same energy the more intense is the charge of a particle the more it is deflected, therefore an iron nucleus is deflected 26 times more than a proton.

The deflection of the cosmic rays can be estimated applying the following equation

$$d\theta(E, d) \propto Z \times \left(\frac{E}{10^{20} \text{ eV}}\right) \times \left(\frac{B}{10^{-9} \text{ G}}\right)^{-1} \times \left(\frac{d}{\text{Mpc}}\right). \quad (1.4)$$

A proton of 10^{20} eV, travelling for a distance of 1 Mpc inside of a magnetic field of 1 nG is deflected of $\sim 1^\circ$.

The presence of a Galactic Magnetic Field (GMF) has been firstly proposed by Fermi in 1954, who predicted also a strength of $\mathcal{O}(1)$ μG [9]. Our Galaxy can be approximated to a disk of radius ~ 15 kpc and height ~ 300 pc. Starting from eq. (1.3) we can obtain the curvature radius of a proton with $E \sim 10^{18}$ eV, which is ~ 300 pc, meaning that, from this energy, cosmic rays are not trapped in the Galaxy anymore. Beside, until 10^{18} eV, cosmic rays are confined in the Galaxy and they are deflected only by the GMF.

The measure of the GMF is accomplished via studies on the Faraday rotation in the polarization of radio emission of different sources, mostly extra-galactic radio sources and pulsars [10]. The rotation is caused by the electrons along the line of sight connecting the sources to the Earth. The Faraday rotation is

$$\text{RM} [\text{sr m}^{-2}] \simeq 0.81 \int_0^L \left(\frac{n_e(l)}{\text{cm}^{-3}}\right) \left(\frac{B_{||}(l)}{\mu\text{G}}\right) \left(\frac{dl}{\text{pc}}\right), \quad (1.5)$$

where $n_e(l)$ is the density of electrons along the line of sight l , while $B_{||}$ is the parallel component of the magnetic field.

Pulsars are very effective probes of the GMF since the Faraday rotation applied to them manifests as a dispersion measure (DM) in the emitted light, leading to a direct estimation of the GMF:

$$\langle B_{||} \rangle [\mu\text{G}] = \frac{\int_0^L n_e B_{||} dl}{\int_0^L n_e dl} = 1.232 \frac{\text{RM}}{\text{DM}}, \quad (1.6)$$

where $\langle B_{||} \rangle$ is the measure of the parallel component of the GMF averaged over the electron density. By considering pulsars near each other we can obtain a tomography of the GMF. Other information about the GMF can be obtained using the synchrotron emission, which is dependent to B_\perp .

The GMF is not homogeneous and can be divided in three components: a large-scale field, a small-scale field and a striated field [11].

The large-scale field describes the component which is coherent on length scale of the order of the dimension of the Galaxy. The configuration of this component is still unclear but the magnetic field seems to roughly follow the spiral arms, and in the Disk area, the magnetic field is symmetric with respect the Galactic plane. The strength of this component is around $1.5 - 2 \mu\text{G}$, although we know that the total field strength around the Solar system is around $6 \mu\text{G}$, and that towards the Galactic

Center the field strength increases, estimates from synchrotron emission gives a total strength of $10 \mu\text{G}$ at galactocentric radius of 3 kpc .

The small-scale field describes the component connected to the turbulent Interstellar Medium. The strength of the random, turbulent magnetic field component can be estimated from RM fluctuations, and, although the strength is still not clear, it is estimated to be $\sim 3 - 4 \mu\text{G}$.

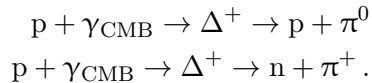
A third component of the magnetic field, included in Galactic magnetic field studies, describes a field whose direction varies on small scales, but the orientation does not. Such a field can arise when a turbulent field structure is compressed into a two-dimensional structure. This field component is often referred to as striated random.

The Extra-Galactic Magnetic Field (EGMF) is largely less known than the GMF. From [12] we know EGMF with coherence lengths of about 1 Mpc can not be stronger than 1.7 nG , whereas a universe-wide EGMF is bound to be weaker than about 0.65 nG . These limits are obtained using RM data from extra-galactic sources. Although being 3 order of magnitude less strong than the GMF, the EGMF plays an important role in the UHECR studies, especially for particles with high Z .

1.3.2 Cosmic ray interactions

During their journey in space cosmic rays could interact with the photon backgrounds, especially the Cosmic Microwave Background (CMB). Discovered by Penzias and Wilson in 1965 [13], the CMB is a relic black body radiation of the recombination epoch which permeates the Universe with a photon density of $411 \text{ particles/cm}^3$ and with average energy of $5 \times 10^{-4} \text{ eV}$ [14, 15]. UHECRs can interact with the CMB, leading to an attenuation of the cosmic ray flux at the highest energies. The energy threshold of the interactions depends on the process and the particles involved.

Protons could interact with the CMB photons in a pion photoproduction interaction called GZK, from Greisen, Zatsepin and Kuzmin who first predicted this process in 1966 [16, 17],

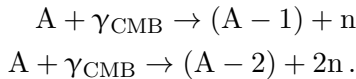


The threshold energy of this interaction is the energy needed to produce a p and a π^0

$$E_{\text{th}} = \frac{m_\pi(m_\pi + 2m_p)}{4E_\gamma}, \quad (1.7)$$

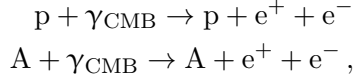
this is $\sim 1.4 \times 10^{20} \text{ eV}$ for a photon of energy equal to 0.5 meV . Since the CMB is a black body radiation there is a tail of photon at higher energies, thus we expect the cosmic rays to start making GZK interactions at lower energies.

The cosmic ray flux is not composed only by protons but also by heavier nuclei. Such nuclei could have a photodisintegration interaction similar to the GZK [18]



The threshold energy is directly proportional to the mass, thus heavier nuclei survive longer than the lighter ones.

Apart from photodisintegration interactions, cosmic rays could go under Bethe-Heitler pair production, both the protons and the nuclei



the threshold energy in this case is

$$E_{\text{th}} = \frac{m_e(m_e + 2m_p)}{2E_\gamma} , \quad (1.8)$$

and, for a photon of E_γ equal to 0.5 meV, this is equal to $\sim 1 \times 10^{18}$ eV, which is lower than the GZK threshold.

Although having a lower threshold energy, the pair production effect is less dominant since a cosmic ray loses circa 0.1% of its energy for each of these interactions, while loses circa 20% of its energy for each photopion interaction. We can also compute the propagation length associated with an average energy loss of one order of magnitude, this is called *energy loss length*. For the pair production effect this is approximately 1 Gpc. For the photodisintegration effect the *energy loss length* is lower and it oscillates from 100 Mpc, for protons and iron nuclei, to 10 Mpc for intermediate nuclei; this leads to an expected suppression of the cosmic ray flux at the Earth, approximately around 50 EeV (similar to the one observed in the cosmic ray flux), and the definition of a local bubble, called *GZK bubble*, outside of which sources could not contribute to the cosmic ray flux observed at the Earth.

Apart from the CMB, cosmic rays could interact with other photon backgrounds, such as the Infrared Background Light (IBL) and the Cosmic Optical Background (COB). These interactions lead to minor energy losses for cosmic rays, due to the limited photon densities.

1.4 Cosmic ray emission

Following the journey of the cosmic rays back from their detection at the Earth, we have arrived at the point to discuss how they are originated. In this section I present how the cosmic rays can be accelerated in the astrophysical objects.

1.4.1 Acceleration mechanism

Cosmic ray energies can not be reached by a single interaction, thus the particles have to be bound to their sources until they reach sufficient energies. A particle gains energy by consecutive interactions while being trapped by the magnetic field of the sources, which has to be coherent over a significant region. By this assumption we can derive the maximum energy which can be reached by an accelerating particle, requiring that the Larmor radius must be smaller than the dimension of the source

$$\left(\frac{E_{\text{max}}}{\text{EeV}} \right) \propto Z \left(\frac{B}{\mu\text{G}} \right) \left(\frac{R}{\text{kpc}} \right) . \quad (1.9)$$

The maximum reachable energy is directly proportional to the charge of the accelerating particle, the strength of the magnetic field and the coherent length of the magnetic field.

By using eq. (1.9) we obtain a necessary condition to derive the maximum energy reachable by an astrophysical object in accelerating cosmic rays, however we need also a mechanical model which can describe the interactions involving the accelerating particles. The most commonly invoked model, and one of the first proposed, is the so-called Fermi-I model, proposed by Enrico Fermi in 1949 [19]. However, this is not the first mechanism proposed by Fermi. The first one, which the Fermi-II is derived from, is the Fermi-II model and explains the acceleration of relativistic particles by means of their collision with interstellar clouds. These clouds move randomly and act as *magnetic mirrors*, so that the particles are reflected off them. The average energy gain per collision is

$$\left\langle \frac{\Delta E}{E} \right\rangle = \epsilon = \frac{8}{3}\beta^2, \quad (1.10)$$

where $\beta = v/c$ is the velocity of the cloud (the model is called Fermi-II for the quadratic dependence on the velocity). Since we have $\beta \ll 1$, the acceleration mechanism is slow.

With this simple model we can evaluate the expected cosmic ray flux. After n collisions a particle will have energy:

$$E_n = E_0(1 + \epsilon)^n, \quad (1.11)$$

and the probability of escape at the n -th collision is

$$P_n = P(1 - P)^n. \quad (1.12)$$

Combining the last two equations we can get the number of particles escaping with energy E_n , given N_0 initial particles

$$N_n = N_0 P_n = N_0 P(1 - P)^n = N_0 P \left(\frac{E_n}{E_0} \right)^{\frac{\ln(1-P)}{\ln(1+\epsilon)}}, \quad (1.13)$$

which translates to the differential spectrum

$$\frac{dN}{dE} \approx \frac{N_n}{(E_{n+1} - E_n)} = \frac{N_n}{\Delta E} \propto E^{-\gamma}. \quad (1.14)$$

The power law factor γ is dependent on the escape probability P and the energy gain ϵ , which for the Fermi-II goes as β^2 [20].

Taking in account propagation effect we expect a cosmic ray flux at the source with a power law factor of $\gamma \approx 2$, however with the cloud velocity of the Fermi-II mechanism we do not reach this value. The situation changes drastically when we consider the acceleration inside shock waves which can reach supersonic velocity, like those produced in supernova explosions or Active Galactic Nuclei (AGN). In these area there is a complete symmetry when a high-energy particle crosses the shock

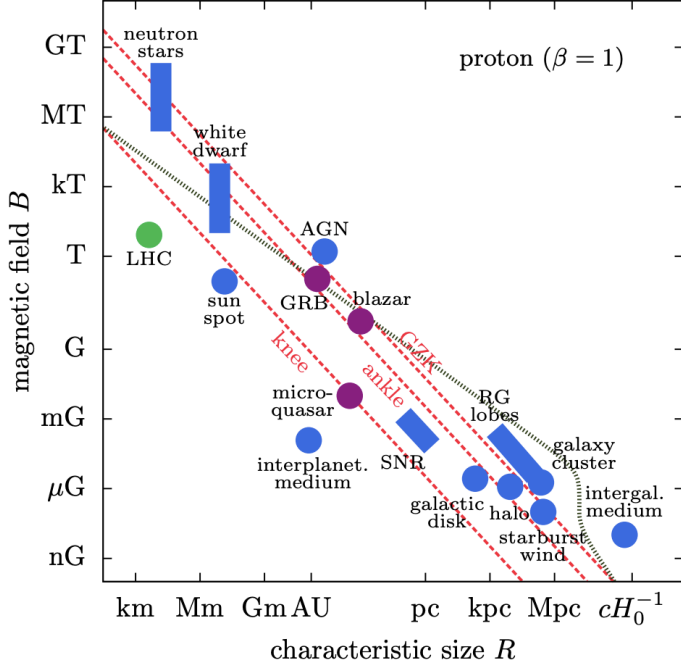


Figure 1.3: The Hillas plot, from [21]. It figures the magnetic fields of several astrophysical object in function of their size and it highlights the best candidate as UHECR accelerators.

from downstream to upstream or from upstream to downstream and in both types of crossing, the particle gains energy. The average energy gain in this case is

$$\left\langle \frac{\Delta E}{E} \right\rangle = \epsilon = \frac{4}{3} \beta, \quad (1.15)$$

and with reasonable values for P , one gets $\gamma = 2$, which is the expected value.

The Fermi models are not a comprehensive explanation of how cosmic rays are accelerated, since they are thought to act on test particles, meaning that the accelerated cosmic rays do not enter in the energy balance of the sources. However this is not compatible with SNRs, since $\sim 10\%$ of their energy should be converted in accelerating particles. Furthermore, the Fermi models could not explain the acceleration of particles up to 0.1 EeV inside of SNRs, of which there is evidence.

1.5 UHECRs

Having completed the general review on cosmic ray physics, I begin now a more specific section regarding UHECRs.

1.5.1 UHECR sources

Considering eq. (1.9) we can understand that not all astrophysical objects can accelerate particles above 10^{18} eV. Nevertheless among the candidate sources we have astrophysical objects that span over several orders of magnitude in dimension. We oscillate from neutron stars, which have a small radius but a strong magnetic field, to AGNs, which have a weaker magnetic field but coherent over a great radius. In order to express all the hypotheses I will complete now a schematic review of the candidate sources. All the candidates UHECR accelerators are summarized in fig. 1.3, which reports the so-called Hillas plot, which put all the candidate cosmic rays accelerators on the base of the intensity of their magnetic field and its extension.

- **Compact objects:** the smallest candidates are neutron stars, which have the strongest magnetic fields in the Universe, going from $10^{10} - 10^{12}$ G, up to 10^{14} G for magnetars. The highest reachable energy should be $E_{\max} = \Omega Z B_{\text{surf}} R^2 / c$, where Ω is the rotational velocity of the neutron star, B_{surf} the strength of the surface magnetic field and R is the star radius. Following this observation magnetars could accelerate protons up to 100 EeV [22]. Nevertheless, we know several magnetars inside of our Galaxy but none of them is currently accelerating particles to the highest energies. One hypothesis is that magnetars could not accelerate constantly but just in the early stage of their formation, thus we could expect magnetars in the local universe to produce the majority of UHECRs.
- **Starburst Galaxies (SBGs):** SBGs are galaxies with an intense rate of star formation, normal galaxies generate stars with a rate of $\sim 3 M_{\odot}/\text{yr}$ ($1 M_{\odot} = 2 \times 10^{33}$ g) while SBGs have a rate of $\sim 100 M_{\odot}/\text{yr}$. The acceleration of UHECRs inside of these galaxies could happen for the formation of the so-called *superwind*, which is the adiabatic expansion from the center of the galaxies of the hot gas generated by the multitude of hot stars and supernova explosions [23]. It seems that the terminal shock regions can accelerate cosmic rays to the highest energies, reproducing the observed conditions. On the other hand, since we have an intense rate of star formation we have also an intense rate of star *death*, leading to the formation of an important concentration of compact objects, which, as previously exposed, are candidate UHECR sources. The acceleration could not be carried on only by the *superwind*, but also by the compact objects formed in these galaxies.
- **AGN accretion disks:** AGNs have been considered for long time the perfect candidates to accelerate UHECRs [25, 26], since they're known to be emitters of non-thermal light. The acceleration would happen inside the accretion disk of matter orbiting around the supermassive black hole at the center of the galaxy, this region has magnetic fields of $\mathcal{O}(1)$ G coherent over a radius of $10^{-4} - 10^{-3}$ pc ($1 \text{ pc} = 3.0857 \times 10^{13}$ km), permitting the acceleration of UHECRs. The acceleration region is dense in photons, and high energy particles, as the protons emitted, should interact and lose energy, while the heavier nuclei

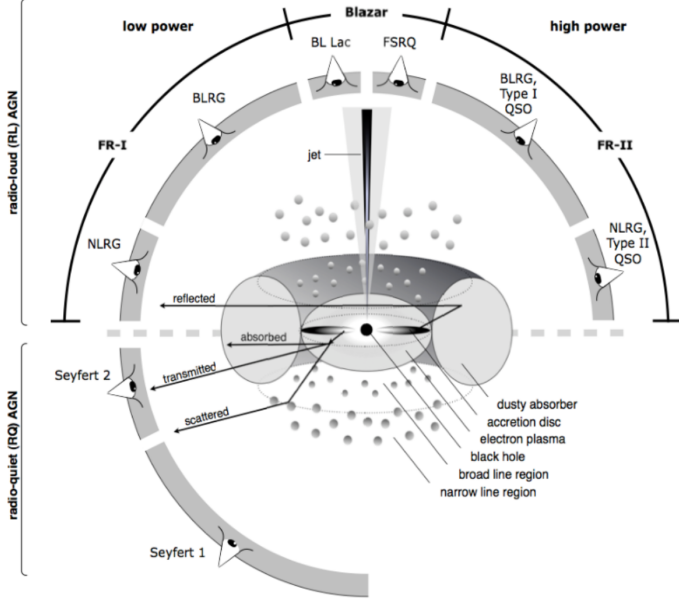


Figure 1.4: Scheme reporting the classification of AGNs from [24]

should photodisintegrate even more quickly. Nowadays we do not expect AGN accretion disks to contribute heavily in the UHECRs flux.

- **Radio galaxies:** while the AGN accretion disks should not be the right sources in general, peculiar type of AGNs are interesting candidates. In fact certain types of radio-loud AGNs are characterized by large lobe of plasma extending from the central supermassive black hole for hundreds of kpc. These are called *Fanaroff – Riley* galaxies and we distinguish *Fanaroff – Riley type I* (FRI) if the lobes dissipate in density with distance and *Fanaroff – Riley type II* (FRII) if the lobes show high density regions at the ends (*hot – spots*). The difference between the two types could come when the jets are supersonic (FRII) or subsonic (FRI) [27]. Lobes exceed the galaxy of $\mathcal{O}(100)$ kpc with magnetic fields of $\mathcal{O}(1)$ μG , on the other hand the *hot – spots* are of $\mathcal{O}(1)$ kpc while their magnetic fields are of $\mathcal{O}(100)$ μG . Both the lobes and the *hot – spots* are potential sites to accelerate UHECRs. If the jets are oriented towards the Earth the galaxies are called *Blazars*, which are the most commonly identified sources of extra-galactic gamma rays known at the moment. Therefore AGNs, in general, and *Fanaroff – Riley* galaxies, in particular, are important candidate hosts for UHECR acceleration. fig. 1.4 reports a schematic description of the classification of AGN.
- **Galaxy clusters:** inside Galaxy clusters magnetic fields of $\mathcal{O}(1)$ μG should extend coherently over distance of $\mathcal{O}(100)$ kpc. This environment is indeed capable to accelerate UHECRs up to 100 EeV, however the long paths which particle should travel, would decrease the maximum reachable energy due to

the interactions with the photon backgrounds.

- **Gamma Ray Bursts (GRBs):** GRBs are extremely energetic explosions in the γ band. We distinguish two classes: short GRBs (<1 s) and long GRBs ($1 - 2$ s). The first ones are associated to the merging of two neutron stars into a black hole, as has been observed with multimessenger event with gamma rays and gravitational waves. The second ones are associated to *hypernovae*, which are extremely intense core-collapse supernovae. Although being able to accelerate UHECRs, GRBs are disfavoured as candidate sources for their rarity in the local universe: they have been observed mostly at high redshift and the number of events observed inside the GZK *bubble* is not sufficient to justify the measured UHECR flux [28].

1.5.2 Extensive Air Shower (EAS)

When the cosmic rays enter in the atmosphere they interact with the nuclei inside of it. The atmosphere is a thick layer which acts as a calorimeter on high energy cosmic rays. These particles generate a cascade of secondary particles, defined Extensive Air Shower (EAS). Since cosmic rays are mostly nuclei the first interaction is governed by the *quantum chromodynamics* (QCD), whose laws are not fully understood, therefore our simulations differ slightly from the experimental features observed.

Inside EASs we can distinguish three components:

- **electromagnetic component:** composed by the photons, electrons and positrons. This is by far the most dominant component of the shower that reaches the ground.
- **hadronic component:** composed mainly by pions and other mesons. It is predominant in the early stages of the shower and becomes much less dominant at the ground.
- **muonic component:** composed by muons generated by the decays of pions in the early stages. Muons act as rectilinear particles reaching the surface without significant energy loss

Apart from these three components there is a fourth component formed by the weakly interacting particles, as neutrinos. These are referred as *invisible* particles since their calorimetric deposit can be neglected.

With the following sections I present a model for the development of the EASs. I start by presenting a model for purely electromagnetic showers then I move on to hadronic showers. I use this approach since electromagnetic showers are less complex than the hadronic ones; furthermore hadronic showers contain electromagnetic sub-showers.

Electromagnetic shower

The one I'm going to present is the Heitler's model for electromagnetic showers [29], which treats the electromagnetic showers as a perfect binary tree composed only by three types of particles: electrons (e^-), positrons (e^+) and photons (γ).

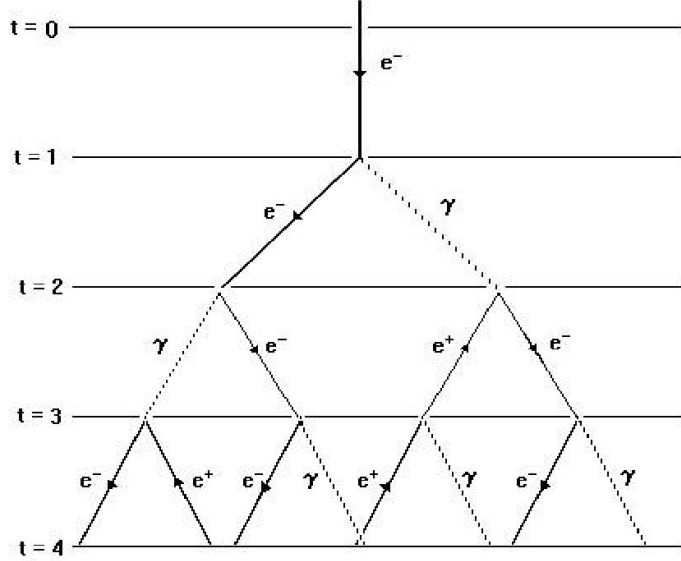


Figure 1.5: Simple scheme of the development of an electromagnetic shower, from [30]

We can consider that at high energies the dominant processes for the electromagnetic particles are: bremsstrahlung, for e^- and e^+ , and pair production, for γ . The bremsstrahlung is a QED process in which a e^+ or e^- interacts with a nucleus and loses energy emitting a photon. We can define the parameter X_0 , which is the path length after which a particle loses all but $1/e$ of its energy, and in the atmosphere it is equal to $\approx 37 \text{ g/cm}^2$. The pair production is also a QED process in which a γ interacting with a nucleus emits an e^+ and an e^- . The mean free path for this process is equal to $9/7X_0$. Therefore we can say:

$$-\frac{dN}{dE} \Big|_{\text{brem}} \approx -\frac{dN}{dE} \Big|_{\text{pair}} \approx \frac{E}{X_0}. \quad (1.16)$$

We can consider now an electromagnetic shower initiated by an e^- with energy E_0 , as schematically reported in fig. 1.5. After the first bremsstrahlung interaction, there is a second generation of particles formed by the initial e^- and the γ emitted. We can consider that the energy splits equally in the two particles, so both the e^- and the γ have $E_0/2$. The shower continues its development doubling the number of particles in each generation: after n generations the shower is composed by 2^n particles, each with energy equal to $E_0/2^n$. The development stops when the energy loss for bremsstrahlung is equal to the energy loss for ionization, this happens at the so-called critical energy E_c . The number of particles inside the shower at this point is

$$N_{\max} = \frac{\ln(E_0/E_c)}{\ln(2)}. \quad (1.17)$$

Taking the step interaction as $X_0 \times \ln(2)$, the atmospheric depth where we have

these number of particles is

$$X_{\max} = X_1 + X_0 \ln\left(\frac{E_0}{E_c}\right), \quad (1.18)$$

where X_1 is the atmospheric depth at which the first interaction happens. The previous depth has been defined X_{\max} since after this point the shower particles cannot produce more particles, but they can only be absorbed. consequentially at X_{\max} the shower reaches the maximum number of particles.

By the last equation we can derive the *elongation rate*, which is the rate of change of X_{\max} in function of E_0

$$D = \frac{dX_{\max}}{d \log_{10}(E_0/\text{eV})} = \ln(10) \frac{dX_{\max}}{d \ln(E_0)} \simeq 2.3X_0. \quad (1.19)$$

With the reported interaction length, the *elongation rate* is 85 g/cm^2 per decade in air for electromagnetic shower.

The Heitler model is a first approach in EAS study, nevertheless it correctly reproduce the relation between the N_{\max} and the initial energy E_0 , and it provides a logarithmic relation between the X_{\max} and E_0 .

Hadronic shower

The previous model can be generalized in the Heitler-Matthews model describing showers generated by a nucleon [31]. The main difference is that a nucleon will make a QCD interaction, producing $2N_\pi$ charged pions (π^\pm) and N_π neutral pions (π^0). π^\pm and π^0 behave differently: a π^0 decays in two photons with a decay time of $8.5 \times 10^{-17} \text{ s}$ giving birth to two electromagnetic showers; π^\pm either make another hadronic interaction or decay in a μ^+ (μ^-) and a ν_μ ($\bar{\nu}_\mu$). If the decay length is shorter than the interaction length a π^\pm will mostly decay. The pion interaction length in atmosphere is $\approx 120 \text{ g/cm}^2$, thus the decay length is

$$L [\text{g/cm}^2] = \Gamma c \tau \rho = \frac{E}{mc} \tau \rho, \quad (1.20)$$

where Γ is the Lorentz factor, ρ is the atmospheric density and τ is the decay time, which is $\sim 2.5 \times 10^{-8} \text{ s}$. Considering $\rho = 10^{-3} \text{ g/cm}^3$, pions tend to interact over $\approx 20 \text{ GeV}$, while they tend to decay below $E_c^\pi \approx 20 \text{ GeV}$. However at high altitude the atmosphere is less dense, and so it is L ; so the faster a particle interacts in the atmosphere the bigger its muon component is.

For simplicity we can consider that all the charged pions generated in the first stage interact. At the second generation there are $(2N_\pi)^2$ charged pions with energy $E_0/(3N_\pi)^2$. Thus, the number of steps to reach the critical energy E_c^π is

$$n_c = \frac{\ln(E_0/E_c^\pi)}{\ln(3N_\pi)} \quad (1.21)$$

Now assuming that all the pions reaching the critical energy decay into muons, we can deduce the number of muons in the shower (N_μ)

$$N_\mu = (2N_\pi)^{n_c}. \quad (1.22)$$

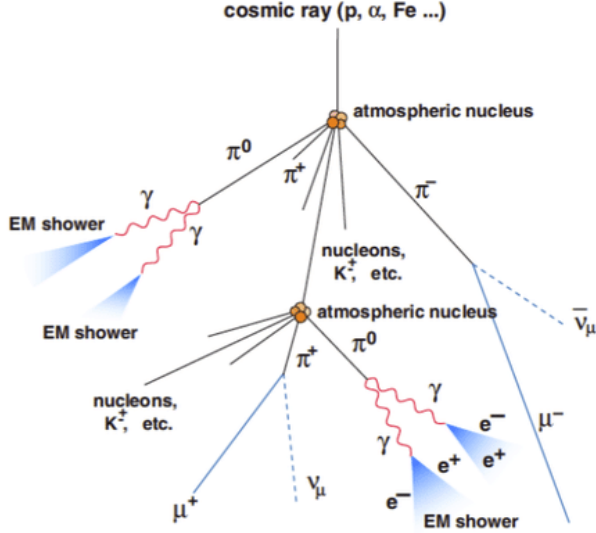


Figure 1.6: Scheme reporting the first interactions inside an hadronic extensive shower, from [32]

By assuming the pion multiplicity $N_\pi = 5$ and defining the new parameter $\beta = \ln(2N_\pi)/\ln(3N_\pi) \approx 0.85$ we can rewrite the previous equation as:

$$N_\mu = \left(\frac{E_0}{E_c^\pi} \right)^\beta, \quad (1.23)$$

which shows that the muon component do not depend linearly with the initial energy but increase with it. Anyway, this result is strongly dependent on the multiplicity of the interaction.

It is now possible to estimate the atmospheric depth of the maximum number of particles in the shower (X_{\max}). Since there are two different component in these showers, the hadronic one and the electromagnetic one, we can define the X_{\max} as the value obtained for the electromagnetic component, cause it is the most important one

$$X_{\max} \sim X_1 + X_{\max}^{\text{e.m.}} \left(E_0^{\text{e.m.}} = \frac{E_0/2}{3N_\pi} \right), \quad (1.24)$$

where X_1 is the atmospheric depth at which we have the first interaction. By recalling eq. (1.18) we can write

$$X_{\max} \sim X_1 + X_0 \ln \left(\frac{E_0}{6N_\pi E_c} \right), \quad (1.25)$$

and, as in the electromagnetic shower, we can evaluate the *elongation rate*

$$D^h = \frac{dX_{\max}^h}{d \log_{10}(E_0)} \sim D^{\text{e.m.}} \left(1 - \frac{d \log_{10}(6N_\pi)}{d \log_{10}(E_0)} \right), \quad (1.26)$$

which can be evaluated to be $\approx 58 \text{ g/cm}^2$, smaller than the electromagnetic case.

The superposition model

Starting from the Heitler-Matthews the shower generated by a nucleus with A nucleons can be described using the so-called *superposition model*. The energies of the UHECRs generating the shower are much higher than the binding energies per nucleon, therefore a nucleus with A nucleons and initial energy E_0 can be described as A free nucleons, each having initial energy E_0/A . Each nucleon follows the Heitler-Matthews model but the total shower is given by superpositioning every cascade.

From this assumption the X_{\max} of a shower generated by a nucleus can be estimated as

$$X_{\max}^A(E_0) = X_{\max}^n(E_0/A) - X_0^{\text{e.m.}} \ln(A). \quad (1.27)$$

Heavier nuclei develop earlier in the atmosphere, meaning the reach sooner the critical energy and they have a major contribute of muons than a nucleon shower. The number of muons is

$$N_{\mu}^A(E_0) = A N_{\mu}^n(E_0/A) = A^{1-\beta} \left(\frac{E_0}{E_c^{\pi}} \right)^{\beta}. \quad (1.28)$$

Showers initiated by an iron nucleus contain $\sim 50\%$ more muons than the ones initiated by protons.

1.5.3 UHECR detection techniques

As previously said the detection of cosmic rays is strictly dependent to their flux, which differs in function of the energy. Below 10^{14} eV the flux is large enough to perform a direct detection of the cosmic rays outside of the atmosphere via balloon or satellite experiments. Unfortunately, the cosmic ray flux over 10^{14} eV is so low that we need to cover large experimental areas to get enough data, this cannot be achieved using balloons or satellites but only at the ground. For these class of cosmic rays, including UHECRs, the detection of the secondary particles inside the EASs is mandatory to achieve information on the primary cosmic ray generating the shower. This detection is mostly performed using two major techniques: ground arrays and atmospheric light detectors.

Ground arrays

The most common technique to reconstruct EAS is sampling the front of the shower with an array of detector at the ground. This is also the technique used by Bruno Rossi and Pierre Auger to detect the first UHECR shower [33]. The detectors adopted can be scintillators or Water Cherenkov detectors. The Water Cherenkov detectors collect the Cherenkov light formed by the passage of charged particles travelling with a speed higher than the light speed in the selected medium (commonly water).

To maximize the detection of showers is important to chose wisely the height above sea level of the detectors, the size of the array and the spacing between each stations.

The height has to be chosen carefully since we want to detect the largest number of particle possible, therefore the arrays need to be placed just below the point where

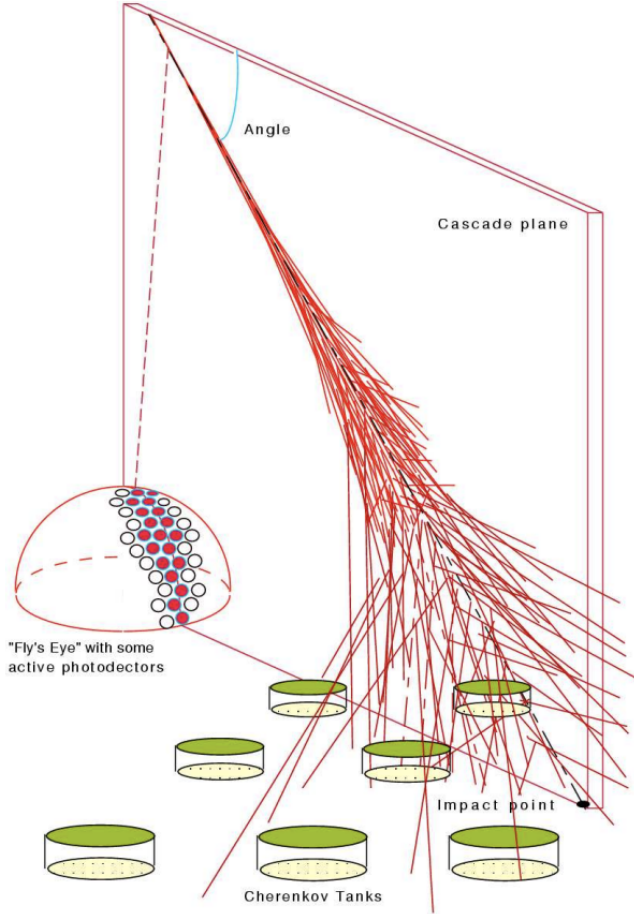


Figure 1.7: Scheme of am hybrid detector which can perform both as a ground array and atmospheric light detector, leading to a better sampling of the EAS, from [34]

the showers reach the X_{\max} . The best height depends on the energy of the selected cosmic rays; for UHECRs it is between 1000 m and 1500 m.

The size of the array depends on the energy too. Since the flux decreases as a power law the more energetic the particles of interest are the larger the array should be. For UHECRs arrays are of $\mathcal{O}(1000) \text{ km}^2$. EASs have also different extension in function of the energy. UHECR showers reach dimension of tens of km^2 , therefore a spacing between the stations of $\sim 1 \text{ km}$ is sufficient to have a good sampling of the events. Therefore the spacing of the array has to be chosen after the minimal energy we want to observe (the more energetic is a particle the larger is the shower generated), while the total surface after the maximal one.

With ground arrays the energy and the direction of the primary cosmic ray can be reconstructed. The energy is obtained from the signal left by the shower in each station, the greater the signal the greater the energy. The direction is reconstructed using the time signal, i.e. knowing which stations collect the first signals.

Unfortunately the mass number A of the particle generating the shower can not be measured directly, but it can be estimated using A -dependent quantities. Two of these quantities are X_{\max} , which depends on the logarithm of A , and the number of muons contained in the shower. However, the reconstruction of the mass of the primary particle is a delicate theme in UHECR physics, since it is complicated by the important uncertainties on the hadronic interaction model.

Atmospheric light detectors

Charged particles passing in the atmosphere excites molecules inside the gas, their de-excitation leads to the emission of photons (with λ in the UV band). Therefore, the atmosphere can be also used as a scintillator, to collect the fluorescence light emitted.

The fluorescence efficiency, which is the energy emitted in fluorescence photons per unit of energy deposited by the charged particles, is very low, $\sim 10^{-5}$, therefore only a shower with a high number of particles could emit detectable photons, roughly only UHECRs.

By studying the fluorescence light the parameter of the primary cosmic ray can be reconstructed: the energy of the particle is derived from the intensity of the light, the direction and geometry of the shower is obtained combining the information of two or more telescopes. Using this technique, the maximum depth of the shower can be observed directly, from which we derive the information on the mass of the primary particles.

The information on the EAS is better obtained using atmospheric light detectors the ground arrays, since we see directly its longitudinal development. However these detectors are more delicate; the fluorescence light emitted is very feeble, therefore they can operate only in moonless night with a good weather condition (no rain, snow or wind). The duty cycle of atmospheric light detectors is way smaller than the one of ground arrays. In order to exploit the advantages of both the techniques the best way to act is build an hybrid detector, i.e. a detector that can cover the same area with both the techniques, in order to observe the same events in two ways. The next chapter is fully dedicated to the description of the most important hybrid detector of the world, which is the Pierre Auger Observatory, meanwhile a schematic depiction of how an hybrid detector should work is reported in fig. 1.7.

Chapter 2

The Pierre Auger Observatory

The Pierre Auger Observatory (from now Auger) is the largest observatory to study UHECRs [35].

It is located in Argentina, in the province of Mendoza, near the city of Malargüe, on a vast plateau at ~ 1400 m above sea level, and it covers an area of $\sim 3000 \text{ km}^2$. The height has been chosen wisely to allow the observation of the average shower maximum at the energy of interest. The chosen site is also optimal considering the atmospheric conditions, since it is characterized by the absence of light pollution, by a dry climate, which favors a clear sky, and by a rarefied atmosphere.

The observatory is taking data since 1 January 2004, though the full configuration was completed in 2008. It has been the first experiment to study the UHECRs with two complementary techniques: a ground sampling of the shower front, with the Surface Detectors (SD), and the observation of the fluorescence light emitted by the charged particles passing in the atmosphere, with the Fluorescence Detector (FD). The SD is currently composed by 1660 Cherenkov detectors while the FD is formed by 27 telescopes divided in 5 buildings. A schematic map of the observatory is reported in fig. 2.1.

Being an hybrid detector is one of the main strength of Auger. In fact using two techniques to see the same events has been crucial in Auger lifetime, since it allowed to cross-check the reconstruction methods and to minimize the need of simulations.

Since this thesis has been completed using Auger data, in this chapter I expose the features of the SD and the FD, focusing on their advantages and disadvantages, then I report the most important results obtained by the Pierre Auger Observatory.

2.1 The Surface Detector (SD)

The Surface Detector reconstruct the information on the primary cosmic rays collecting the particles contained in the front of the showers. This purpose is accomplished using an array of stations covering an area of $\sim 3000 \text{ km}^2$ and a system multitriggers, in order to reconstruct only real events.

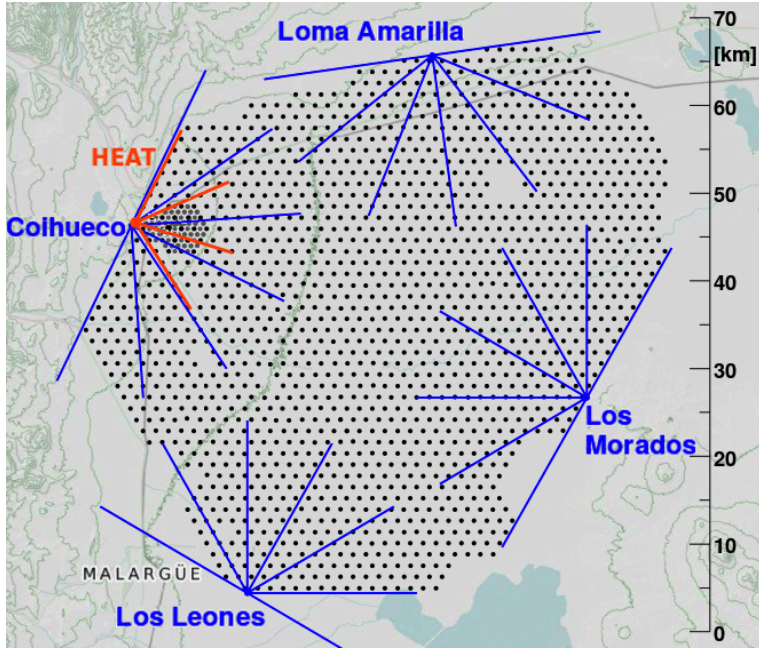


Figure 2.1: Scheme of the geometry of the Pierre Auger Observatory seen from above from [36]. Each black dot represents a station of the SD while the colored dot on the perimeter are the FD buildings. The wedges defined by the blue and red line are the field of view of each fluorescence telescope.

2.1.1 Station description

The stations composing the SD are Water Cherenkov Tanks (WCDs) placed in a triangular grid at a distance of 1.5 km from each other. The distance has been chosen considering that the EASs of the UHECRs can reach the dimension of $\mathcal{O}(10)$ km², the SD has full efficiency for shower generated by particles of energy ≥ 3 EeV. The development of the SD has been completed in 2008. In 2017 a new grid of WCDs has been inserted with a distance of 750 m with each other, covering an area of ~ 25 km², forming the *infill* detector [37]. A part of this area has a full efficiency for the reconstruction of showers generated by cosmic rays of energy $\sim 10^{17}$ eV and more, which is a region of the flux that overlaps with other observatories. This area is also equipped with underground muon detector (AMIGA) [38].

The big advantage of the SD is the opportunity to collect data in all the atmospheric conditions, with a duty cycle of $\simeq 100\%$. On the other side the SD has only the limited information of the front of the shower and loses the information on its longitudinal development.

The WCD station is formed by a cylindrical tank of 3.6 m in diameter and 1.6 m in height filled with $\sim 12\,000$ l of ultra-pure water. The relativistic charged particles of the shower passing by emit photons for Cherenkov effect, which are collected by a system of three photomultiplier tubes (PMTs), observing the water volume from above. To collect all the light emitted the inner surface of each tank is covered with

reflective material.

Each PMT collects the signal using two channels: an AC coupled anode signal and the amplified signal of the last dynode, with 32 times the charge gain of the anode. The second one is called the high gain channel while the first one is the low gain channel, and it is used when the high gain channel is saturated. The maximum signal registered before saturation is around 650 VEM (Vertical Equivalent Muon), which is 650 times the signal left by a vertical muon at the minimum of ionization (it corresponds to the signal of a 10^{20} eV cosmic ray at 500 m of the shower core). In order to record all the information the frequency at which the digital signal is sent is about 40 MHz, with an amplitude of 25 ns.

Each SD station contains a GPS receiver. The absolute timing of the signals in individual WCDs is relevant for reconstructing the shower front and computing the arrival directions of the incoming cosmic rays.

2.1.2 Triggers and reconstruction

To select and reconstruct only real EASs the SD have a hierarchical system of 5 triggers. The first two triggers (T1 and T2) are at the level of the WCDs. T1 triggers either when all three PMTs exceed a threshold signal or on lower signals extended in time. T2 lowers the rate of T1. The signals passing T1 and T2 are sent to the Central Data Acquisition System (CDAS), which perform the other triggers. Since EASs extend in space for several km² a real signal has to trigger more stations at a compatible time. At least three stations in a compact configuration and in a compatible time window are required to form a T3 trigger. Two a posteriori triggers are required to ensure the correct event selection: T4 discards random coincidences of nearby detectors which have triggered on low energy showers, while T5 performs a quality selection.

With the SD we can reconstruct both the inclination of the shower and the energy of the primary particle which generated it.

The inclination of the shower can be found by using the time information of the triggered stations to reconstruct the zenith angle, i.e. the angle formed between the direction of the primary particle, and so the core of the shower, and the vertical. In fact if two detectors i and j are triggered by the same shower we can measure the zenith angle as:

$$\theta = \sin^{-1} \left(\frac{c t_{ij}}{d_{ij}} \right), \quad (2.1)$$

where t_{ij} is the time delay between the two stations being triggered, d_{ij} is the distance between the stations and c is the light speed, as we consider that the shower is formed by ultra-relativistic particles.

The energy reconstruction is based on the fit of the Lateral Distribution Function (LDF), which is a modified version of the Nishimura-Kamata-Greisen (NKG) function describing the lateral development of the shower. The fit is performed using the signal collected in the WCDs. The NKG function used by Auger is:

$$S(r) = S(1000) \times \left(\frac{r}{1000 \text{ m}} \right)^\beta \times \left(\frac{r + 700 \text{ m}}{1000 \text{ m}} + 700 \text{ m} \right)^{\beta+\gamma}, \quad (2.2)$$

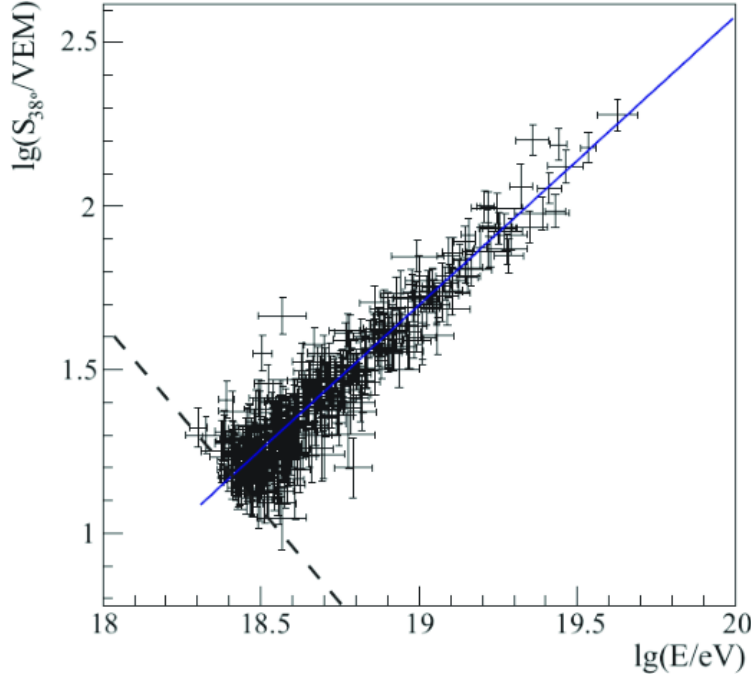


Figure 2.2: Plot reporting the S_{38} line, in blue, as it has been fitted using hybrid events, reported with their error in black, from [39]

where β is a parameter depending on the zenith angle and on the shower dimension, γ is a parameter very close to 0. By fitting this function we extrapolate $S(1000)$ which is the signal at 1000 m from the shower core, this value has been chosen since at this distance the shower fluctuations are minimum.

Unfortunately, the $S(1000)$ depends on the inclination of the shower: inclined showers pass through more atmosphere, so the expected $S(1000)$ is lower than the one generated by vertical showers. Therefore $S(1000)$ has to be corrected using a function ($f_{\text{CIC}}(\theta)$) extracted using a data-driven method called Constant Intensity Cut (CIC) method. From the $S(1000)$ we get the $S_{38} = S(1000)/f_{\text{CIC}}(\theta)$, which is the $S(1000)$ obtained for a shower inclined by an angle $\theta = 38^\circ$, since it is the median value between 0° and 60° .

S_{38} depends only to the energy and it can be used to extract the energy of the primary particle. The absolute energy has been calibrated using the data of the Fluorescence Detector, which reconstructs the energy of the primary particle with a different method, see section 2.2. The relation between the reconstructed energy (E_{FD}) and S_{38} is described by a power-law function,

$$E_{\text{FD}} = A \cdot S_{38}^B. \quad (2.3)$$

By completing the reconstruction of the LDF we can extract also the core of the shower, which allows a better estimation of the zenith angle.

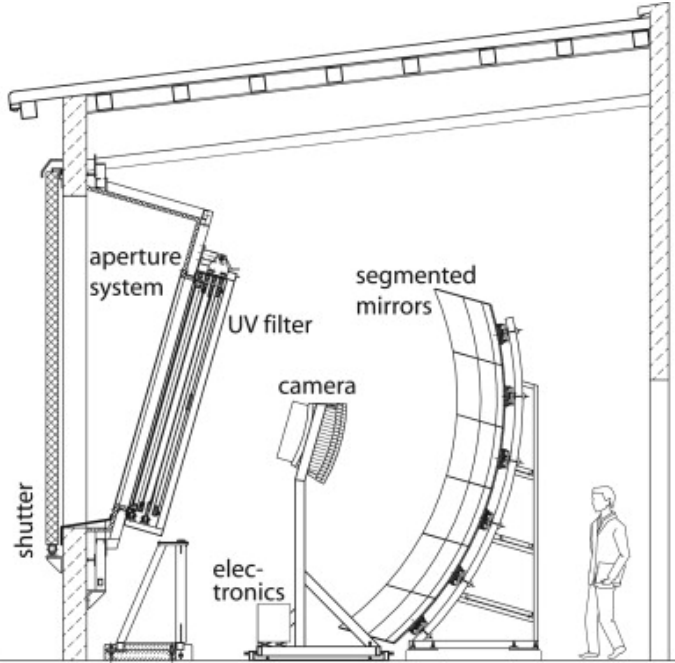


Figure 2.3: Scheme of a fluorescence telescope of the FD

2.2 The Fluorescence Detector (FD)

Charged particles of the shower excite molecules in the atmosphere, their de-excitation emit fluorescence light isotropically. The light is emitted mainly by Nitrogen molecules in the UV band ($\lambda \sim 370$ nm). The Fluorescence Detector reconstructs the longitudinal development of the showers in the atmosphere collecting the fluorescence light emitted [40].

The FD is composed by 27 fluorescence telescopes divided in 5 buildings placed along the perimeter of the SD. The names of the 5 buildings are Los Leones, Los Morados, Loma Amarilla, Coihueco and HEAT. The first four are equipped by 6 telescopes each, covering a field of view from 1° to 31° in elevation, while HEAT is composed by 3 telescopes and can operate in two configurations: DOWN, with a field of view from 1° to 31° in elevation, and UP, with a field of view from 31° to 61° in elevation. The HEAT site has been completed in 2011. Each telescope covers 30° in azimuth and it is equipped with 440 photomultipliers, each with a field of view of $1.5^\circ \times 1.5^\circ$. The telescopes have a circular diaphragm of 1.1 m in radius covered with a filter glass window which only allows the passage of UV light, to improve the signal/noise ratio.

The PMT data are processed with a three stage trigger system, in order to select real events. It should be noticed that, for the FD, the energy threshold for detection depends on the distance and the relative geometry of the shower with respect to the FD building.

With the FD we have a direct information of the shower, but unfortunately the collected light is so feeble that it can work only in specific situation. First of all

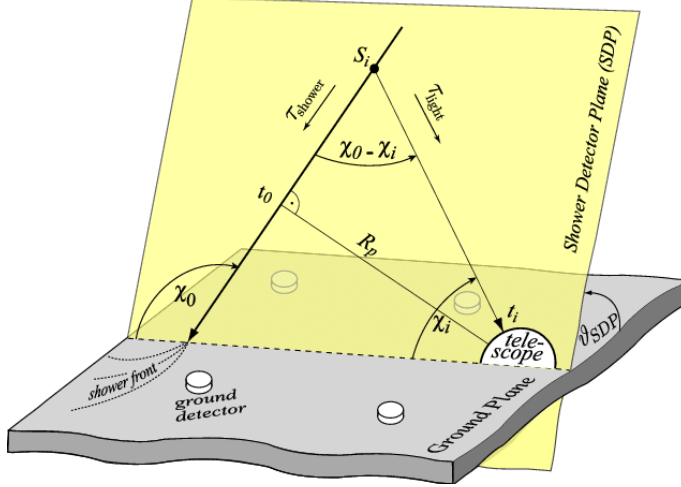


Figure 2.4: Scheme depicting the reconstruction of the arrival direction of the EAS performed by the FD

the FD requires the absence of light, so it can work only in moonless night, then it needs precise weather conditions (low wind, no rain or snow) and lastly it needs the transparency of air. All these limitations reduce FD duty cycle to $\sim 15\%$ [41].

Even with the FD, as with the SD, we can reconstruct both the direction of the shower and the energy of the primary particle.

To reconstruct the direction we measure the angle that the shower core form with the horizontal plane (χ_0), from which then we can find the azimuth angle. The first step is to define the Shower Detector Plane (SDP), which is the plane containing the shower axis and the eye of the telescopes which detected the shower. We then define R_p , the perpendicular distance of the camera to the shower axis. We can now consider the i -th pixel of the telescope, forming an angle χ_i with the horizontal plane. Let t_0 be the time when the shower front on the axis passes the point of closest approach R_p to the camera. The light arrives at the i -th pixel at the time

$$t_i = t_0 + \frac{R_p}{c} \cdot \tan\left(\frac{\chi_0 - \chi_i}{2}\right), \quad (2.4)$$

all the quantities previously described can be seen in fig. 2.4.

The energy reconstruction can be performed after having reconstructed the geometry of the EAS, then the light collected in function of the arrival time can be converted in energy deposited by the shower as a function of the traversed atmospheric depth (X).

We have to convert the light collected in energy deposit using the fluorescence yield. To complete this operation it is crucial a good knowledge of its absolute value as well as its dependence on wavelength, temperature, pressure and humidity. The energy of the primary cosmic ray can be derived by fitting the full longitudinal profile of the energy deposit with the Gaisser–Hillas function to the time profile of

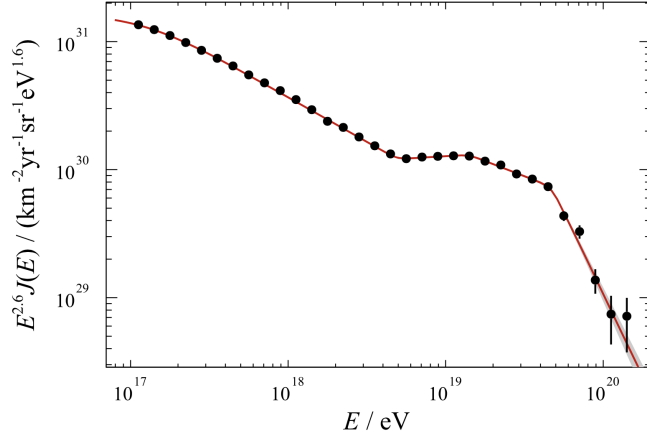


Figure 2.5: Spectrum of the UHECRs as it has been measured by the Pierre Auger Observatory, from [43]

photoelectrons detected in the PMTs

$$N_e = N_{X_{\max}} \cdot \left(\frac{X - X_1}{X_{\max} - X_1} \right)^{\frac{X_{\max} - X_1}{X_0}} \cdot e^{\frac{X_{\max} - X}{X_0}}. \quad (2.5)$$

Finally, the calorimetric energy of the shower is obtained by integrating over the total longitudinal profile. The total energy is estimated by correcting for the *invisible* energy carried away by neutrinos and high energy muons, that do not deposit in the atmosphere, typically it is $\sim 10\%$, as it has been estimated using hybrid data [42].

2.3 Auger results

Operating since 2004 Auger has obtained important results in the UHECR field. With this section I intend to report the major achievements regarding the knowledge on the cosmic ray flux, on their composition and on their arrival directions.

- **Spectrum:** during its lifetime Auger measured accurately the cosmic ray flux starting from the energy of 10^{17} eV, thanks to the *infill* array. The spectrum can be parameterized with the following equation.

$$J = J_0 \left(\frac{E}{E_0} \right)^{-\gamma_0} \frac{\prod_{i=0}^3 \left[1 + \left(\frac{E}{E_{ij}} \right)^{\frac{1}{\omega_{ij}}} \right]^{(\gamma_i - \gamma_j)\omega_{ij}}}{\prod_{i=0}^3 \left[1 + \left(\frac{E_0}{E_{ij}} \right)^{\frac{1}{\omega_{ij}}} \right]^{(\gamma_i - \gamma_j)\omega_{ij}}} \quad (2.6)$$

with $J_0 = 1.309 \text{ km}^{-2} \text{ sr}^{-1} \text{ yr}^{-1} \text{ eV}^{-1}$, $j = i + 1$, E_0 equal to $10^{18.5}$ eV and the parameters $\omega_{ij} = 0.05$ [43].

This function has 4 different spectral indexes, and consequentially three changes in inclination. The first change in the spectral index is at $E_{12} = 4.9 \times 10^{18}$ eV,

which is the *ankle*, and the spectral index pass from $\gamma_1 = 3.298$ to $\gamma_2 = 2.52$. The second change is the *instep* at $E_{23} = 1.4 \times 10^{19}$ eV, when the spectral index becomes $\gamma_3 = 3.08$. The last change, called *toe*, is at $E_{34} = 4.7 \times 10^{19}$ eV, where it has been observed a cut-off with $\gamma_4 = 5.4$. This happens at an energy compatible to the expected GZK cut-off. The observation of this suppression has been really important since the previous experiments, AGASA and HiRes, led to controversial conclusions on its presence. Furthermore the observation of this cut-off permitted to exclude exotic scenarios such as strong Lorentz Invariance Violation. Although being compatible with the GZK cut-off, we do not know yet what causes the last change in the slope: it could be the GZK effect or the sources not able to accelerate further (probably it is a combination of these two effects or an upper limit to the sources acceleration capabilities).

The latest update of all-particle spectrum can be seen in fig. 2.5.

The Observatory can also detect cosmic rays of lower energy taking advantage of an additional infill array, called 433 [44].

- **Mass composition:** the mass of cosmic rays cannot be measured directly by Auger. However we can estimate the atomic number A of the primary cosmic ray considering some properties of the EASs.

For this purpose the Auger Collaboration has focused on the reconstruction of mass-sensitive observables. The two most easily usable are the X_{\max} , which depends on the logarithm of the mass number, and the number of muons in the shower (N_μ). However, the models used to simulate the EASs disagree with N_μ measured from the showers and we do not know if it is a problem due to the simulation or due to the measure of N_μ . Therefore the Auger Collaboration has not been able to use N_μ as primary mass estimator yet. Furthermore, the errors associated to N_μ are important, so it cannot be used as event per event mass estimator yet.

The latest results are reported in fig. 2.6, where it has been reported the evolution of the average value of the X_{\max} in function of the energy and how it is referred to the mass composition [45], according to the result of simulations. As it can be seen the composition of UHECRs is not constant: at low energies the proton contribute dominates the flux, while at higher energies the flux is dominated by heavier nuclei.

The studies on the mass of the primary cosmic rays has been performed using the X_{\max} and, due to fluctuations of the properties of the first interactions, the mass inference is best performed averaging X_{\max} of different EASs. The observatory has not completed a event per event mass estimation, but just a study on the mass distribution in function of the energy.

- **Neutral particles:** in the cosmic ray flux we expect also the presence of neutrinos and photons. Neutrinos can be produced both in GZK interactions or in the interactions of the primary cosmic rays with the background light around their sources (in both cases they should be produced as decay products of

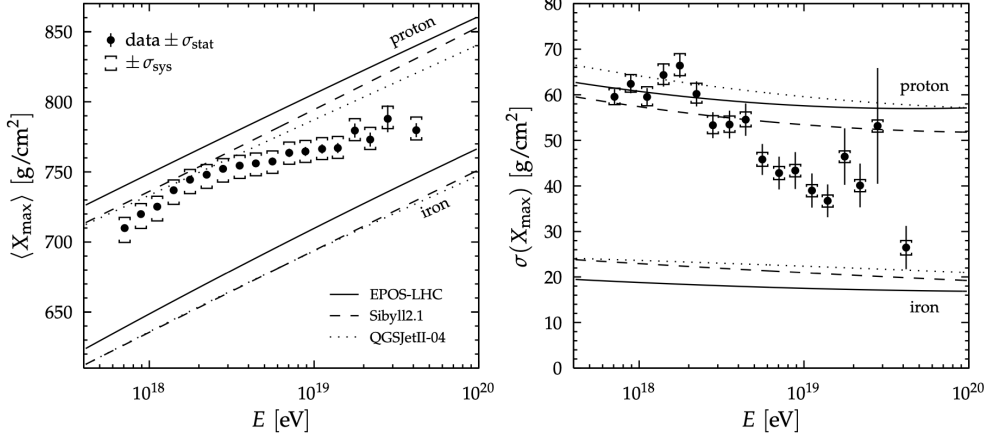


Figure 2.6: First and second moment of the X_{\max} distribution as a function of the primary energy, from [45]

pions). Photons can be produced in GZK interactions, in pion photoproduction or in nuclear inelastic collisions at the sources.

Neutrinos and photons are neutral particles, therefore they are not deflected by the magnetic fields. When they enter the atmosphere Ultra-High Energy photons generates electromagnetic air showers that could be detected at the Pierre Auger Observatory. Also, Ultra-High Energy neutrinos could be detected by Auger: they could generate showers interacting with nuclei, however, since neutrino interaction cross sections are very weak, they would more probably interact very late in the atmosphere (and the showers would be almost horizontal); they could travel across the Earth and interact with a nucleus near the surface, generating a shower coming from the bottom (the so-called Earth-skimming showers) [46]. During its lifetime the observatory did not find any candidate event for both photons and neutrinos, therefore Auger has set the strongest limits on the UHE photons and neutrinos fluxes [47, 48]. The limit on the photons has been important to exclude the so called *top-down* models: cosmic ray production mechanism in which they are generated as a decay of exotic particles, these models foresee an important component of photons in UHECR flux.

- **Arrival directions:** one of the main field in Auger studies has been the arrival direction sector. UHECRs are mainly nuclei deflected by the magnetic fields, so we cannot find directly their sources. However, studying the arrival directions, we can obtain important information on the UHECRs sources. The arrival direction studies have focused in two major areas: the large scale anisotropies and the small scale anisotropies.

The large scale anisotropy studies use a large range of cosmic rays, starting from few EeV. These particles are strongly deflected by the Galactic Magnetic Field. However, using data with energy above 8 EeV the Pierre Auger Collaboration

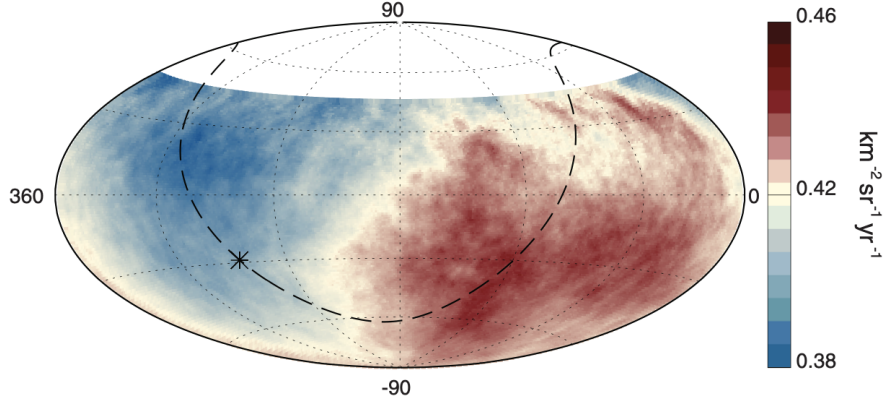


Figure 2.7: Sky map in equatorial coordinates showing the UHECR flux integrated in energy as it has been measured by Auger as a function of the arrival direction of the cosmic rays, from [5]

observed a dipole anisotropy directed away from the Galactic Center with a significance level of 6.6σ , this points out the extragalactic origin of most of the UHECRs at these energies [5]. The map showing the arrival directions for cosmic rays with energy above 8 EeV is reported in fig. 2.7

The small-scale anisotropy studies focus on more energetic, less deflected particles. Using data with energy above 32 EeV studies of correlation with astrophysical catalogues have been made, finding out a correlation with a post-trial significance of 4.4σ with a catalog of starburst galaxies [49]. This correlation is mostly driven by a warm spot in the direction of the Centaurus constellation ($\sim 4\sigma$). This region contains two close and prominent starburst galaxies (M83 and NGC4945) but also the nearest AGN to the Earth (Centaurus A).

- **Combined fit:** in 2023 the Auger Collaboration performed a combined fit to constrain the physical parameters related to the energy spectrum and the mass composition of particles escaping the environments of extra-galactic sources, in order to reproduce the observed UHECR spectrum at the Earth [50]. This fit has been performed considering two extra-galactic components: one at low energies (LE) and one at high energies (HE). In addition, it has been considered a first scenario in which there is a galactic component (SCENARIO 1) and a second one in which the spectrum can be explained using only an extra-galactic origin (SCENARIO 2). The combined fit was performed defining the spectrum emitted for particles with mass number A per comoving volume, per time (\tilde{Q}_A). The emission for all the particles is $\tilde{Q} = \sum \tilde{Q}_A$.

To find the associated flux observed at the Earth some SIMPROP [51] simulations have been performed. The energy losses considered in the propagation are the adiabatic loss due to the expansion of the universe and the interactions with the photon background, mainly the Cosmic Microwave Background

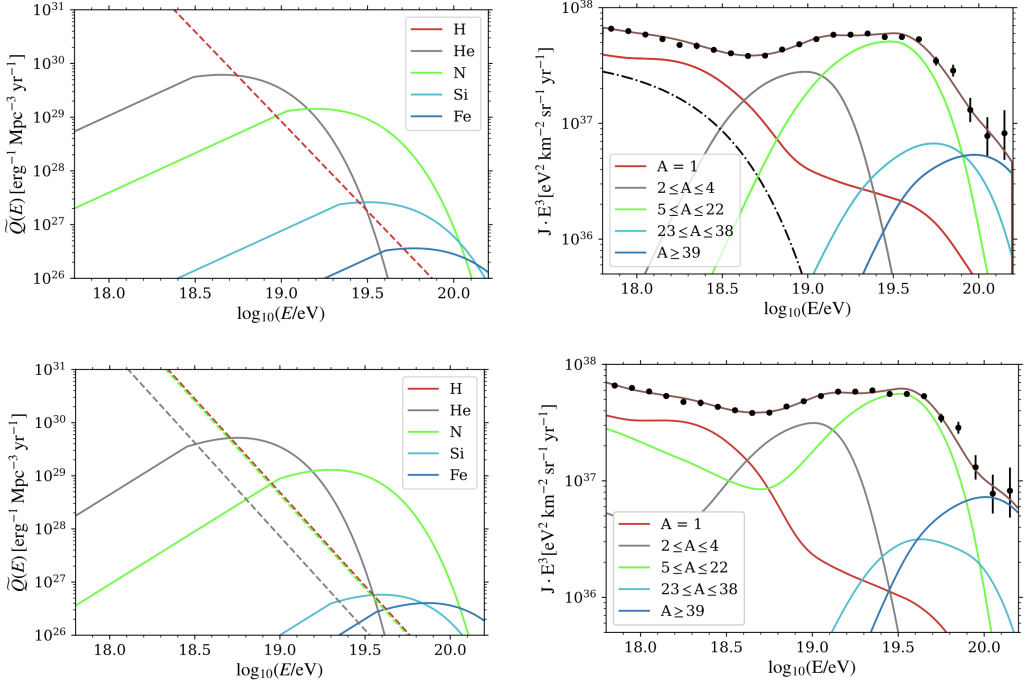


Figure 2.8: **Top:** Spectrum emitted by the sources for the various atomic species considered in the combined fit (left) and their contribution to the observed spectrum at the Earth (right) in SCENARIO 1. **Bottom:** Same as above but for SCENARIO 2

(CMB) and the Extra-galactic Background Light (EBL). The observed flux is obtained by

$$J_{\text{obs}}(E) = \frac{c}{4\pi} \sum_A \sum_{A'} \int \int dE' dz \left| \frac{dt}{dz} \right| S(z) \tilde{Q}_A(E') \frac{d\eta_{AA'}}{dE}(E, E', z). \quad (2.7)$$

In eq. (2.7) $S(z)$ is the evolution of the luminosity of UHECRs with z (where z is the gravitational redshift), $\eta_{AA'}(E, E', z)$ expresses the probability to produce a nucleus with A atomic mass and energy E from one with atomic mass A' and energy E' and dt/dz describes the relationship between the expansion of the Universe and the redshift, it can be expressed by

$$\frac{dz}{dt} = -H_0(1+z)\sqrt{\Omega_m(1+z^3) + \Omega_\Lambda}, \quad (2.8)$$

$H_0 = 70 \text{ km s}^{-1} \text{ Mpc}^{-1}$ is the Hubble constant, $\Omega_m = 0.3$ describes the dark matter contribution and $\Omega_\Lambda = 0.7$ describes the dark energy contribution.

In fig. 2.8 the plots regarding the results of the fit are reported.

Chapter 3

Magnetars

With this chapter I intend to present why magnetars should be considered among the UHECR accelerators, giving a detailed model for the acceleration of cosmic rays.

Magnetars are a peculiar type of Neutron Stars (NSs), characterized by very intense magnetic fields, of $\mathcal{O}(10^{14} - 10^{15})$ G (to have a comparison the field of a fridge magnet is ≈ 100 G). They have a rotational period quite large compared to other class of NSs, with typical values of $\mathcal{O}(1)$ s. However, magnetars should be born with rotational periods way smaller than the one observed, of $\mathcal{O}(10^{-3})$ s. During the first stages of their life magnetars dissipate important energy contributes, leading to a possible acceleration of UHECRs, which theoretically could reach $\sim 10^3$ EeV. Furthermore, magnetars are among the most energetic and most exotic objects in the known Universe, and their study could give us important information of matter at densities of the order of nuclear densities.

In this chapter I first complete a review on Neutron Stars in general, then I focus completely on magnetars, explaining what is the actual knowledge on their physics and a proposed model for the acceleration of UHECRs.

3.1 Neutron Stars

Neutron Stars are compact objects formed in type II core-collapse Supernova explosions of stars of high mass ($9 M_\odot \lesssim M \lesssim 30 M_\odot$) [52]. The mechanism of these explosions was firstly proposed by Bethe and Brown in 1985 [53].

Type II core-collapse Supernovae are neutrino bombs supported by the gravitational energy of the star. During their life stars form massive nuclei, making nuclear fusion with lighter one, until they reach ^{56}Fe , which is the nucleus with the highest binding energy. After having formed iron, a star can not free energy by creating heavier nuclei, therefore it starts to contract, first, and collapse, then, after its own gravity. During the first phase the iron core of the star contracts, passing from a radius of $\approx 10^9$ cm to a radius of $\approx 10^7$ cm, forming a so-called Proto-Neutron Star (PNS). During this phase the difference in gravitational energy is

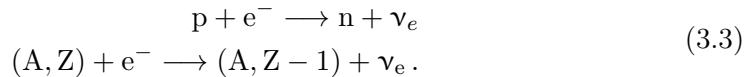
$$\Delta E = \frac{GM^2}{R_i} - \frac{GM^2}{R_{\text{PNS}}} \simeq 10^{52} \text{ erg}, \quad (3.1)$$

the result is obtained considering a mass M of $1 M_{\odot}$.

During this first phase, for the virial theorem, the contracting iron core increases its temperature and a process of photodissociation of the nuclei begins.



At the same time two types of neutrino emission happen: thermal neutrino emission and neutronization. In the first one a couple, real or virtual, of e^- and e^+ annihilates. These interactions do not change the leptonic number of the system and they are the main interactions inside a PNS, when the neutrinos are trapped within matter. The second set of interactions are electronic captures which can happen both on protons and nuclei



When neutrinos produced by these interactions escape from the system they reduce the leptonic number, taking away pressure.

While collapsing, the density of the system increases. Therefore the free path ($l = 1/\sigma n$, where σ is the interaction cross section and n is the matter numerical density) of the neutrinos decreases. Therefore when the PNS reaches a density of $\rho \simeq 3 \times 10^{11} \text{ g/cm}^3$, neutrinos become trapped inside of the system. As a consequence of that, the weak interactions are in equilibrium and, since neutrinos cannot escape the system, the leptonic number does not change anymore. Protons are collected in neutron rich nuclei, which remain until the saturation density is reached (which is the density of nuclear matter $\simeq 2.8 \times 10^{14} \text{ g/cm}^3$). The inner part of the system undergoes a phase of adiabatic and homologous collapse. At the border of the collapsing core the system begin to bounce back and oscillate, forming a shock wave which detaches the envelope of the original star and gives kinematic energy to the ejecta. Actually, the original shock wave stalls passing the iron layers but it gets revitalized by the neutrinos freed from the core at the end of the collapsing process.

The remnant of this explosion is a neutron star, which in its first stage is still a hot object, T of $\mathcal{O}(10^{11} - 10^{12}) \text{ K}$. It cools down in circa a week reaching $\sim 10^9 \text{ K}$. While being called "neutron" stars, they are composed both by nucleons and electrons. The electrons inside of them are ultra-relativistic and degenerate, while nucleons are classical and degenerate. The mass of a NS is of the order of a solar mass, but the radius is way shorter; a typical NS radius is $\approx 10 \text{ km}$, while the solar radius is $\approx 700 000 \text{ km}$.

To understand the mechanics of a neutron star, we can define the adimensional potential

$$\Phi_{\text{ad}} = \frac{GM}{Rc^2}, \quad (3.4)$$

which for a neutron star is $\simeq 0.1 - 0.2$. The adimensional potential describes how much relativistic a system is: the more it is close to 1 the more relativistic a system is.

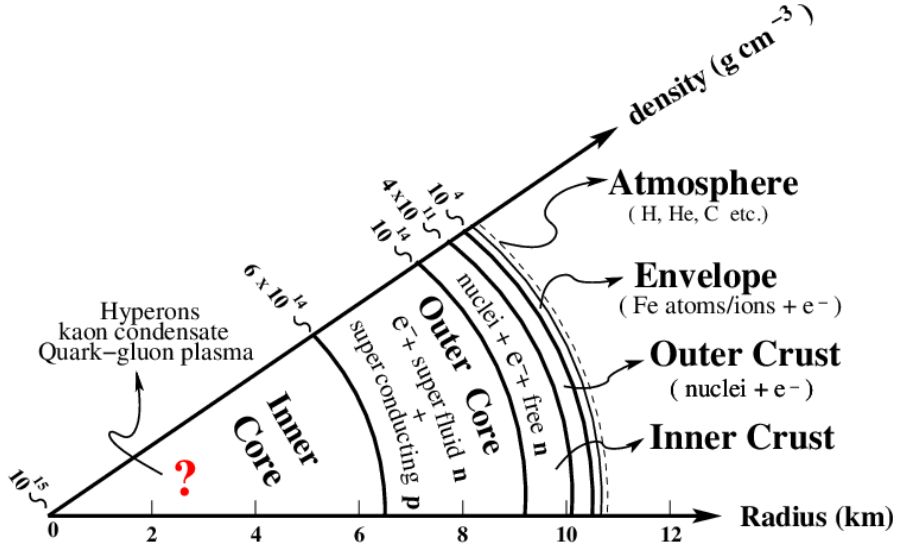


Figure 3.1: Scheme of the inner layers of a neutron star, from [54]

Differently from classical stars, and also from white dwarves, the adimensional potential is not $\ll 1$, therefore the hydrostatic equilibrium of a neutron star is described using the Tolman-Oppenheimer-Volkoff equation

$$\frac{dP}{dr} = -\frac{Gm(r)}{r^2}\rho(m)\left(1 + \frac{4\pi r^3 P(r)}{m(r)c^2}\right)\left(1 + \frac{P(r)}{\rho(r)c^2}\right)\left(1 - \frac{2Gm(r)}{rc^2}\right)^{-1} \quad (3.5)$$

In this equation the pressure (P) enhances the effect of the gravity, therefore there is a limit on the maximum mass which can be sustained by a self-gravitating object.

By imposing the following three conditions a variational study has been performed to estimate the maximum mass of a self-gravitating object.

- (i) General Relativity is the right gravitational theory
- (ii) $dP/d\rho > 0$, that is the microscopic stability
- (iii) $dP/d\rho < c^2$, that is causality of the sound speed

By assuming (i), (ii) and (iii) $M_{\max} \simeq 3 M_\odot$, while by assuming just (i) and (ii) $M_{\max} \simeq 5 M_\odot$.

The maximum value of a self-gravitating object is obtained considering an non compressible object, i.e. considering the density constant along the radius. However, NSs present a stratified structure, reported in fig. 3.1, in which the density increases going deep in the star. The different phases can be catalogued as follow [55]:

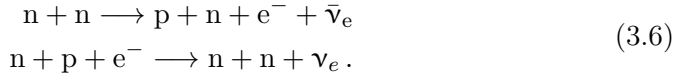
- (i) the *envelope* ($\rho \leq 10^6 \text{ g/cm}^3$), it is a region in which the temperature and the magnetic fields can affect the equation of state. The surface is populated by ^{56}Fe ;

- (ii) the *outer crust* ($10^6 \text{ g/cm}^3 \leq \rho \leq 4.3 \times 10^{11} \text{ g/cm}^3$), a region populated by neutron rich nuclei in a *bcc* lattice structure and a relativistic degenerate electron gas
- (iii) the *inner crust* ($4.3 \times 10^{11} \text{ g/cm}^3 \leq \rho \leq (2 - 2.4) \times 10^{14} \text{ g/cm}^3$) in which there is *neutron drip*. The region is formed by a lattice of neutron rich nuclei and a superfluid neutron gas
- (iv) the *outer core* ($((2 - 2.4) \times 10^{11} \text{ g/cm}^3 \leq \rho \leq \rho_{\text{sat}})$, it contains mainly superfluid neutrons with small concentration of superfluid protons and electrons
- (v) the *inner core* ($\rho \geq \rho_{\text{sat}} = 2.8 \times 10^{14} \text{ g/cm}^3$). This is a region we can only theorize about, since the density is above the density of nuclear matter. There could be pion condensation, or a transition to a neutron solid, or to quark matter, or some other phase physically distinct from a neutron liquid

3.2 Classification of Neutron Stars

The NSs are distinguished based on the mechanism of energy loss [56]:

- **Thermal NSs:** their energy source is the thermal energy left in the object. They have surface temperature of $\simeq 10^6 \text{ K}$. The cooling of the star is carried on by the escaping neutrinos, which can be produced in degenerate matter with the modified URCA interactions



In this NS, the neutrino free path is $\simeq 500 \text{ km}$, so the neutrinos produced can escape the star and free energy. Three epochs of cooling can be distinguished: the first one is the core relaxation epoch, during which the surface temperature does not change; the second one is a neutrino cooling epoch, which is dominated by the emission of neutrinos, it can be a standard cooling or a rapid cooling, the rapid cooling is quite vertical but can happen only in exotic matter; after $\sim 10^5 \text{ yr}$, the last phase is a cooling dominated by the emission of photons.

- **Rotational Powered Pulsars (RPP):** this is a class of NSs whose energy loss is mainly given by the rotational energy. They are characterized by three features:

- (i) they emit periodic pulsation in the range $1.4 \text{ ms} \leq P \leq 10 \text{ s}$. The period (P) has been measured to be precise even to a part in 10^{13}
- (ii) the period increases in time ($dP/dt = \dot{P} < 0$)
- (iii) the pulsations can be in a single band or in all the electromagnetic spectrum

They have been identified as rotating NSs with intense magnetic field $B \simeq 10^{11} - 10^{12} \text{ G}$.

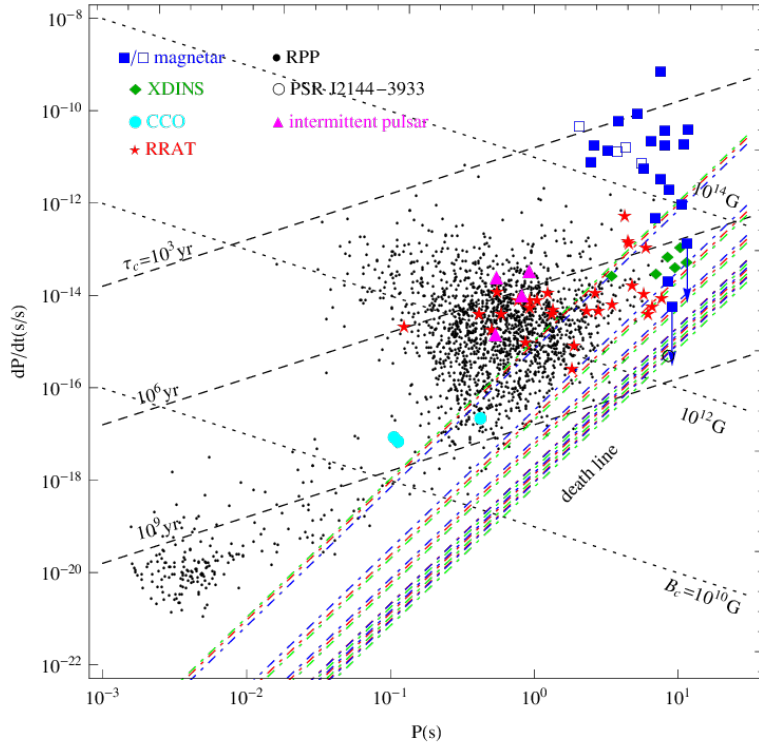


Figure 3.2: $P - \dot{P}$ diagram which expresses the period time derivative and the period of the known neutron stars, from [57]

- **NSs in binary system:** in these systems the neutron star accretes from the companion and emit in the X-ray band
- **Magnetars:** these are a peculiar type of rotating neutron stars whose energy source is not the rotational energy but the strong magnetic field at the surface (the typical intensity is of $\mathcal{O}(10^{14} - 10^{15})$ G). Since magnetars are central in this work the next section is completely dedicated to them.

3.3 Magnetars

Magnetars are a class of young neutron stars which have great variability across the electromagnetic spectrum (particularly at X-ray and soft γ -ray energies), ranging from few millisecond bursts to major month-long outbursts [58]. Some magnetar outbursts include X-ray and soft γ -ray flares that briefly outshine the entire cosmic hard X-ray sky put together.

As previously said, magnetar emission is not powered by the rotational energy of the neutron star but by the decay of enormous internal magnetic fields.

Historically, magnetars first appeared in astronomy under names Soft Gamma Repeaters (SGRs) and Anomalous X-ray Pulsars (AXPs), as initially it was unclear that they represented the same astrophysical object.

In 1998, the first measurement of an SGR spin-down rate was reported and both its sign and magnitude (SGR 1900+14) [59] provided stunning confirmation of the magnetar model predictions, which was proposed by Duncan and Thompson in 1992 [60–62]. Considering the magnetar as a magnetic dipole braking, its magnetic field can be estimated as $B = 3.2 \times 10^{19} \sqrt{P\dot{P}} \text{ G}$. For SGR 1900+14 it was inferred a field strength of $\sim 8 \times 10^{14} \text{ G}$.

Magnetars are, without exception, spinning down, with spin-down rates that imply spin-down time scales ($\sim P/\dot{P}$) of a few thousand years, thus they are young among neutron stars. The spin-down luminosity is usually far smaller than the persistent quiescent X-ray luminosity of the sources.

After SGR 1900+14 other spin down rates were measured and they imply, for 20 out of 23 of the known sources, $B > 5 \cdot 10^{13} \text{ G}$, with the vast majority over 10^{14} G .

In fig. 3.2 it was reported the so-called $P - \dot{P}$ diagram, which reports the known neutron stars according to their periods and their first time-derivative periods. The magnetars are mostly collected in the top right corner, meaning they are characterized both by a big P and \dot{P} . However most of the radio pulsars are thought to be born with periods of at most a few hundred milliseconds, therefore magnetars should pass a rapid braking period in which they lose lot of their energy. This energy loss could be the basis for the acceleration of the UHECRs in the new birth magnetars.

3.4 Pulsar and magnetar age

One of the central parameter for this thesis work is the age of the considered magnetars. The age of the neutron stars can be obtained assuming a model for the energy loss of the object. What I present in this section is the oblique rotator model in vacuum, which can describes the behaviour of a rotating neutron star with a dipolar magnetic field not orientated along the rotational axis and whose main energy loss is the rotational energy loss. This model applies quite well to pulsars and can be applied also to magnetars. For magnetars, we have mentioned that the primary energy loss is due to the strong magnetic field, however we have also a significant energy loss due to rotational energy. Therefore the age we obtain from this model, called *characteristic age* is a good age estimation for pulsars and an upper limit for magnetars. Since in literature the characteristic age is often used as an estimation of the magnetar age, I will use it also in this work.

The oblique rotator model consider a neutron star with rotational speed $\boldsymbol{\Omega}$ and a central magnetic dipole $\boldsymbol{\mu}$ forming an angle θ versus the vector $\boldsymbol{\Omega}$. The polar magnetic field can be estimate as

$$B_p = \frac{2\mu}{R^3}. \quad (3.7)$$

We can choose now an inertial framework whose versors are $\hat{e}_{||}$ (which is aligned to $\boldsymbol{\Omega}$) and \hat{e}_{\perp_1} and \hat{e}_{\perp_2} , which are oriented in the perpendicular plane. We can write the magnetic dipole as

$$\boldsymbol{\mu} = \frac{B_p R^3}{2} (\cos(\theta) \hat{e}_{||} + \sin(\theta) \sin(\Omega t) \hat{e}_{\perp_1} + \sin(\theta) \cos(\Omega t) \hat{e}_{\perp_2}). \quad (3.8)$$

From the Larmor law we can derive the emitted power

$$\frac{dE}{dt} = \frac{2}{3c^2} \left| \frac{d^2}{dt^2} \mu \right|^2, \quad (3.9)$$

we can evaluate the second derivative of the magnetic dipole and find

$$\frac{d^2}{dt^2} \mu = -\frac{1}{2} B_p R^3 \Omega^2 \sin(\theta) (\sin(\Omega t) \hat{e}_{\perp_1} + \cos(\Omega t) \hat{e}_{\perp_2}), \quad (3.10)$$

therefore the power emitted in this model is

$$\frac{dE}{dt} = \frac{1}{6c^3} B_p^2 \sin^2(\theta) R^6 \Omega^4. \quad (3.11)$$

Considering now that all the energy loss is due to the loss in kinematic energy we can say

$$\frac{dE}{dt} = \frac{dK}{dt} = -I \Omega \dot{\Omega}, \quad (3.12)$$

where I is the inertial moment of the star and $\dot{\Omega}$ is the first derivative of the rotational energy. Now equating the last two equations we get that

$$\dot{\Omega} = -\frac{1}{6c^3 I} B_p^2 \sin^2(\theta) R^6 \Omega^3 = -\alpha \Omega^3. \quad (3.13)$$

We can focus now on the equation $\dot{\Omega} = -\alpha \Omega^n$, remembering that in this case $n = 3$. The parameter α can be measured starting from observations of the neutron star, defining $\alpha = -\dot{\Omega}_0 / \Omega_0^n$, where $\dot{\Omega}_0$ and Ω_0 are values measured on the star.

We can now integrate the above equation between the birth time of the neutron star and now

$$\begin{aligned} \int_{\Omega_i}^{\Omega_0} \frac{d\Omega}{\Omega^n} &= \int_0^{t_0} \frac{\dot{\Omega}_0}{\Omega_0^n} dt \\ \frac{1}{1-n} \left(\frac{1}{\Omega_0^{n-1}} - \frac{1}{\Omega_i^{n-1}} \right) &= \frac{\dot{\Omega}_0}{\Omega_0^n} t_0. \end{aligned} \quad (3.14)$$

By assuming $\Omega_0 \ll \Omega_i$ we have

$$t_0 = \frac{1}{1-n} \frac{\Omega_0}{\dot{\Omega}_0}, \quad (3.15)$$

and remembering that in this model $n = 3$ we can define the characteristic age as

$$\tau_c = \left| \frac{\Omega_0}{2\dot{\Omega}_0} \right|, \quad (3.16)$$

in this model n can be measured directly to verify if it is equal to 3. By deriving $\dot{\Omega}$ we can find

$$\frac{d\dot{\Omega}}{dt} = \ddot{\Omega} = -n\alpha\Omega^{n-1}\dot{\Omega} = n \frac{\dot{\Omega}^2}{\Omega}, \quad (3.17)$$

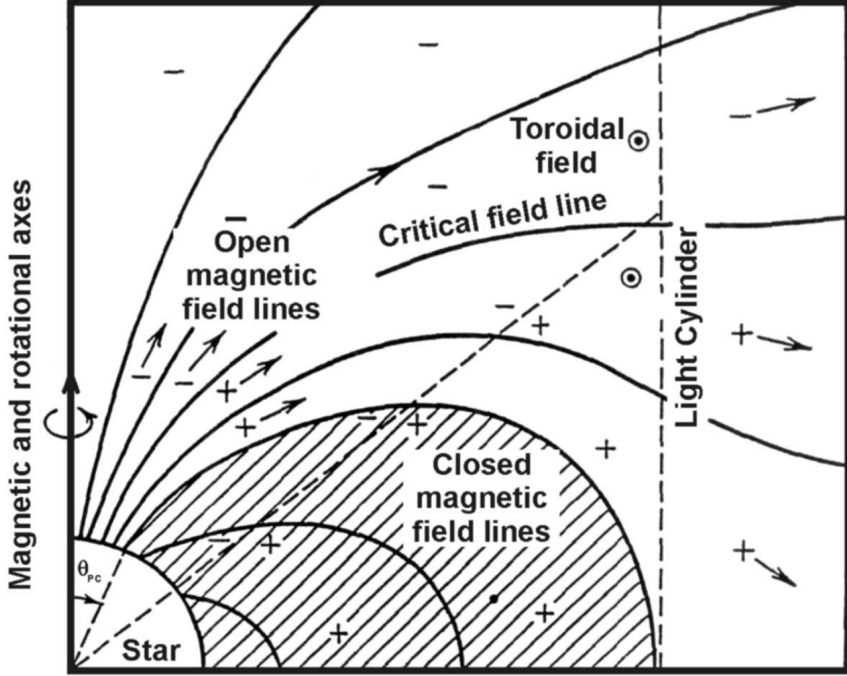


Figure 3.3: Scheme of a neutron star in the oblique rotator model

therefore $n = \ddot{\Omega}\Omega/\dot{\Omega}^2$. Due to the phenomenon of glitches (rapid spin-up in the rotational speed) the measure of $\ddot{\Omega}$ is quite difficult and it is hard to obtain a precise value of n .

Goldreich and Julian [63] pointed out that this model is not stable, since the rotation of μ induces strong electric fields on the surface of the NS, filling with particles the magnetosphere, a zone outside the star passed by the lines of force of the magnetic field. They proposed a modified model which gives a energy loss $dE/dt \propto \Omega^4$, i.e. the same behaviour as the oblique rotator model. They defined the light cylinder, an ideal cylinder around the NS where the particle co-rotating with it have speed equal to the light speed. The radius of this surface is

$$R_L = \frac{c}{\Omega}. \quad (3.18)$$

The area around the star can be divided in two areas: the near zone ($r \ll R_L$) and the far zone ($r \gg R_L$). The magnetic field in the near zone is dipolar, with

$$B(r) = B_p \left(\frac{R}{r} \right)^3, \quad (3.19)$$

while in the far zone there is a radiation field with $\mathbf{E} \sim \mathbf{B}$. The module of the Poynting vector is

$$s = c \frac{B(r)^2}{4\pi}, \quad (3.20)$$

and the energy loss is

$$\frac{dE}{dt} = 4\pi r^2 s = cr^2 B(r)^2. \quad (3.21)$$

A figurative representation of the magnetic field of a NS in this modified model can be found in fig. 3.3.

The two solutions for the energy loss have to be equal in the turning point which is at $r = R_L$

$$\frac{dE}{dt} = cR_L^2 B(R_L)^2 = \frac{R_L^6 B_p^2}{c^3} \Omega^4. \quad (3.22)$$

The energy loss is still proportional to Ω^4 , therefore the previous calculation can be repeated to find that also in this model τ_c represents a measure of the age of a NS.

3.5 Magnetars as UHECR accelerators

In this section I present the model proposed by J. Arons in 2003 in which magnetars are considered as candidate UHECR accelerators [64]. This model differs from the mechanism reported in section 1.4.1, since it predicts a linear acceleration, rather than a Fermi type acceleration, in which particles are accelerated by the electromagnetic fields of the magnetar's wind.

The model is treated first from an energetic point of view, then the interactions leading the acceleration are depicted. All the following equations are written in cgs system.

A magnetar can be considered as a relativistic oblique magnetic rotator with a dipolar magnetic moment μ , rotational speed Ω and angle within the two vectors θ . Across the magnetic field the magnetosphere voltage drops are

$$\Phi_{mag} = \frac{\Omega^2 \mu}{c^2}, \quad (3.23)$$

which govern the particle acceleration. However, if a particle is accelerated inside the magnetosphere, the radiation losses are catastrophic. This can be seen considering the radiative power of a charged particle moving on path with curvature radius ρ_c , which is

$$P = \frac{2}{3} \left(\frac{q^2 c}{\rho_c^2} \right) \left(\frac{E}{mc^2} \right)^4, \quad (3.24)$$

this means that the particles can not be accelerated further than

$$E_{rad} \approx 10^{16.5} \left(\frac{A^2}{Z} \right)^{\frac{1}{3}} \left(\frac{\Omega}{10^4 \text{ s}^{-1}} \right)^{\frac{1}{3}} \left(\frac{r}{R_L} \right)^{\frac{1}{3}} \left(\frac{\rho_c}{r} \right)^{\frac{2}{3}}, \quad (3.25)$$

therefore particles can not reach the Ultra-High Energies.

At $r \gg R_L$ the situation changes drastically, since here the curvature radii ρ_c of highly accelerated ions can exceed significantly the distance r from the magnetar. Furthermore the magnetar is characterized by *non – radiative* relativistic outflows, including wound-up magnetic fields and plasma, which support an electric field \mathbf{E}_\perp .

By considering that the wind is relativistic, $B \approx B(R_L)(R_L/r)$ and $\mathbf{E}_\perp = -(1/c)\mathbf{v} \times \mathbf{B}$, we can evaluate the cross field voltage of the wind as

$$\phi_{\text{wind}} \approx rE_\perp = rB(r) = R_L B(R_L) = \phi_{\text{mag}}, \quad (3.26)$$

therefore the voltage generated by the magnetar is available to accelerate particles at $r >> R_L$.

Each particle passing through the wind gains a fraction η of the total energy

$$E(\Omega) = q\eta\phi_{\text{mag}} = q\eta \frac{\Omega^2 \mu}{c^2}. \quad (3.27)$$

Now, considering the energy loss of the magnetar, we can find the flux of UHECRs emitted. The electromagnetic rate of rotational energy loss is

$$\dot{E}_{\text{EM}} = \frac{4}{9} \frac{\Omega^4 \mu^2}{c^3}. \quad (3.28)$$

The electromagnetic fields are sustained by beams of charged particles extracted from the rotating object, forming the conduction currents

$$\begin{aligned} \dot{E}_R &= I\phi_{\text{mag}} = qc\dot{N}\phi_{\text{mag}} \\ \dot{N} &= c \left(\frac{\Omega B_p}{2\pi c} \right) (2\pi A_{\text{cap}}) = c\rho_{\text{GJ}}(2\pi A_{\text{cap}}), \end{aligned} \quad (3.29)$$

A_{cap} is the area of the magnetic polar cap and it is equal to $\pi(\Omega R/c)R^2$. ρ_{GJ} represents the Goldreich-Julian charge density, which is the number of elementary charges per unit volume such that parallel electric fields are shorted out in the magnetosphere.

The currents in stars with dipolar magnetic fields include a primary electron beam emitted in the polar cap. This is the Goldreich-Julian current

$$I_{\text{GJ}} = 2A_{\text{cap}}c\rho_{\text{GJ}} = \frac{\Omega^2 \mu}{c} = c\phi_{\text{mag}}. \quad (3.30)$$

The energy rate in Eq. (3.28) and Eq. (3.29) can now be matched using I_{GJ} .

The current emanating from the polar cap must be balanced on average by an electric return current. Starting from the observation completed on the Pulsar Wind Nebulae the idea is that this current is an outflowing beam of positive charged particles (i.e. ions). These ions will represent the UHECR flux accelerated by the magnetar, and considering a process with η as efficiency, the energy rate emitted in cosmic rays is

$$\dot{E}_{\text{ions}} = I_{\text{GJ}}\eta\phi_{\text{mag}}. \quad (3.31)$$

Both ϕ_{mag} and I_{GJ} depend on Ω^2 , therefore UHECRs will be mostly emitted in the first phase of a magnetar life, when the rotational speed is sufficiently high. By defining Ω_i the initial rotational speed of the magnetar we can find the initial spin-down time as

$$\tau_{\text{EM}} = \frac{(1/2)I\Omega_i^2}{\dot{E}_{\text{EM}}} = \frac{9}{8} \frac{Ic^3}{\mu^2\Omega_i^2}, \quad (3.32)$$

therefore the UHECR magnetar injection is

$$N_i \sim \dot{N}_{GJ}(\Omega_i) \tau_{EM}(\Omega_i) = \frac{Ic^2}{Ze\mu}, \quad (3.33)$$

in the last two equations I is the inertial momentum of the magnetar.

In this model highly rotating magnetars, with initial rotational speed of $\mathcal{O}(10^4) \text{ s}^{-1}$, with surface magnetic field of $\mathcal{O}(10^{15}) \text{ G}$ can emit protons up to $\mathcal{O}(10^{21}) \text{ eV}$.

Now, the spectrum emitted by an isolated magnetar can be estimated. Considering that the magnetar, in a period dt , passes from angular speed $\Omega(t)$ to $\Omega(t+dt)$. The number of particles accelerated is

$$-dN_i = \dot{N}_i[\Omega(t)]dt = \dot{N}_i \frac{dt}{d\Omega} \frac{d\Omega}{d\Gamma} d\Gamma \quad (3.34)$$

Where Γ is the Lorentz factor, since the energy of an accelerated particle is $m\Gamma(\Omega)c^2$. Now, considering the energy loss of the magnetar, we have

$$\frac{d\Omega}{dt} = \dot{\Omega} = -\frac{\dot{E}_R}{I\Omega} = -\frac{\dot{E}_{EM} + \dot{E}_{grav}}{I\Omega}, \quad (3.35)$$

\dot{E}_{EM} is the electromagnetic energy loss, while \dot{E}_{grav} is the energy lost by gravitational waves. Considering the equatorial ellipticity ϵ of the magnetar we have

$$-\dot{E}_{grav} = \frac{32}{5} \frac{GI^2\epsilon^2\Omega^6}{c^5}, \quad (3.36)$$

and the initial spin-down rate due to gravitational waves is

$$\tau_{GW} = \frac{(1/2)I\Omega_i^2}{-\dot{E}_{grav}}. \quad (3.37)$$

We can rewrite eq. (3.35) as

$$-\dot{\Omega} = \frac{4}{9} \frac{\mu^2\Omega^3}{Ic^3} \left[1 + \left(\frac{\Omega}{\Omega_g} \right)^2 \right], \quad (3.38)$$

where Ω_g is the angular speed at which gravity losses and electromagnetic losses are equal

$$\Omega_g = \left(\frac{5}{72} \frac{c^2\mu^2}{GI^2\epsilon^2} \right). \quad (3.39)$$

The spectrum of accelerated particle is

$$\frac{dN_i}{d\Gamma} = \frac{dN_i}{dt} \left(-\frac{dt}{d\Omega} \right) mc^2 \frac{d\Omega}{dE} = \frac{9}{4} \frac{c^2 I}{Ze\mu\Gamma} \left(1 + \frac{\Gamma}{\Gamma_g} \right)^{-1}, \quad (3.40)$$

where Γ_g is the "gravitational" energy of the particle

$$E_g = m_i c^2 \Gamma_g = \frac{Z\eta e\mu}{c^2} \Omega_g^2 = \frac{5}{72} \frac{Z\eta e\mu^3}{GI^2\epsilon^2}. \quad (3.41)$$

By using this model, making only energetic assumptions, we have been able to write the energetic spectrum of an isolated magnetar. We can now consider the mechanism from a mechanical point of view, describing how the cosmic rays are accelerated by the magnetar wind.

Magnetars are formed in Type II Supernovae and when a highly rotating magnetar is formed, it loses much of its rotational energy before the envelope of the Supernova can be ejected. While losing rotational energy the magnetar emits a relativistic wind which can accelerate particle as seen in eq. (3.40). However, the expanding wind will interact with the envelope, and therefore the actual cosmic ray acceleration can happen only if the energy loss is negligible.

Initially, the magnetar emits electromagnetic energy at a prodigious rate and fills the cavity within its surface and the envelope with "lightweight" relativistic energy. During this phase the radiation absorbs the energy of any accelerated particle. This radiation will lead to the shredding of the envelope with the radiation pressure, which happens quickly.

The radiation creates a pressure on the inner unstable surface of the envelope and "buoyant" bubbles of lightweight energy can rise through the shell. When these bubbles break through the expanding envelope the shredding happens. During this phase most of the envelope material is contained in a layer of thickness ΔR comparable to the radius of a proto-neutron star. This process is not so energy consuming, leaving an important part of the electromagnetic energy free to escape and to form the relativistic wind and the Magnetar Wind Nebula (MWN).

The material of the envelope is non relativistic while the radiation fields and the particle emitted by the magnetar are relativistic. When the two materials meet each other, a mixing of the two species happens, via Kelvin-Helmholtz instabilities. However the non-relativistic matter mixes into only a small fraction, therefore even in this process only a small part of the energy of the wind is lost. After having shredded the envelope and mixed the two components, the radiation emitted maintains $\sim 60 - 70\%$ of its original energy.

In this environment UHECRs are most likely accelerated surf-riding the relativistic outflowing electromagnetic fields. When these electromagnetic fields dominate the outflow's energy density, the magnetosphere and the outflows themselves can be considered as force-free, therefore

$$\rho_q \mathbf{E} + \frac{1}{c} \mathbf{J} \times \mathbf{B} = 0, \quad (3.42)$$

where ρ_q is the charge density, while \mathbf{J} is the current density. In this assumption the electric and magnetic field can be described as

$$B_r = \pm \frac{M}{r^2}, \quad B_\phi = \mp \frac{M \sin(\theta)}{r R_L} \quad (3.43)$$

$$E_\theta = B_\phi \quad (3.44)$$

$$B_\theta = E_r = E_\phi = 0, \quad (3.45)$$

M is equal to $k\mu/R_L$, with k a constant of the order of the unity. The plus and minus signs apply to the opposite hemispheres.

The electromagnetic energy flows with speed

$$\mathbf{v}_E = c \frac{\mathbf{E} \times \mathbf{B}}{B^2} \quad (3.46)$$

$$|\mathbf{v}_E| = c \frac{x}{\sqrt{1+x^2}}, \quad \gamma_E = \left[1 - \left(\frac{v_E}{c} \right)^2 \right] = (1+x^2)^{-\frac{1}{2}} \quad (3.47)$$

$$x = \frac{r \sin(\theta)}{R_L}. \quad (3.48)$$

Therefore the accelerated particles have speed $\mathbf{v} = \mathbf{v}_E + v_{\parallel} \mathbf{b}$, where \mathbf{b} is the verson of the magnetic field. If the initial particle energy inside the wind is $mc^2 \Gamma_L$, their parallel speed is

$$\beta_{\parallel} = \frac{\Gamma_L}{\Gamma_E \sqrt{\Gamma_L^2 + \Gamma_E^2}}, \quad (3.49)$$

and the wind Lorentz factor is

$$\Gamma_w = \frac{1}{\sqrt{1 - \beta_E^2 - \beta_{\parallel}^2}} = \sqrt{\Gamma_L^2 + \Gamma_E^2} = \sqrt{1 + \Gamma_L^2 + \left(\frac{r}{R_L} \right)^2 \sin^2(\theta)}. \quad (3.50)$$

A particle increases its energy by a factor for each decade in radius crossed. At large radii, the particles move with the field lines, with no motion parallel to \mathbf{B} , therefore we can focus on the speed component perpendicular to \mathbf{B}

$$\mathbf{v} = \mathbf{v}_{Er} + \frac{mc}{q} \frac{\mathbf{B} \times D(\gamma v)/Dt}{B^2} \approx \mathbf{v}_{Er} + \frac{mc}{q} \frac{\mathbf{B} \times D(\gamma_w \mathbf{v}_{Er})/Dt}{B^2} = \mathbf{v}_{Er} + \mathbf{v}_{pol}, \quad (3.51)$$

where $D/Dt = \partial/\partial t + \mathbf{v} \times \nabla \approx \partial/\partial t + v_{Er}(\partial/\partial r)$. We can evaluate the polarization speed \mathbf{v}_{pol} as

$$\mathbf{v}_{pol} = \mp \frac{mc^3}{q} \frac{r}{M} \hat{\theta}. \quad (3.52)$$

The evolution in time of the energy of each particle is

$$mc^2 \frac{D\Gamma}{Dt} = q \mathbf{v}_{pol} \cdot \mathbf{E}_{\theta} = \frac{mc^3 \sin(\theta)}{R_L}. \quad (3.53)$$

This model considers newly born, highly rotaring magnetar as UHECR sources, with an emission spectrum described by eq. (3.40). Furthermore, considering the relativistic force-free winds as linear accelerator, this model allows us to evaluate the particle speed and its evolution using eq. (3.53).

Chapter 4

Framework

After having explained the theoretical apparatus at the basis of this thesis, this chapter is dedicated to discuss the main goals of this work. This work can be divided in a first part of simulation and a second part of analysis. During the first part, we selected potential candidate magnetars inside of our Galaxy and simulated the emission of a fixed number of protons from them, at different energies. Then, in the second part, we compared the results obtained with Auger data to put upper limits on the number of particle emitted in several emission models. We also confronted the simulated particles with the Arons model [64] (described in section 3.5) and see if the experimental result are compatible within the model.

Following the structure of this work, this chapter is divided into two parts: a first part, where I discuss which and how the magnetars has been selected, and a second part, where I focus on the Auger data and the comparison with the simulated data.

4.1 Magnetars selection

Since cosmic rays are charged particles, they are deflected by the Galactic magnetic fields. This means that the UHECRs arriving to the Earth are delayed respect to the light coming from the same source. This allows us to put upper limits to the UHECR emission at birth of magnetars, even if they were born well before the cosmic rays were measured.

UHECRs are ultra-relativistic particles, their mass is several orders of magnitude lower than their momentum energy: the mass is of $O(10^9)$ eV while the momentum is higher than $O(10^{17})$ eV. UHECRs do not experience important energy losses during their propagation inside the Galaxy, so we can consider that they are travelling with a speed equal to the speed of light (c). Therefore, in order to understand the delay of cosmic rays respect to the light emitted by the magnetars, we have to count the length of the path that they have completed before they impact on the Earth, subtract the distance between the magnetar and the Earth (which is the length of the path made by the light), and then divide by c .

The strength of the Galactic magnetic field is of $\mathcal{O}(1)$ μG . The Milky Way can be approximated as a disk with a radius of 15 kpc and a height of 300 pc. The curvature radius for a proton of $E = 10^{18}$ eV is $\sim 10^{21}$ cm, which is approximately 300 pc,

name	d [kpc]	R.A.	Dec	τ_c [yr]	B_{surf} [PG]
Swift J1818.0-1607	4.8	274.63°	-16.13°	265 ± 1	0.3375 ± 0.0004
Swift J1818.0-1607	4.8	274.63°	-16.13°	491 ± 33	0.248 ± 0.008
SGR 1806-20	8.6	272.16°	-20.41°	242 ± 3	1.96 ± 0.01
PSR J1846-0258	6.0	281.60°	-2.98°	728 ± 1	0.049 ± 0.001
1E 1547.0-5408	4.5	237.73°	-54.31°	689 ± 6	0.318 ± 0.001

Table 4.1: Table resuming the main features of the magnetars selected for this analysis. The position of the magnetars is expressed in equatorial coordinates: right ascension (R.A.) and declination (Dec).

meaning UHECRs are not confined into the Galaxy. The curvature radius increases with the energy, so the more energetic a particle is, the less is deflected and the shorter is its path.

To be detected by Auger, UHECRs emitted by the magnetars need a good combination of delay and path length. The delay has to be inside the Auger lifetime window, but if the path length of the particles is too high the UHECRs that could be detected are too low in energy for Auger. Therefore not all magnetars in the Galaxy could be used in this work. The magnetars that could have led to Auger detecting UHECRs are the following ones:

- Swift J1818.0-1607;
- SGR 1806-20;
- PSR J1846-0258;
- 1E 1547.0-5408.

In table 4.1 the distance to Earth, the sky position, the characteristic age and the surface magnetic field of each magnetars are reported. Swift J1818.0-1607 is reported twice with two different characteristic ages, since two different measures has been completed and it is still under debate which is the correct one.

4.1.1 Swift J1818.0-1607

Swift J1818.0-1607 is a recently discovered magnetar (during March 2020). It is located at 18 h 18 m 3.7 s in right ascension and $-16^\circ 7' 31.8''$ in declination, and its distance to Earth is ~ 4.8 kpc.

Shortly after its discovery, the magnetar, whose features were compatible to the one of a soft gamma-ray repeater, has been monitored. The first measurements have been made using the 100 m Effelsberg radio telescope of the MPIfR (Max-Planck-Institut für Radioastronomie), leading to an estimated period of 1363.490 ± 0.003 ms, which is the second shortest among magnetars [65]. The first measure of the period time derivative has been $8.16 \pm 0.02 \times 10^{-11}$ ss $^{-1}$. With these two values we can estimate a characteristic age of 265 ± 1 yr, and a surface magnetic field of $B_{\text{surf}} =$

$3.375 \pm 0.004 \times 10^{14}$ G. However a second measure for a longer period of time made by three radio telescopes (the Effelsberg 100 m, the Lovell Telescope at Jodrell Bank Observatory and the Nançay Radio Telescope) estimated a different value in the period first derivative [66]. They observed how the spin rate can change by some order of values within weeks or days. Averaging the results obtained during the complete period the final value has been $\dot{P} = 4.4 \pm 0.4 \times 10^{-11}$ ss $^{-1}$. The new estimated values for characteristic age and surface magnetic field are $\tau_c = 491 \pm 33$ yr and $B_{\text{surf}} = 2.48 \pm 0.08 \times 10^{14}$ G.

Since it is still under debate which of these is the correct characteristic age, in this work the analysis have been completed for both the values.

4.1.2 SGR 1806-20

SGR 1806-20 is a magnetar whose distance to Earth is ~ 8.6 kpc, towards the constellation of the Sagittarius. It is located at 18 h 08 m 39.32 s in right ascension and $-20^\circ 24' 39.5''$ in declination. It has been recognised as a Soft Gamma Repeater and it is known to be the most magnetic object inside of our Galaxy, with a surface magnetic field of $\approx 2 \times 10^{15}$ G. Although being the farthest among the selected magnetars, this object can have emitted UHECRs compatible with Auger lifetime since it has a very low characteristic age. Its period, evaluated in 2007 [67], is $P = 7547.73 \pm 0.02$ ms, while the period first derivative is $\dot{P} = (49.5 \pm 0.5) \times 10^{-11}$ ss $^{-1}$. Using this data we obtain a characteristic age of $\tau_c = 242 \pm 3$ yr.

4.1.3 PSR J1846-0258

PSR J1846-0258 is a young X-Ray pulsar which displayed magnetar-like behaviour in 2006, with X-Ray burts, X-Ray flux increase and a sizable glitch with overshoot recovery. It has a distance from us of ~ 6.0 kpc and a surface magnetic field of $\approx 0.49 \times 10^{14}$ G, which is the less important among the considered objects. Its right ascension is 18 h 46 m 24.955 s while its declination is $-2^\circ 58' 30.069''$

This is most likely an object changing from its status of Rotational Power Pulsar to magnetar. It has been measured the post-glitch braking index of this object, using ν , $\dot{\nu}$ and $\ddot{\nu}$ (which are the rotational frequency and its first and second time derivative), finding $n = 2.16 \pm 0.13$ [68]. Using ν and $\dot{\nu}$, and therefore P and \dot{P} , we can also estimate the characteristic age. We have $P = 326.57128834(4)$ ms, $\dot{P} = 0.7107450(2) \times 10^{-11}$ ss $^{-1}$ and a characteristic age $\tau_c = 728$ yr with an associated error of less than a year. In this work however we considered an associated error of 1 yr.

4.1.4 1E 1547.0-5408

1E 1547.0-5408 is a magnetar with a surface magnetic field of $B_{\text{Surf}} \approx 3.2 \times 10^{14}$ G and a distance of ~ 4.5 kpc from us. It is located at 15 h 50 m 54.124 s in right ascension and $-54^\circ 18' 24.11''$ in declination. This magnetar had an outburst between October 2008 and December 2009, during which it has been monitored. At the end of the outburst, the values of period and period first derivative were studied obtaining

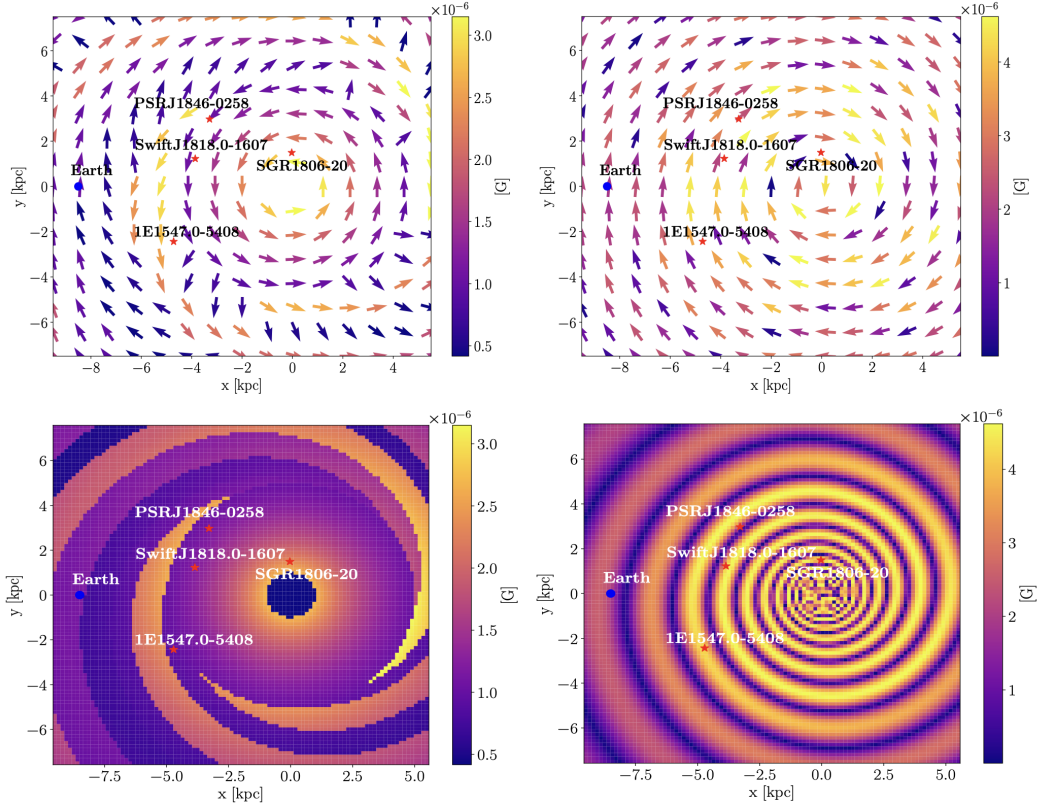


Figure 4.1: **Top:** The directions of the field line of the JF12 magnetic field (left) and PT11 magnetic field (right) with the associated field strength at the height of 0 pc towards the galactic plane. **Bottom:** The module of the JF12 magnetic field (left) and PT11 magnetic field (right) as a function of the coordinates of the galactic plane at the height of 0 pc. The red stars are the projection in the galactic plane of the position of the selected magnetars while the blue dot indicates the position of the Earth.

$P = 2072.1255 \pm 0.0001$ ms and $\dot{P} = 4.77 \pm 0.04$ ss $^{-1}$ [69]. We can derive the characteristic age of the magnetar which is $\tau_c = 689 \pm 6$ yr.

4.2 Simulation

After having selected the candidate magnetars, the next step has been studying the emission and propagation of UHECRs. The effect on the propagation of cosmic rays inside our Galaxy has been simulated using the *python* package CRPROPA [70], which is created to propagate particles in the Galaxy with a defined magnetic field.

The simulations have been performed inside a galactocentric frame system where the Galactic Centre is at $(x,y,z)=(0,0,0)$ while the Earth is at $(x,y,z)=(-8.5,0,0)$ kpc. The magnetars have been posed a source of cosmic rays passing from Equatorial coordinates to galactocentric coordinates using the *python* package ASTROPY.

The cosmic rays propagation has been completed considering a semi-ballistic regime. 10^9 particles at different energies were simulated and the chosen energies have been selected differently for each magnetar considering their distance to Earth and their age.

A strong assumption has been performed to simulate the Earth as observer: it has been depicted as a sphere with a radius of 10 pc, this has been the best compromise to permit that a significant number of particles could hit the target. As a consequence, in the following stages of the analysis, the exposure has been scaled, passing from the Earth of 10 pc radius to the real Auger exposure, and the 10 pc more the particles had to do to reach the real experiment (equal to ~ 32 yr in delay) have been added.

Cosmic rays have been emitted in random directions considering a cone of 1.2π , with the axis oriented along the line connecting the magnetar and the Earth. This aperture has been selected based on a preliminary work made with Swift J1818.0-1607: the value 1.2π has been selected because it allowed us to not loose information at any energy. This work has been repeated for all magnetars, to be sure that this value could be used for any of them.

During this work two models of magnetic field have been considered: the first one has been the Pshirkov-Tinyakov (PT11) [71], the second one has been the Janson-Farrar model (JF12) [72] (considered without any turbulent random component or striated random component). This work has been developed with two different models to see if there is an agreement among the ones considered. The features of the considered magnetic fields can be observed in fig. 4.1.

For all the propagation scenarios it has been considered a model in which there is only proton acceleration. The delay expected for heavier nuclei could be extrapolated starting from the proton one and scaling it proportionally. Furthermore, since the path lengths are of $\mathcal{O}(10)$ kpc, the difference in the interaction probability with the photon background should not affect the results.

The delay of a UHECR could be found as

$$D = \frac{L_{UHECR} - L_\gamma}{c}, \quad (4.1)$$

where L_{UHECR} is the path made by the cosmic ray, L_γ is the path made by the light (i.e. the distance Earth-magnetars) and c is the speed of light (the UHECRs has been considered as ultra-relativistic particles).

4.3 Analysis

In fig. 4.2 we present two plots reporting the arrival directions of the simulated protons hitting the Earth in the case of Swift J1818.0-1607, considered with $\tau_c = 265 \pm 1$ yr both for PT11 and JF12. We can see how the particles are concentrated in two different zones: in PT11 they come mainly from a region below the magnetar, while in JF12 they come from above. The two ones differ also in the value of the maximum angular distance between the farthest protons and the magnetar: in PT11 it is 15° , while in JF12 it is 11° . The two models predict two different deflections of the simulated particles, but in both cases the distance are not too large. In order to

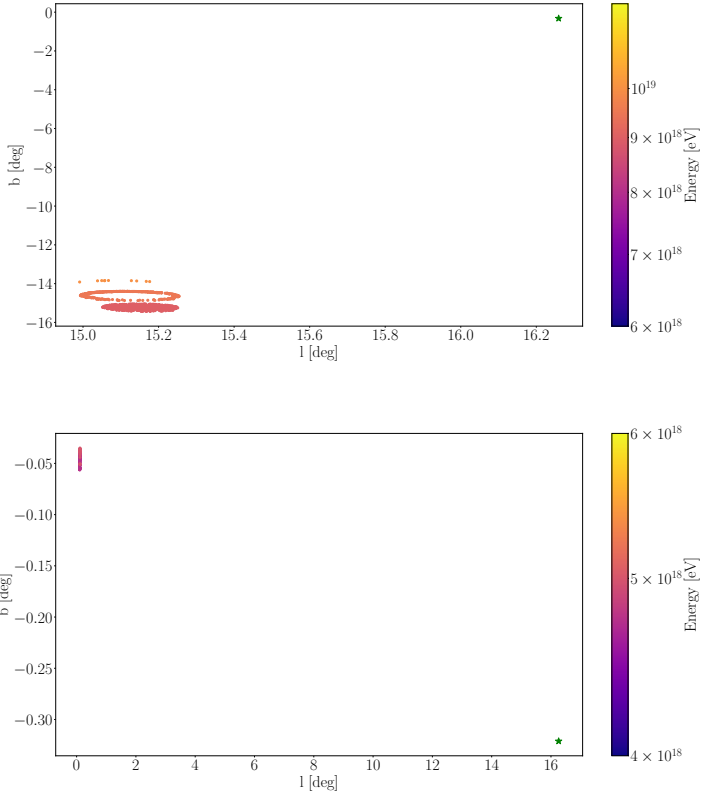


Figure 4.2: Arrival directions of the simulated particles hitting the Earth with an optimal delay expressed in Galactic coordinates in PT11 (top) and JF12 (bottom) in the case of Swift J1818.0-1607, considered with $\tau_c = 265 \pm 1$ yr. The green star expresses the position of the emitting magnetar

compare the simulated data with Auger data, we have defined an area centred around the position of the magnetar. This is a conservative approach (we could have selected a smaller area where the cosmic rays are coming from), and it has been dictated by the opposite results obtained with the two models of magnetic fields. Furthermore, we chose this method since the galactic magnetic fields are used without adding any random component (choice made for computational time reasons and since this component is overestimated in the two galactic magnetic field models adopted).

In fig. 4.3 the sky region considered in Auger data, are reported, both in the PT11 case and in the JF12 one. As it can be seen, some regions overlap, however they do not overlap in the energy bins.

The first step in this analysis has been finding the significance of the signal coming from the defined sky regions. In doing this we adopted the Li-Ma significance [73], which is defined as

$$S = \pm\sqrt{2} \times \sqrt{N_{\text{on}} \ln\left(\frac{1 + \alpha}{\alpha} \frac{N_{\text{on}} + N_{\text{off}}}{N_{\text{on}}}\right) + N_{\text{off}} \ln\left(\frac{1}{1 + \alpha} \frac{N_{\text{on}} + N_{\text{off}}}{N_{\text{off}}}\right)}. \quad (4.2)$$

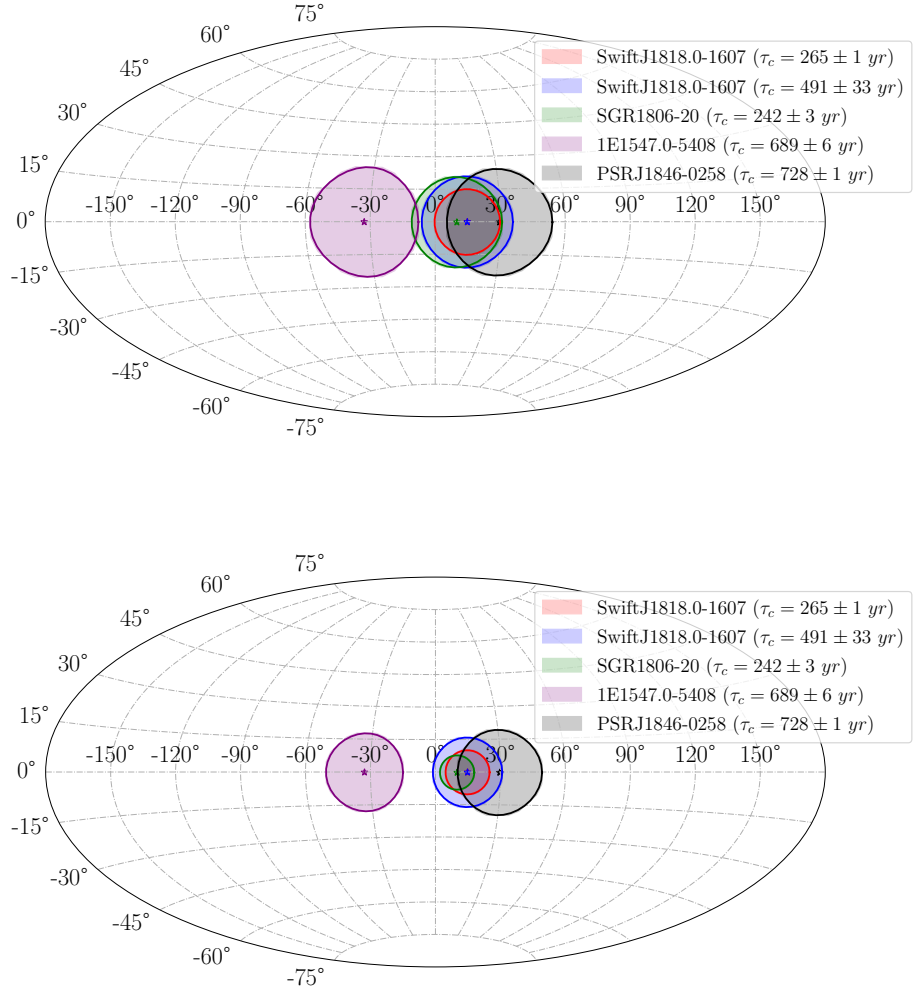


Figure 4.3: Sky positions of the selected magnetars in galactic coordinates with their corresponding regions defined to find the signal upper limits in Auger data in the PT11 case (top) and in the JF12 case (bottom)

N_{on} is the number of counts in the signal region, N_{off} is the number of counts in a selected background region and α is the ratio of the signal region time of exposure and the background region time of exposure. In eq. (4.2), S is in unit of gaussian standard deviations and it is positive if $N_{\text{on}} > N_{\text{off}}$ while it is negative if $N_{\text{on}} < N_{\text{off}}$.

In this analysis N_{on} is the number of counts collected by Auger coming from the defined sky region in the energy range that could have lead to the observation of the cosmic rays coming from the magnetar. To obtain N_{off} , 1000 datasets were simulated with a scrambling procedure. The scrambling procedure was carried out using Auger datasets in the desired energy range. The events were generated choosing a UTC time randomly between the ones from the original data, choosing a zenith angle in

Li-Ma significance			
name	τ_c [yr]	PT11	JF12
Swift J1818.0-1607	265 ± 1	0.73	-0.49
Swift J1818.0-160	491 ± 33	0.73	-0.10
SGR 1806-20	242 ± 3	1.21	0.81
PSR J1846-0258	728 ± 1	-0.98	-0.86
1E 1547.0-5408	689 ± 6	0.91	0.04

Table 4.2: Table reporting the Li-Ma significance for each magnetar, in unit of gaussian standard deviations, both for the PT11 and the JF12

the same way, while the azimuth angle was chosen randomly between 0° and 360° . To confront these results with data the Auger events has been divide in energy bins, where each bin has been centered on the energy of a simulation. N_{off} was evaluated taking the average values between all the generated events in the selected regions around magnetars in each energy bin and adding them up. α is equal to 1.

The significances for each magnetar are reported in table 4.2, both for PT11 and JF12. As it can be seen, no significant signal region have been found, therefore the second step of this analysis has been to put upper limits on the UHECR emission from the selected magnetars. In doing this a frequentist approach has been chosen, using Zech procedure [74]. Considering an experiment with an expected signal s and an expected background b , we can express the probability ϵ to find N or less counts as

$$\epsilon = \frac{\sum_{n=0}^N \mathcal{P}(n; s+b)}{\sum_{nb=0}^N \mathcal{P}(nb; b)}, \quad (4.3)$$

where \mathcal{P} expresses a Poissonian distribution. We consider that, if we know the expected value of background counts b , we can chose a Confidence Level (CL) $CL = 1 - \epsilon$ and invert the previous equation to find the expected value for signal counts s , i.e. the upper limit of the counting experiment.

In this analysis N represents the number of particles obtained from Auger data, while b the isotropic background that we expect at the observatory, obtained taking the average value of the scrambled datasets in the selected region.

The analysis has been divided in two parts: in the first part the results of the simulations were compared to Auger data to test Arons model and in the second part a set of different emission models was proposed to find the maximum number of particles accelerated by the magnetars in these models.

4.3.1 Analysis on Arons model

In Arons model the emission spectrum of a magnetar accelerating UHECRs is

$$\frac{dN_i}{dE} = \frac{9}{4} \frac{c^2 I}{Ze\mu E} \left(1 + \frac{\Gamma}{\Gamma_g}\right)^{-1} = A \frac{1}{E} \frac{E_g}{E_g + E}, \quad \text{with} \quad (4.4)$$

$$\Gamma_g = \frac{Z\eta e\mu}{m_i c^4} \Omega_g^2 = \frac{5}{72} \frac{Z\eta e\mu^3}{G I^2 \epsilon^2 m_i c^2}. \quad (4.5)$$

In this model, the particles are emitted instantaneously by the magnetar. The previous equation represents the UHECR emission spectrum, therefore we can integrate it to find the number of particles emitted between two energies E_i and E_j .

$$N(E_i, E_j) = \frac{9}{4} \frac{c^2 I}{Z e \mu} \times \ln \left(\frac{E_j}{E_i} \frac{E_g + E_i}{E_g + E_j} \right). \quad (4.6)$$

To compare the simulation data with Auger data, we need to estimate the simulation exposure and then scale it to the Auger exposure. In the simulations the observer is a spherical object, with radius of 10 pc, with a field of view pointing toward all directions and a lifetime equal to the Auger lifetime (the timespread for Auger in this analysis goes from 2004 to 2018). Therefore the simulation exposure is:

$$X_{\text{Sim}} = 4\pi(10)^2 \times 4\pi \times 14 \text{ pc}^2 \text{ sr yr}. \quad (4.7)$$

On the other hand, the Auger exposure (X_{Auger}) has been obtained considering all the active area, during the observatory lifetime, which pointed toward the selected region around the magnetar.

In the simulations the emission zone was limited to a cone with 1.2π of aperture, however the real magnetar should in principle emit in all the direction. Therefore, in order to obtain the number of particles arriving to the Earth per particle emitted by the magnetar we need to divide the results of the simulations for $W = 10^9 \times 4\pi/1.2\pi = 3.3 \times 10^9$. Then dividing by X_{sim} and multiplying for X_{Auger} , it has been possible to obtain the fraction of protons which could be detected by the observatory.

The signal expected at the observatory for each energy bin considered is:

$$s(E_{\text{mid}}) = N(E_i, E_j) \frac{N_{\text{sim}}(E_{\text{mid}})}{W} \frac{X_{\text{Auger}}}{X_{\text{sim}}}. \quad (4.8)$$

E_{mid} is the central energy of the energy bin considered, while E_i and E_j are respectively the minimum and the maximum value. $s(E_{\text{mid}})$ is the upper limit obtained with Auger data. We can now invert the last equation to write

$$N(E_1, E_2) = \frac{s(E_{\text{mid}})}{N_{\text{sim}}(E_{\text{mid}})} \frac{W \times X_{\text{Auger}}}{X_{\text{sim}}}, \quad (4.9)$$

and we can confront this value with the one predicted in Arons model.

4.3.2 Analysis on multiple emission models

Besides comparing Arons model, in the second part of the analysis we have defined other emission models by combining a power law in energy (with spectral index γ) with three different models in time. The three emissions model are: an instantaneous emission model, a constant emission model acting for a limited time period (with time period T) and an emission model softening as a decay law (with decay constant τ). We can write the differential spectrum in energy (dN/dE) for the three models

leaving N_0 as a free parameter, which is the total number of particles emitted by the magnetar. During the analyses we have considered different combination of γ with T and τ .

$$\frac{dN}{dE} = N_0 \times f(E, \gamma) = N_0 \times (\gamma - 1) \frac{E^{-\gamma}}{E_0^{-\gamma+1}}, \quad (4.10)$$

$$\frac{dN}{dEdt} = \begin{cases} N_0 \times g(t, T) \times f(E, \gamma) = N_0 \times \frac{1}{T} \times (\gamma - 1) \frac{E^{-\gamma}}{E_0^{-\gamma+1}} & 0 < t < T \\ 0 & otherwise \end{cases}, \quad (4.11)$$

$$\frac{dN}{dEdt} = N_0 \times h(t, \tau) \times f(E, \gamma) = N_0 \times \frac{e^{-\frac{t}{\tau}}}{\tau} \times (\gamma - 1) \frac{E^{-\gamma}}{E_0^{-\gamma+1}}. \quad (4.12)$$

E_0 is a reference value chosen to normalize the number of emitted particles to N_0 , and it is equal to 1 EeV, while N_0 is free parameter in this analysis.

Considering the instantaneous emission model we can integrate eq. (4.10) and find the number of particles emitted between E_i and E_j . Then, considering again the exposure of the simulated events and the exposure of Auger, we can write

$$s(E_{\text{mid}}) = N_0(E_{\text{mid}}) F(E_i, E_j) \frac{N_{\text{sim}}(E_{\text{mid}})}{W} \frac{X_{\text{Auger}}}{X_{\text{Sim}}}, \quad (4.13)$$

where $F(E_i, E_j)$ is the integral of the function $f(E, \gamma)$ in eq. (4.10) evaluated between E_i and E_j . $s(E_{\text{mid}})$ is the upper limit obtained with the scrambling procedure. Inverting the last equation we can find the value N_0 .

We can now proceed with the last two emission models. In case of constant emission, the equation expressing the signal expected at the observatory for each energy bin is:

$$s(E_{\text{mid}}, T) = N_0(E_{\text{mid}}) F(E_i, E_j) \frac{1}{W} \frac{X_{\text{Auger}}}{X_{\text{sim}}} \int_0^T g(t, T) N_{\text{sim}}(E_{\text{mid}}, T) dt. \quad (4.14)$$

In this case, we have to consider that in expanding the time period in emission, we are also expanding the optimal delay. After having selected γ and T , it has been divided the integral in eq. (4.14) in several time bins (going from 0 to T), so it has been possible to understand which is the number of protons arriving at the Earth in the simulations. In this way, we could evaluate the free parameter N_0 in multiple combinations of γ and T .

Applying the exact same method, we have been able to consider the third case, the one with a decay law in time. We began by defining an energy constant γ and a time constant τ , so we could integrate eq. (4.12) to get the following equation, which expresses the signal at the observatory for each energy bin:

$$s(E_{\text{mid}}, \tau) = N_0(E_{\text{mid}}) F(E_1, E_2) \frac{1}{W} \frac{X_{\text{Auger}}}{X_{\text{sim}}} \int_0^{3\tau} h(t, \tau) N_{\text{sim}}(E_{\text{mid}}, \tau) dt. \quad (4.15)$$

With the same procedure defined for the previous case we have been able to get N_0 . The only differences from the previous case are having defined temporal bin between 0 and 3τ and integrated the function $h(t, \tau)$ written in eq. (4.12).

Chapter 5

Results

With this chapter I present the results of the analysis. I focus first on the Arons model, comparing the factor predicted and the one obtained with the simulations. Then I study the other emission models proposed in the previous chapter. I start presenting the detailed results obtained for a single magnetar, and then I make a comparison of the upper limits obtained for all the selected magnetars.

All the results are obtained using Auger open data, which represent 10% of the data gathered by the observatory from 2004 to 2018. Since we look for upper limits in signal in defined zones of the sky, we expect that the results found with the open data are compatible with the one that would have been found with the total data. However, it is likely that using the complete data the errors associated to the analyses would be smaller.

5.1 Arons model

To compare Arons model with the results of simulations we have to find the number of particles emitted by both models. The number of particles predicted by Arons between E_i and E_j is

$$N(E_i, E_j) = \frac{9}{4} \frac{c^2 I}{Z e \mu} \times \ln\left(\frac{E_j E_g + E_i}{E_i E_g + E_j}\right). \quad (5.1)$$

Considering that the previous equation is expressed in cgs and that the inertial moment of a sphere is $I = 2/5 M R^2$ we can rewrite eq. (5.1) as

$$N(E_i, E_j) = \frac{1.125 \times 10^{43}}{Z} \left(\frac{B}{10^{15} \text{ G}}\right)^{-1} \left(\frac{R}{10 \text{ km}}\right)^{-1} \left(\frac{M}{M_\odot}\right) \times \ln\left(\frac{E_j E_g + E_i}{E_i E_g + E_j}\right), \quad (5.2)$$

where E_g is

$$E_g = 0.25872 \times 10^2 Z \left(\frac{\eta}{0.1}\right) \left(\frac{B}{10^{15} \text{ G}}\right)^3 \left(\frac{R}{10 \text{ km}}\right)^2 \left(\frac{M}{M_\odot}\right)^{-2} \left(\frac{\epsilon}{0.01}\right)^{-2} \text{ EeV}. \quad (5.3)$$

In Arons model we have several free parameters that we can not compute. η expresses the efficiency of the accelerating process, B is the magnetic field of the magnetar,

R is the radius, M is its mass and ϵ is a parameter expressing the ellipticity of the magnetar. Since we consider that the emission can happen in the first life stages of the magnetar we have to consider the magnetic field at birth, however since we do not know the value at birth the current estimation has been used as a conservative benchmark. We do not know also the radius and the mass of the magnetar, therefore in this work we chose to use as standard value for all magnetars $R = 10$ km and $M = 1.4 M_\odot$. The last two free parameters are ϵ and η , which have been chosen according to Arons predictions: $\epsilon = 0.01$ and $\eta = 0.1$.

To compare Arons model with simulations, we supposed the following emission model

$$\tilde{f}(E) = \frac{A}{E} \left(1 + \frac{E}{E_g}\right)^{-1}, \quad (5.4)$$

where A is a factor that, if the Arons model is valid for the selected magnetars, should be equal to the one predicted, which is

$$A_{\text{Arons}} = \frac{1.125 \times 10^{43}}{Z} \left(\frac{B}{10^{15} \text{ G}}\right)^{-1} \left(\frac{R}{10 \text{ km}}\right)^{-1} \left(\frac{M}{M_\odot}\right). \quad (5.5)$$

We understand now that we can find the factor A from the simulations and confront it with the one predicted. Considering the simulations we can write

$$\begin{aligned} s(E_{\text{mid}}) &= \tilde{F}(E_i, E_j) \frac{N_{\text{sim}}(E_{\text{mid}})}{W} \frac{X_{\text{Auger}}}{X_{\text{sim}}} = \\ &= \frac{N_{\text{sim}}(E_{\text{mid}})}{W} \frac{X_{\text{Auger}}}{X_{\text{sim}}} A(E_{\text{mid}}) \times \ln\left(\frac{E_j E_g + E_i}{E_i E_g + E_j}\right), \end{aligned} \quad (5.6)$$

where $\tilde{F}(E_i, E_j)$ is the function in eq. (5.4) integrated between E_i and E_j . We can now invert eq. (5.6) to obtain $A(E_{\text{mid}})$

$$A(E_{\text{mid}}) = W \times \frac{s(E_{\text{mid}})}{N_{\text{sim}}(E_{\text{mid}})} \frac{X_{\text{sim}}}{X_{\text{Auger}}} \times \left[\ln\left(\frac{E_j E_g + E_i}{E_i E_g + E_j}\right)\right]^{-1}. \quad (5.7)$$

We repeated this procedure for each simulated energy and select the factor A as the smallest among the one measured.

In tables 5.1 and 5.2 the results of the value A obtained from Arons model and from simulations, are reported respectively with cosmic ray propagation in PT11 and in JF12.

As can be seen by the tables, the values obtained from Arons model and from simulations are incompatible with each other, both using PT11 and JF12. The two results differ of several order of magnitude: from $\mathcal{O}(10^3)$, in the case of PSR J1846-0258, to $\mathcal{O}(10^6)$ for 1E 1547.0-5408. We also see that the results using PT11 differ from the ones obtained with JF12 (we obtain always a minor number using PT11), but they remain in the same order of magnitude. The error reported in the simulation results are the one associated with the characteristic age of the magnetar. Since a change in the age of a magnetar impose also a change in the energy of the particle arriving at the Earth with an optimal delay, the error associated to the number of particles emitted are not obtained considering the extremes of the magnetar age. To compute the errors we defined the following steps:

PT11				
name	age [yr]	B [PG]	Arons	Auger
Swift J1818.0-1607	265 ± 1	0.3375 ± 0.0004	4.67×10^{43}	$9.17_{-0.46}^{+0.65} \times 10^{37}$
Swift J1818.0-1607	491 ± 33	0.248 ± 0.008	6.35×10^{43}	$1.6_{-0.8}^{+2.4} \times 10^{38}$
SGR 1806-20	242 ± 3	1.96 ± 0.01	7.88×10^{42}	$4.60_{-0.74}^{+0.43} \times 10^{36}$
PSR J1846-0258	728 ± 1	0.049 ± 0.001	3.21×10^{44}	$1.20_{-0.18}^{+0.18} \times 10^{41}$
1E 1547.0-5408	689 ± 6	0.318 ± 1	7.85×10^{44}	$4.60_{-0.74}^{+0.43} \times 10^{38}$

Table 5.1: Results on the number of particle emitted by magnetars according to the Arons model and to the Auger data in PT11

JF12				
name	age [yr]	B [PG]	Arons	Auger
Swift J1818.0-1607	265 ± 1	0.3375 ± 0.0004	4.67×10^{43}	$2.34_{-0.20}^{+0.11} \times 10^{38}$
Swift J1818.0-1607	491 ± 33	0.248 ± 0.008	6.35×10^{43}	$7.8_{-3.6}^{+9.4} \times 10^{38}$
SGR 1806-20	242 ± 3	1.96 ± 0.01	7.88×10^{42}	$6.4_{-1.0}^{1.8} \times 10^{37}$
PSR J1846-0258	728 ± 1	0.049 ± 0.001	3.21×10^{44}	$2.67_{-0.19}^{+0.37} \times 10^{41}$
1E 1547.0-5408	689 ± 6	0.318 ± 1	7.85×10^{44}	$1.99_{-0.48}^{+0.73} \times 10^{38}$

Table 5.2: Results on the number of particle emitted by magnetars according to the Arons model and to the Auger data in JF12

- (i) the age interval defined by the errors in the characteristic age was divided in 10 bins;
- (ii) the analysis on the upper limits was completed for each age at the edge of the defined bins;
- (iii) we selected the largest value and the smallest value obtained;
- (iv) the errors associated to the age are deduced subtracting the value for the characteristic age to the largest value, and subtracting the smallest value to the one with the characteristic age.

From the results, it is evident that a symmetric error in the age does not correspond to a symmetric error in the number of particles.

5.2 Swift J1818.0-1607 ($\tau_c = 265 \pm 1$ yr)

In this section I present the results obtained with Swift J1818.0-1607 in the case of characteristic of 265 ± 1 yr.

In Fig. (5.1) two scatter plots showing the delay of the particles emitted hitting the Earth are reported. The gray band depicts the optimal delay that protons

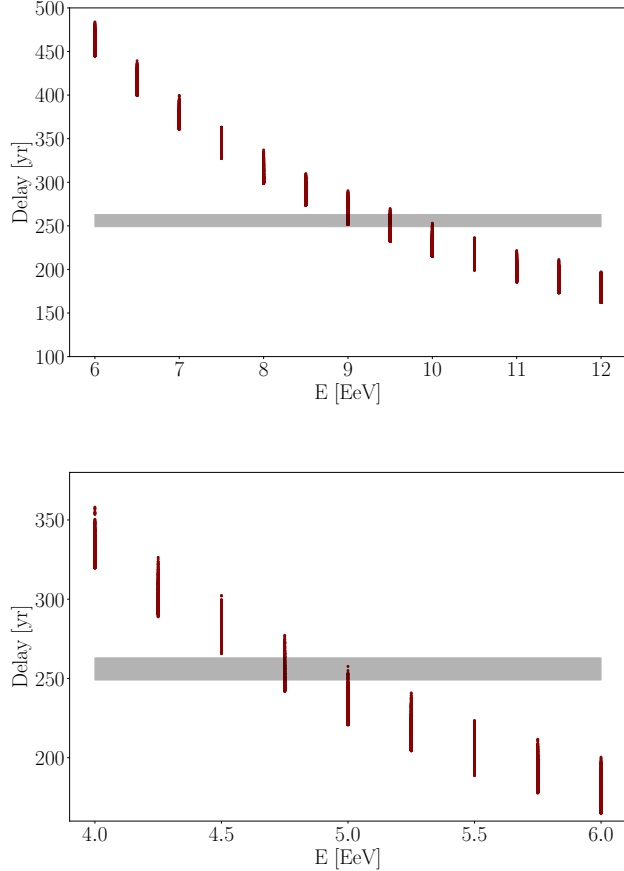


Figure 5.1: Plots reporting the delays obtained for the simulated particles in PT11 (top) and JF12 (bottom), expressed as red dots, and the optimal delay for the protons to be detected by Auger, expressed as a grey band, considering an instantaneous emission at birth

should have in order to be detected by Auger (in the case of instantaneous emission at birth by the magnetar). This is obtained considering the characteristic age of the magnetar, the year in which it has been measured and the Auger lifetime. In this case the magnetar age has been estimated in the 2020 and it is equal to 265 yr, therefore, considering that the Auger data has been collected between 2004 and 2018, we have that the optimal delay is comprised between $265 - 16 \text{ yr} = 249 \text{ yr}$ and $265 - 2 \text{ yr} = 263 \text{ yr}$. The top plot reports the results obtained using PT11 as galactic magnetic field, while the bottom plot using JF12 as galactic magnetic field. As we can see the two differ in the optimal energy of the protons hitting the Earth: for PT11 this is comprised between 9 and 10 EeV, while for JF12 it is between 4.75 and 5 EeV. This means that the protons are more deflected by PT11 than by JF12.

As said in the previous chapter, we considered the arrival directions of the protons hitting the Earth and evaluated the maximal distance between them and the position

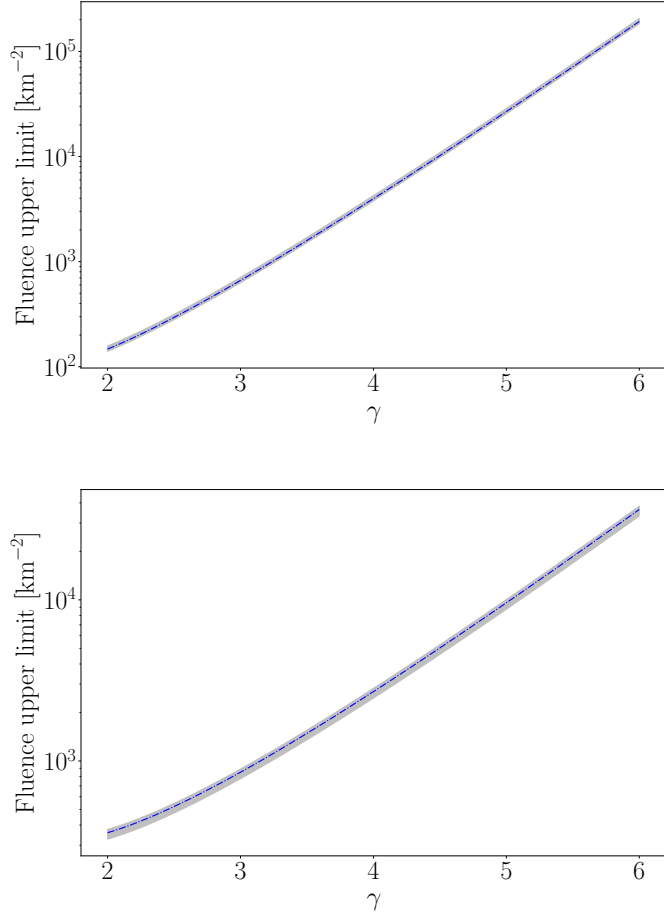


Figure 5.2: Fluence upper limit obtained for Swift J1818.0-1607 in the case of an instantaneous emission described by eq. (4.10) for PT11 (top) and JF12 (bottom)

in the sky of the magnetar, both for PT11 and JF12. From these two distances we defined two circular regions centred in the magnetar position and with radii equal to the distances. These are the regions of the Auger data in which we looked for upper limits. Furthermore, these two distances will be the radii of the areas not only in the instantaneous emission case but also in the time dependent emission cases. In fact, if the magnetar emits in time, the protons emitted after its birth will need less delay to hit the Earth during Auger lifetime, consequentially these particles will be more energetic and less deflected. The maximum distance obtained in the case of instantaneous emission will be the same for all the emission scenarios.

After having found the right delays and the right distances, we can move on to confront the various emission scenarios, starting with the instantaneous emission at birth, described by eq. (4.10). In this model we have only a free parameter which is the spectral index γ . Rather than finding the number of particles emitted in function of γ , it is more physically interesting to study the fluence at 5 kpc. This is

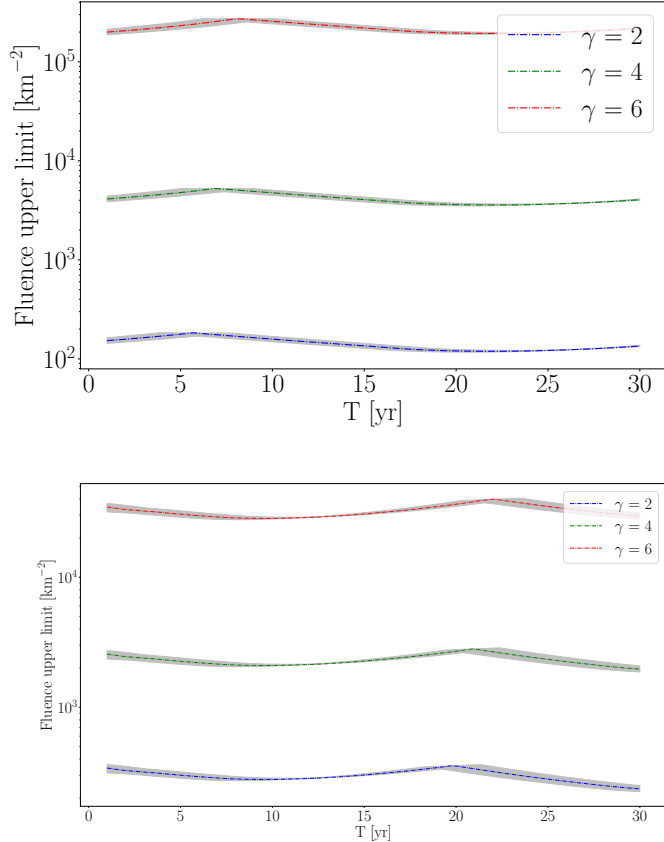


Figure 5.3: Same as fig. 5.2 but for the emission model continuous in time expressed by eq. (4.11)

the number of particles emitted that flow at a distance of 5 kpc. The value has been chosen as a reference distance of our Galaxy: this should be the fluence recorded at the Earth if all the particles emitted could be detected. The fluence is defined as $F = N_0 / 4\pi(5 \text{ kpc})^2$.

To find N_0 we have to invert eq. (4.13) as follows

$$N_0(E_{\text{mid}}) = \frac{s(E_{\text{mid}})}{F(E_i, E_j)} \frac{W}{N_{\text{sim}}(E_{\text{mid}})} \frac{X_{\text{sim}}}{X_{\text{Auger}}} . \quad (5.8)$$

In this way we found the value of N_0 for all the simulated energy of the protons reaching the Earth. The final value has been chosen as the smallest among the one found.

The results for the instantaneous emission scenario are reported in fig. 5.2: in the top plot we find the results for the PT11 magnetic field, while in the bottom plot we find the results for JF12. Although in both plots we can find the same trend, since the fluence upper limit increases with the spectral index, the PT11 case has a more important growth than the JF12 one, passing from $\mathcal{O}(10^2) \text{ km}^{-2}$ to $\mathcal{O}(10^5) \text{ km}^{-2}$.

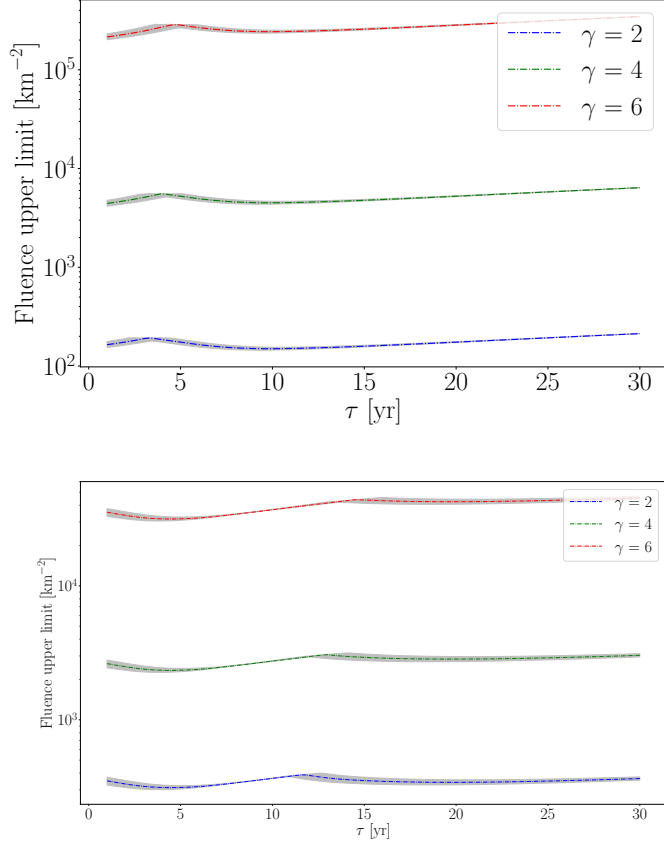


Figure 5.4: Same as fig. 5.2 but for the emission model with a decay law in time expressed by eq. (4.12)

We can now confront also the emission scenario constant in time and the one described by a decay law. In both cases, described respectively by eq. (4.11) and eq. (4.12), we have two free parameters: the spectral index γ and a time parameter, which is the time-period of emission T in the first scenario, and the decay constant τ in the second one. Therefore we chose to consider the fluence of the two models fixing γ , and going to study it as a function of the time parameter. We considered three possible spectral indexes $\gamma = 2, 4, 6$, while both the T and τ span between 1 and 30 yr.

The values of N_0 in these two scenarios are obtained inverting eq. (4.14) (for the continuous model)

$$N_0(E_{\text{mid}}, T) = W \times \frac{s(E_{\text{mid}}, T)}{F(E_i, E_j)} \frac{X_{\text{sim}}}{X_{\text{Auger}}} \times \left[\int_0^T g(t, T) N_{\text{sim}}(E_{\text{mid}}, T) dt \right]^{-1}, \quad (5.9)$$

and eq. (4.15) (for the decay model)

$$N_0(E_{\text{mid}}, \tau) = W \times \frac{s(E_{\text{mid}}, \tau)}{F(E_i, E_j)} \frac{X_{\text{sim}}}{X_{\text{Auger}}} \times \left[\int_0^{3\tau} g(t, \tau) N_{\text{sim}}(E_{\text{mid}}, \tau) dt \right]^{-1}. \quad (5.10)$$

In both cases the final value of N_0 is chosen as the smallest among the ones obtained.

The results for both the scenarios are reported in fig. 5.3 and fig. 5.4, where the top plots are the PT11 cases and the bottom plots are the JF12 ones. In both figure we can see the same trends: the fluence upper limit remains almost constant in function of the time parameters while increases of several orders for different γ . In both the scenarios the PT11 magnetic field predicts a bigger fluence than the JF12.

5.3 Complete results

As made in the previous section with Swift J1818.0-1607 in the case of $\tau_c = 265 \pm 1$ yr, in this section we consider the results obtained for all magnetars. In the following pages I show the plot for the fluence upper limit in all the emission scenarios, both for PT11 and JF12. Apart from the fluence upper limit plots I also show the plots reporting the upper limit on the integrated luminosity of the model. The luminosity is defined as

$$\mathcal{L} = \int_{E_0}^{\infty} E \frac{dN}{dE}(E) dE, \quad (5.11)$$

which represents the total energy emitted in protons by the magnetar. In case of the time-dependent emission models the previous equation is modified in

$$\mathcal{L} = \int_{E_0}^{\infty} \int_0^{\infty} E \frac{dN}{dE}(E, t) dEdt. \quad (5.12)$$

Observing the following plots we can find some common trends. We see that the fluence upper limit increases with γ both in PT11 and JF12, and that is valid for all the emission model.

Confronting the singular magnetars we can see that, apart from low γ in PT11, the most interesting one is SGR 1806-20. The fluence upper limit is some order of magnitude bigger than the other ones, and this behaviour is more evident with high γ and with JF12. This trend is also visible in the luminosity upper limit plot where the energy needed in the various model increases with γ . It is interesting to find that the most promising magnetar to accelerate UHECRs is SGR 1806-20, which is the most intense in magnetic field and the youngest one.

It is also interesting to observe that for SGR 1806-20 for $\gamma = 6$ the luminosity upper limit is of $\mathcal{O}(10^{49})$ erg in PT11 and $\mathcal{O}(10^{50})$ erg in JF12. These are energies intense, corresponding to the rotational energy of a magnetar of $M = 1.4 M_{\odot}$, $R = 10$ km and period of $\mathcal{O}(10)$ ms, or to one thousandth of the energy of a core collapse supernova. However, we have to note that an emission scenario with $\gamma = 6$ is unlikely to reproduce correctly the behaviour of the observed cosmic rays flux at the Earth. Therefore, even if from these results the fluence upper limit increases with γ , we have also to consider that model with high spectral index are not physically realistic.

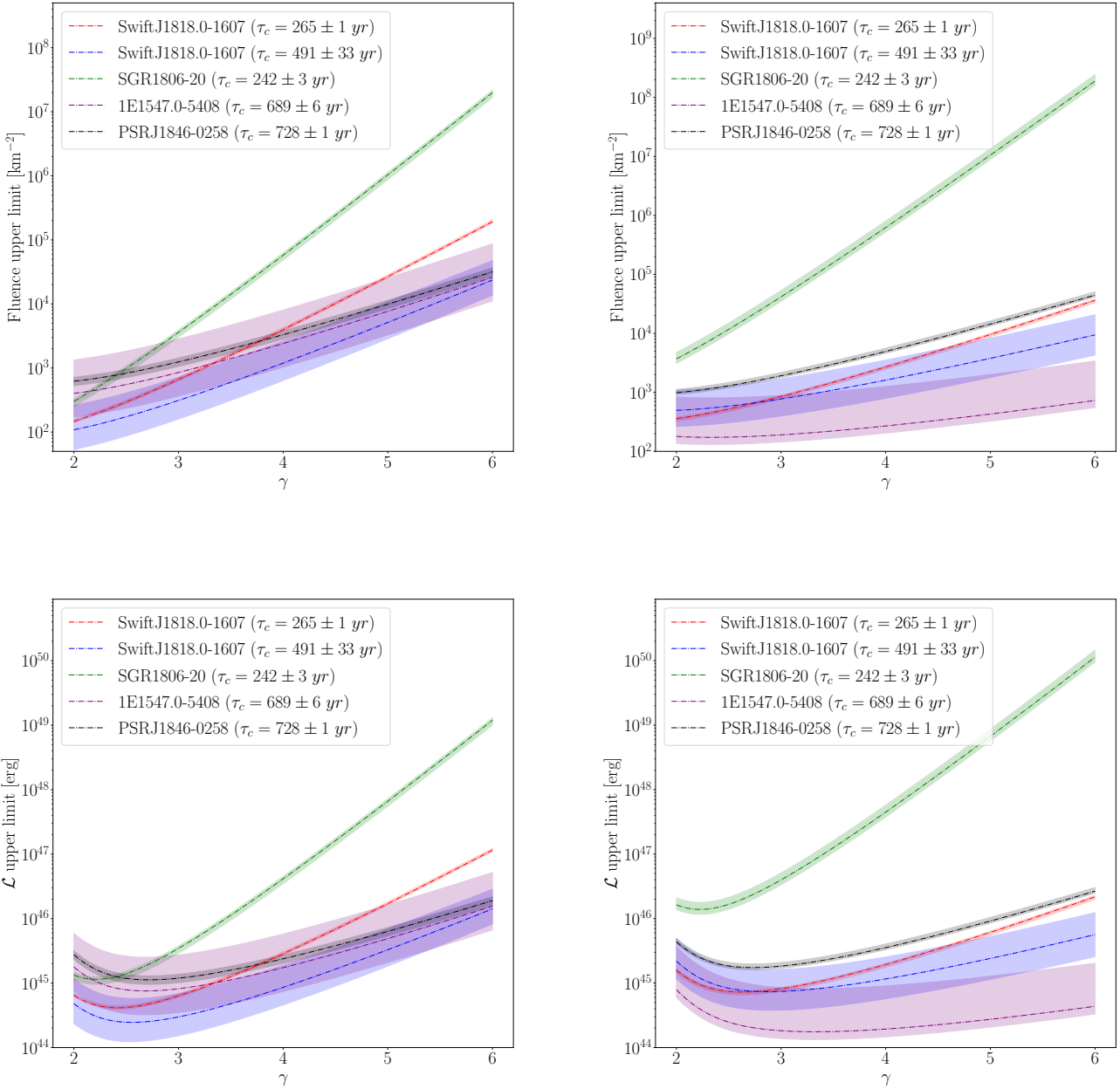


Figure 5.5: **Top:** Fluence upper limit plots of all magnetars in the constant emission scenario, defined by eq. (4.10), reported both for PT11 (left) and JF12 (right).
Bottom: The associated luminosity upper limit plots.

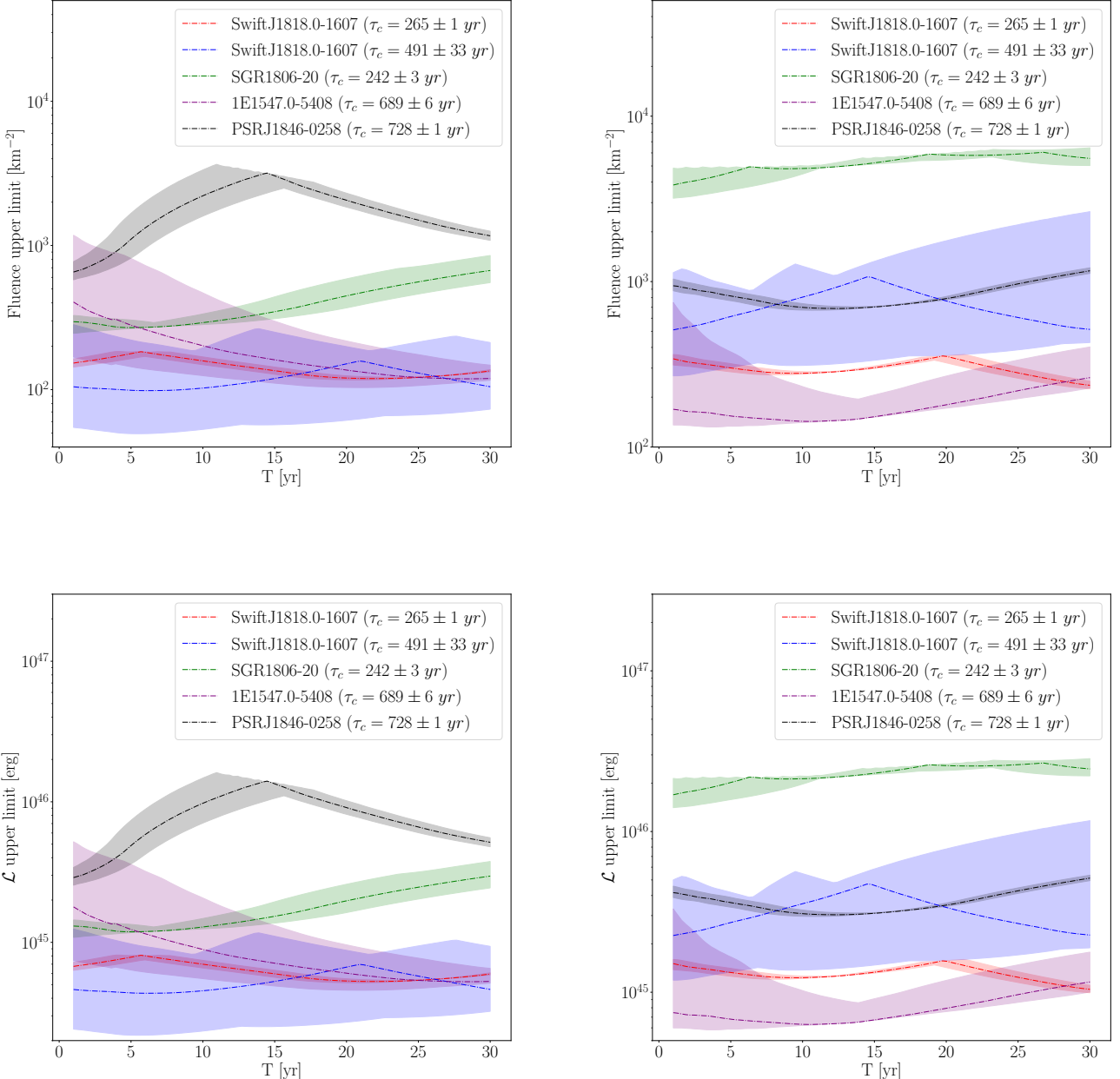


Figure 5.6: Same as fig. 5.5 but in the continuous emission scenario expressed by eq. (4.11) with $\gamma = 2$

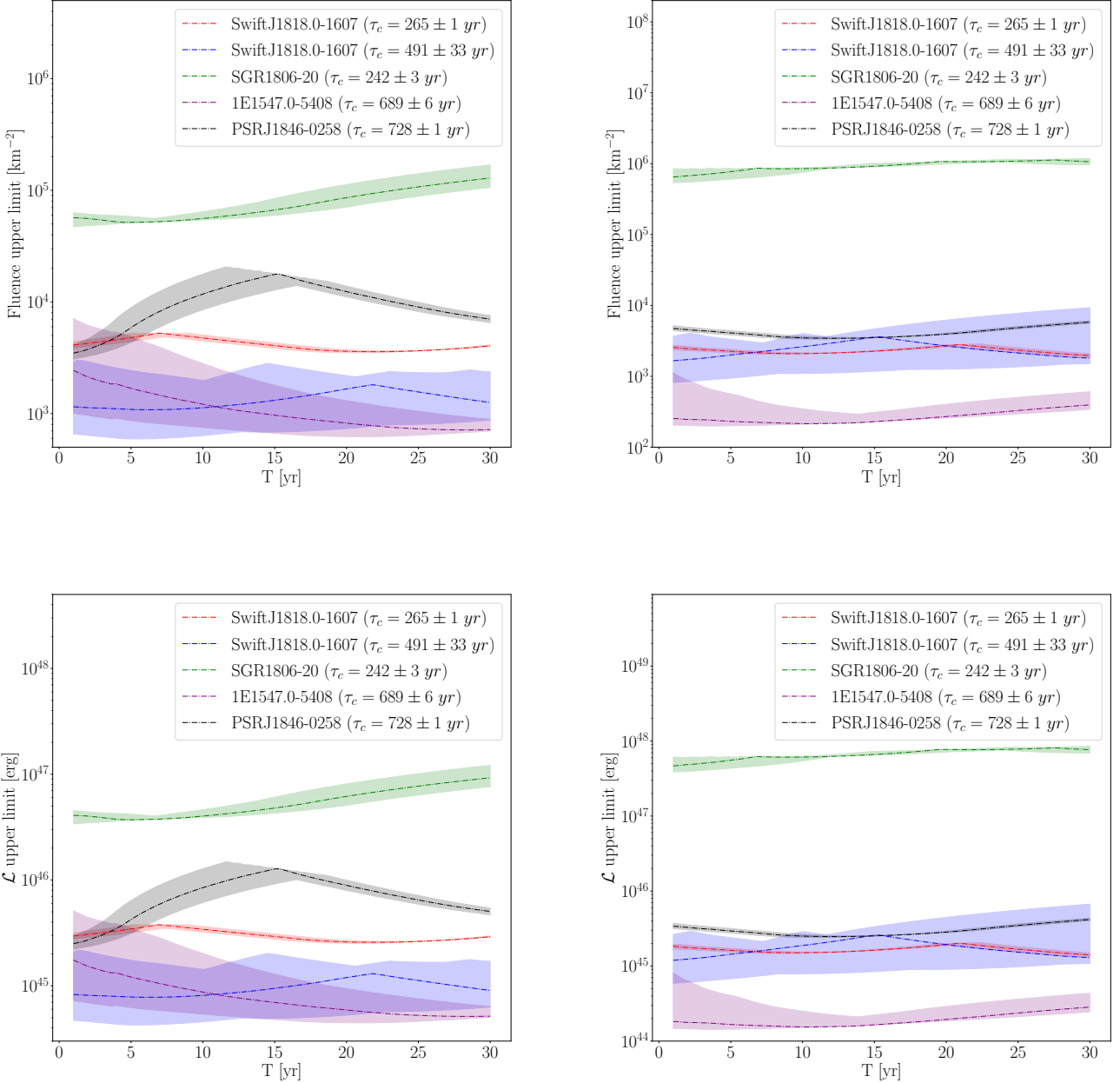


Figure 5.7: Same as fig. 5.5 but in the continuous emission scenario expressed by eq. (4.11) with $\gamma = 4$

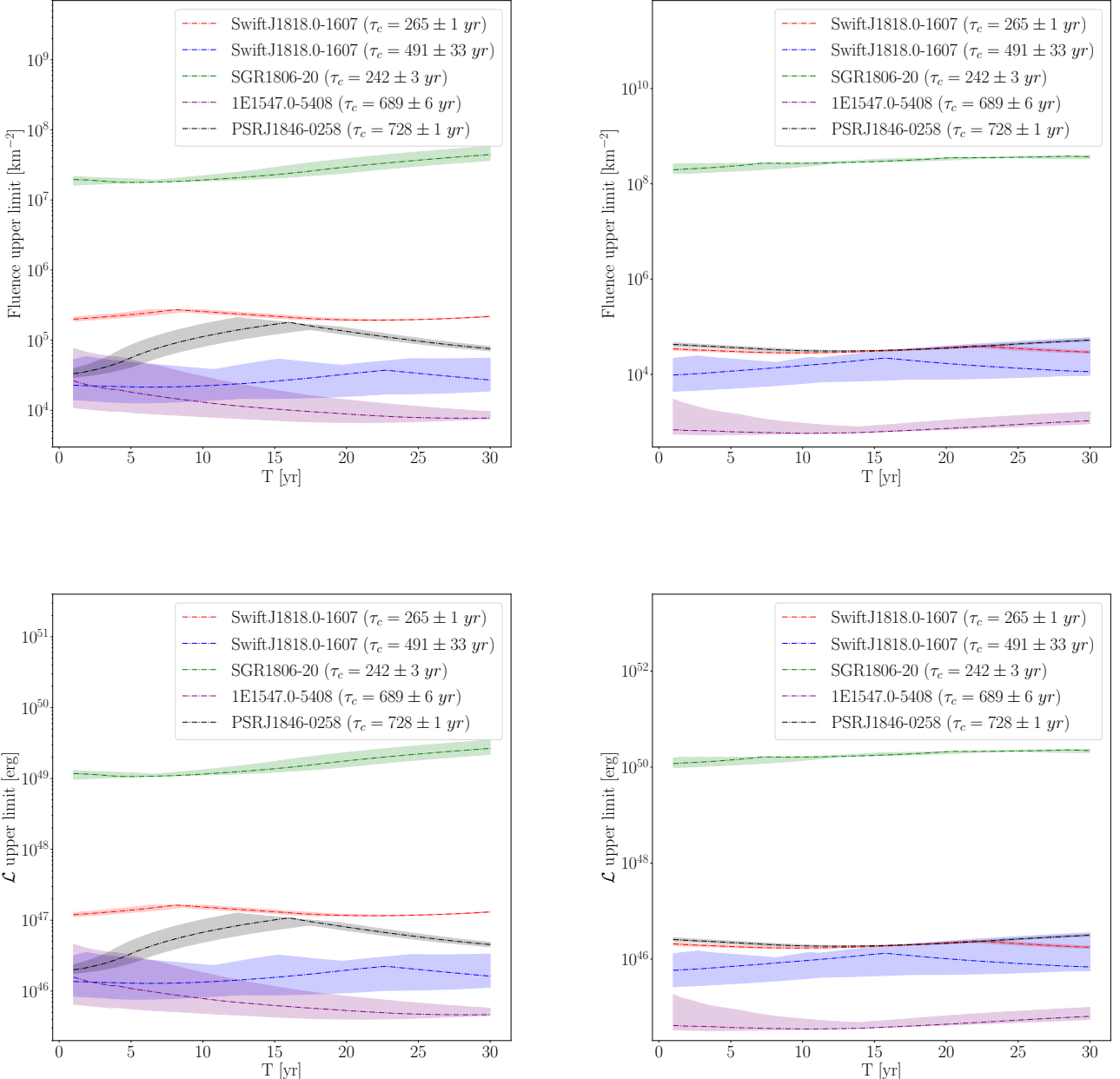


Figure 5.8: Same as fig. 5.5 but in the continuous emission scenario expressed by eq. (4.11) with $\gamma = 6$

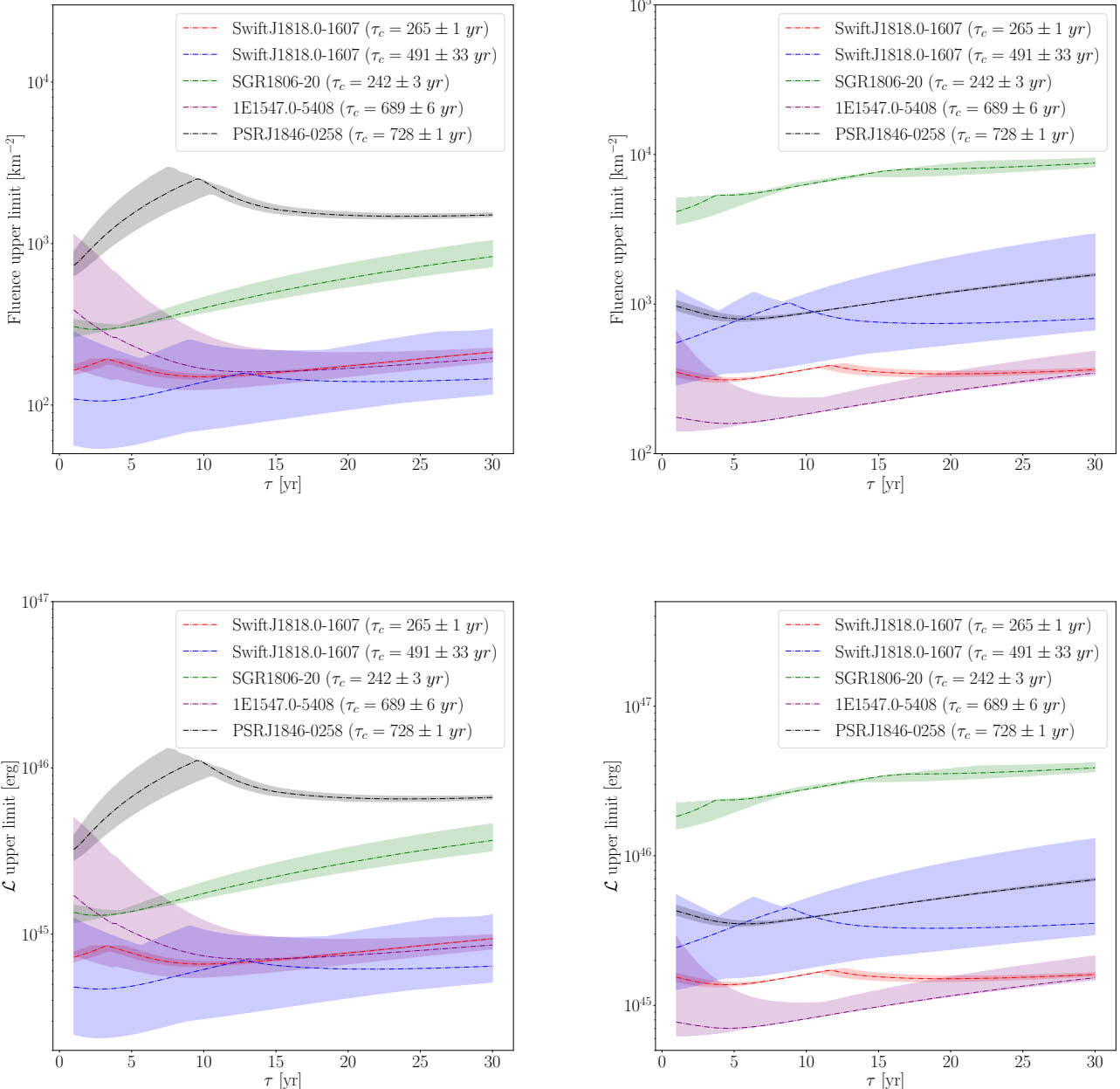


Figure 5.9: Same as fig. 5.5 but in the emission scenario described by a decay law in time expressed by Eq. eq. (4.12) with $\gamma = 2$

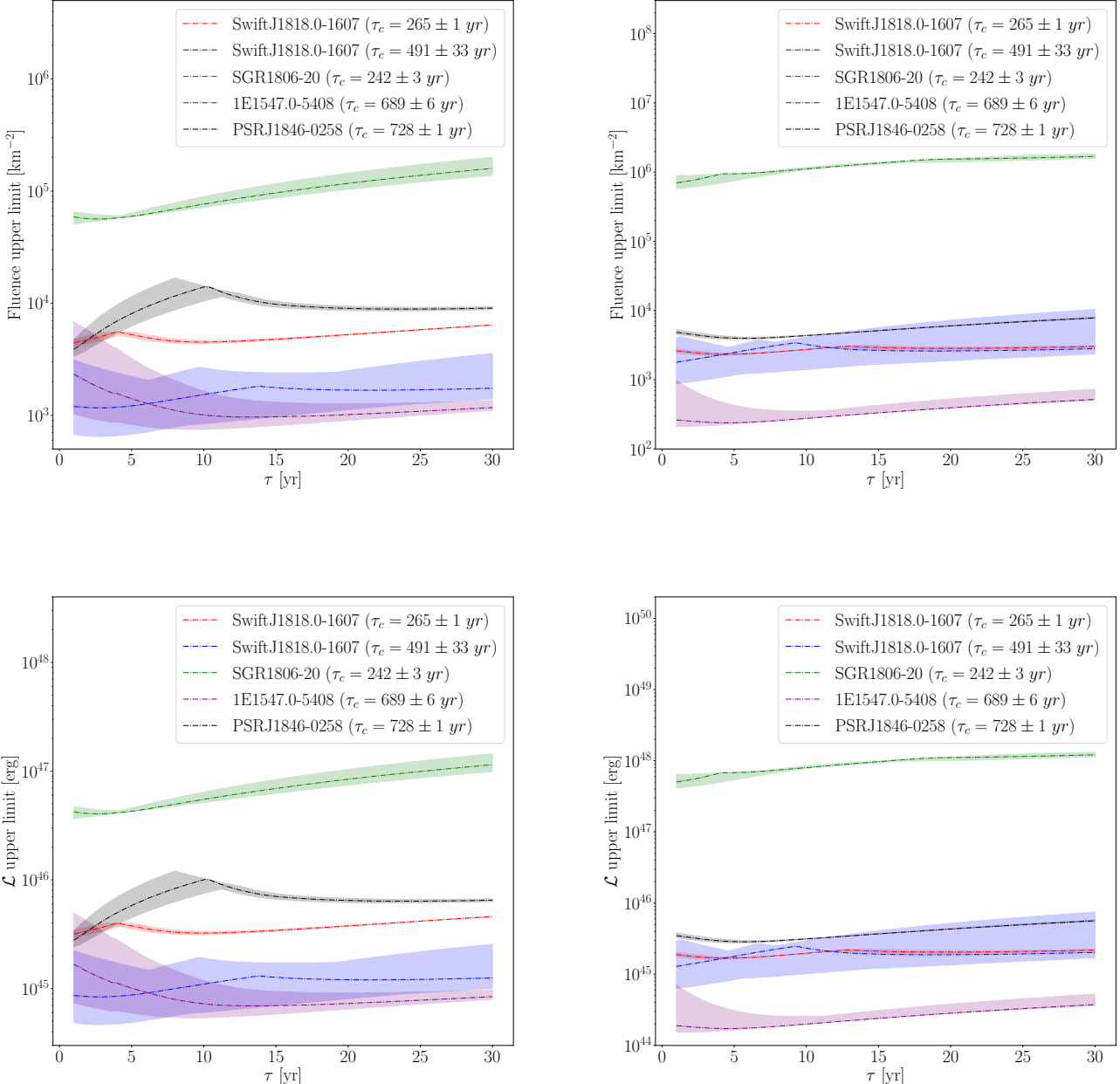


Figure 5.10: Same as fig. 5.5 but in the emission scenario described by a decay law in time expressed by eq. (4.12) with $\gamma = 4$

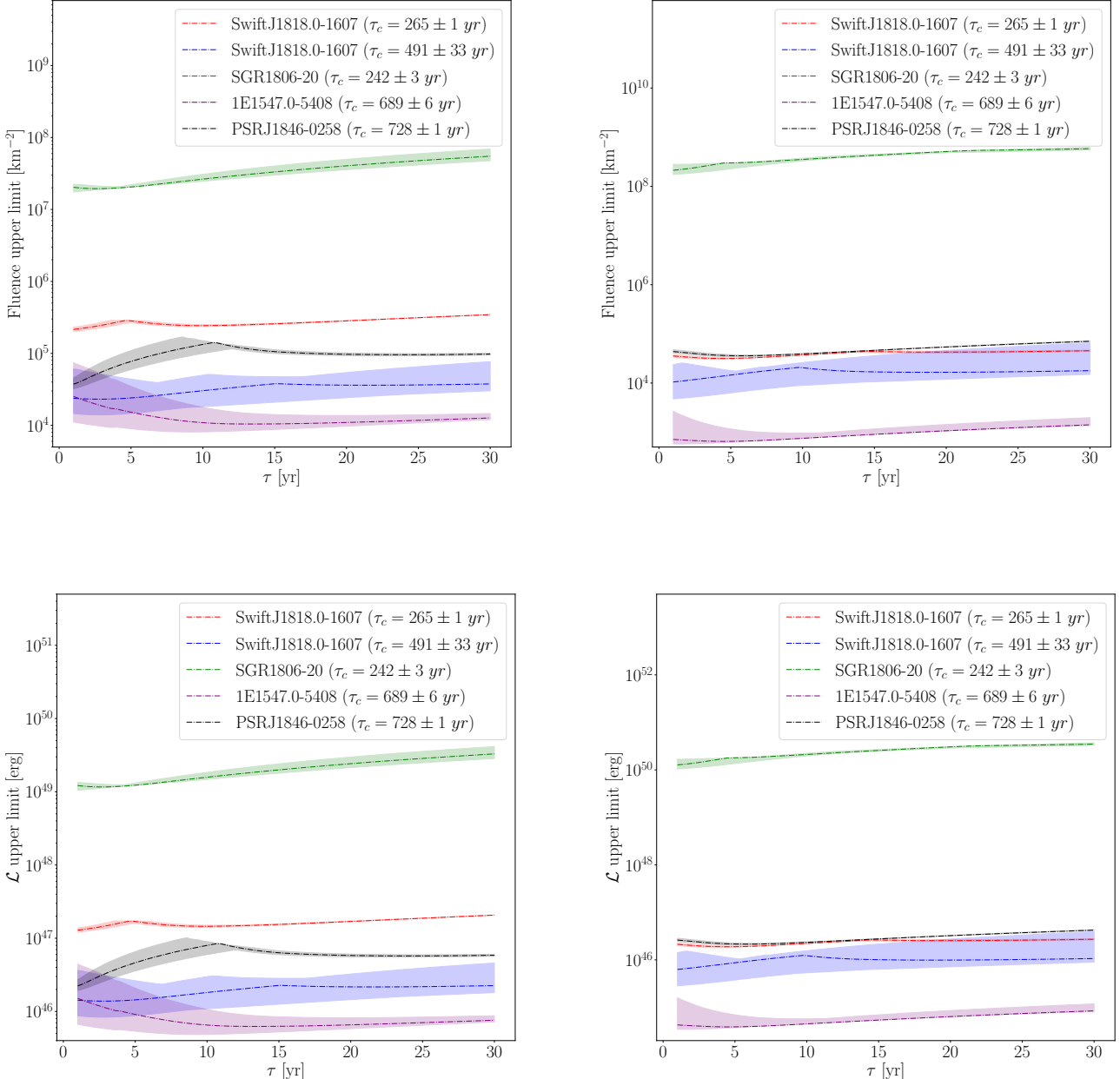


Figure 5.11: Same as fig. 5.5 but in the emission scenario described by a decay law in time expressed by eq. (4.12) with $\gamma = 6$

Chapter 6

Limits on extra-galactic magnetars

In this chapter we compare the results obtained through simulations with the ones obtained in the combined fit performed by the Auger Collaboration [50] (for a detailed description see section 2.3). The goal is to understand which is the lower limit on magnetar birth rate needed to reproduce the observed UHECR spectrum. Conversely, it is also possible to impose a birth rate and observe which is the upper limit on the fraction of cosmic ray energy observed in the spectrum at Earth that could be originated by magnetars.

6.1 Auger results

In this section I present the results of the combined fit performed by the Auger Collaboration, resuming the description made in section 2.3. The fit has been performed assuming the following equation

$$\tilde{Q}_A = \tilde{Q}_{0A} \left(\frac{E}{E_0} \right)^{-\gamma} \begin{cases} \frac{1}{\exp(1 - \frac{E}{Z_A E_{\text{cut}}})} & E \leq Z_A E_{\text{cut}} \\ otherwise & \end{cases}, \quad (6.1)$$

where \tilde{Q}_A describes the spectrum emitted for particles with mass number A per comoving volume, per time and it is expressed in $\text{eV}^{-1} \text{Mpc}^{-3} \text{yr}^{-1}$. The emission for all the particles is given by $\tilde{Q} = \sum \tilde{Q}_A$. E_0 has been arbitrarily set to 10^{18} eV . In this model the free parameters are γ , E_{cut} and \tilde{Q}_{0A} . Therefore considering n atomic species, the total number of free parameters is $2 + n$.

The results of the fit are reported in table 6.2. Instead of \tilde{Q}_{0A} it has been reported the total source emissivity, defined as

$$\mathcal{L}_0 = \sum_A \int_{E_0}^{\infty} E \tilde{Q}_A(E) dE, \quad (6.2)$$

and the fractions I_A , which are defined as

$$I_A = \frac{\int_{E_0}^{\infty} E \tilde{Q}_A(E) dE}{\mathcal{L}_0} \quad (6.3)$$

	SCENARIO 1		SCENARIO 2	
EG components	LE	HE	LE	HE
$\mathcal{L}_0 [10^{44} \text{ erg Mpc}^{-3} \text{ yr}^{-1}]$	6.54 ± 0.36	5.00 ± 0.35	11.35 ± 0.15	5.07 ± 0.06
γ	3.34 ± 0.07	-1.47 ± 0.13	3.52 ± 0.03	-1.99 ± 0.11
$\log_{10}(E_{\text{cut}}/\text{eV})$	> 19.3	18.19 ± 0.02	> 19.4	18.15 ± 0.01
$I_{\text{H}} (\%)$	100	0.0 ± 0.0	48.7 ± 0.3	0.0 ± 0.0
$I_{\text{He}} (\%)$	-	24.5 ± 3.0	7.3 ± 0.4	23.6 ± 1.6
$I_{\text{N}} (\%)$	-	68.1 ± 5.0	44.0 ± 0.4	72.1 ± 3.3
$I_{\text{Si}} (\%)$	-	4.9 ± 3.9	0.0 ± 0.0	1.3 ± 1.3
$I_{\text{Fe}} (\%)$	-	2.5 ± 0.2	0.0 ± 0.0	3.1 ± 1.3

Table 6.1: Results of the combined fit performed by the Auger Collaboration

As can be seen in table 6.2, the fit has been performed in two scenarios. In first scenario the behaviour of the UHECR spectrum is explained with the presence of a galactic component and two extra-galactic component, one of low energy and one of high energy. The spectrum at Earth of the galactic component has the same behaviour as eq. (6.1) with $J_0 = (1.06 \pm 0.04) \times 10^{-13} \text{ eV}^{-1} \text{ km}^{-2} \text{ sr}^{-1} \text{ yr}^{-1}$ and $\log_{10}(E_{\text{cut}}) = 17.48 \pm 0.02$. In this scenario the low energy contribution is completely dominated by protons, while heavier nuclei contribute only in the high energy component.

On the other hand, the second scenario assumes that the ankle is formed by the superposition of two extra-galactic components, while a possible Galactic contribution is subdominant in the considered energy range. As can be seen in table 6.2, the spectral parameters in both energy ranges, as well as the composition of the HE one, are similar to those found in the previous scenario, while the composition of the LE component is a mix of mostly protons and nitrogen.

6.2 Magnetar rate

To obtain the lower limit on the magnetar birth rate, we suppose an emission model equal to the one obtained with the combined fit. Therefore, we have to modify eqs. (4.10) to (4.12) in order to add a cut-off in energy. The modified equations can be written as

$$\frac{dN}{dE} = R_0 \times \tilde{f}(E, \gamma) = R_0 \left(\frac{E}{E_0} \right)^{-\gamma} \begin{cases} 1 & E \leq Z_A E_{\text{cut}} \\ \exp(1 - \frac{E}{Z_A E_{\text{cut}}}) & \text{otherwise} \end{cases}, \quad (6.4)$$

$$\frac{dN}{dEdt} = \begin{cases} R_0 \times g(t, T) \times \tilde{f}(E, \gamma) = R_0 \times \frac{1}{T} \times \tilde{f}(E, \gamma) & 0 < t < T \\ 0 & \text{otherwise} \end{cases}, \quad (6.5)$$

$$\frac{dN}{dEdt} = R_0 \times h(t, \tau) \times \tilde{f}(E, \gamma) = R_0 \times \frac{e^{-\frac{t}{\tau}}}{\tau} \times \tilde{f}(E, \gamma). \quad (6.6)$$

In this model the free parameters R_0 is measured in eV $^{-1}$.

The above equations express the spectrum emitted by an isolated magnetar, to account for all the magnetars which can contribute to the observed UHECR flux at the Earth we have to multiply for the density of galaxy (n_g) and the magnetar birth rate in the singular galaxies (ν_m)

$$\tilde{Q}_m = n_g \times \nu_m \times \frac{dN}{dE}. \quad (6.7)$$

This equation expresses the spectrum of UHECRs emitted in the Universe by the magnetars per comoving space per year, and it can be confronted with the one expressed in eq. (6.1).

The value of n_g is set considering that inside a radius of 250 Mpc of distance to the Earth, compatible with the GZK distance, we have $\sim 44\,000$ galaxies. The value of ν_m is left as target of the analysis.

Considering the results of the combined fit we can set the value of γ and E_{cut} . Therefore, repeating the procedure made in the previous chapter, we can find upper limit on R_0 in the various emission models. One last step to confront the results is to consider that the simulations were completed just using protons, therefore we have to find the value of \tilde{Q}_{0H} from the combined fit.

After having found \tilde{Q}_{0H} we could compare the result of the combined fit with the upper limit obtained with the simulations, since

$$\tilde{Q}_{0H} = n_g \nu_m R_0. \quad (6.8)$$

Inverting the equation and taking the upper limit on R_0 we find the lower limit on ν_m

$$\nu_m = \frac{\tilde{Q}_{0H}}{n_g R_0}. \quad (6.9)$$

This analysis can be completed both for the instantaneous emission model and for the time-dependent ones, considering both the error associated to the age of the magnetar and the error obtained in the combined fit.

The analysis has been performed considering the most promising magnetar as UHECR accelerator, which is SGR 1806-20, both for PT11 and JF12.

In the case of instantaneous emission the results reported in table 6.2 are obtained. The best results is obtained for JF12 in the second scenario where it would be sufficient 3.1 magnetars per year in a galaxy to sustain the UHECR flux observed at the Earth. However this is a number physically unlikely, since the rate of SN in a galaxy has been estimated to be ~ 0.03 yr $^{-1}$. The analysis has been completed also for the time-dependent emission models and the results are reported in fig. 6.2. The lower limit on magnetar birth rate needed decreases with the time parameters, however it does not reach realistic values: the best value is obtained for the SCENARIO 2 in the emission model going as a decay law with JF12 and it is equal to ~ 1 yr $^{-1}$, which is a value still physically unlikely.

This analysis can be inverted to find the upper limit on the fraction of cosmic ray energy that could be emitted by magnetars. In fact, since the birth rate found are

	ν_m lower limit [yr^{-1}]		f_E upper limit [%]	
	SCENARIO 1	SCENARIO 2	SCENARIO 1	SCENARIO 2
PT11	69^{+6}_{-11}	34^{+3}_{-6}	$0.0012^{+0.0001}_{-0.0002}$	$0.0023^{+0.0002}_{-0.0004}$
JF12	$6.1^{+1.8}_{-1.0}$	$3.1^{+0.9}_{-0.5}$	$0.014^{+0.004}_{-0.002}$	$0.026^{+0.007}_{-0.004}$

Table 6.2: Values of ν_m lower limit and f_E upper limit obtained from the simulations in PT11 and JF12 considering both the scenarios of the combined fit

bigger than the estimated SN rate by two order of magnitude, we can set a reasonable number and find the emissivity that could be linked to magnetars, considering the results of the combined fit. Starting from the SN rate in the galaxies ($\sim 0.03 \text{ yr}^{-1}$), we can suppose that half of the SN should become a neutron stars and that $\sim 10\%$ of these should become magnetars. Therefore the magnetar birth rate is $\nu_m = 1.5 \times 10^{-3} \text{ yr}^{-1}$. Now we can define the upper limit on the emissivity

$$\mathcal{L}_s = n_g \nu_m \int_{E_0}^{\infty} \frac{dN}{dE} E dE, \quad (6.10)$$

where we take the upper limit on R_0 in order to evaluate dN/dE .

Therefore, the upper limit on the energy fraction is $\mathcal{L}_s/\mathcal{L}_{0H}$, where \mathcal{L}_{0H} is the combined fit emissivity obtained for hydrogen.

The results for the upper limit on the energy fraction in the instantaneous emission model are reported in table 6.2. The optimal scenario is the second one in JF12 where the magnetars can contribute to the UHECR energy just up to the 0.026%. The upper limit on the energy fraction increases in the emission model time dependent, as can be seen in fig. 6.2, but it remains in the same order of magnitude of the instantaneous model. Also in this analysis the best results is obtained for the second scenario in JF12 for the emission model going as a decay law, where f_E reaches $\sim 0.07\%$.

The analysis completed considers that magnetars have only proton emission, however this is not necessarily true. We therefore studied the birth rate lower limit considering an emission of heavier nuclei. Keeping the upper limits of SGR 1806-20 we evaluated the limit in SCENARIO 2, where the combined fit foresees a multi-species composition of the UHECR spectrum at lower energies. We repeated the analysis considering both helium and lithium emission and found that, in the best case, the magnetar rate decreases to $\sim 0.5 \text{ yr}^{-1}$. This is still a non physical value, incompatible with the expected birth rate in a galaxy ($\sim 1.5 \text{ yr}^{-1}$).

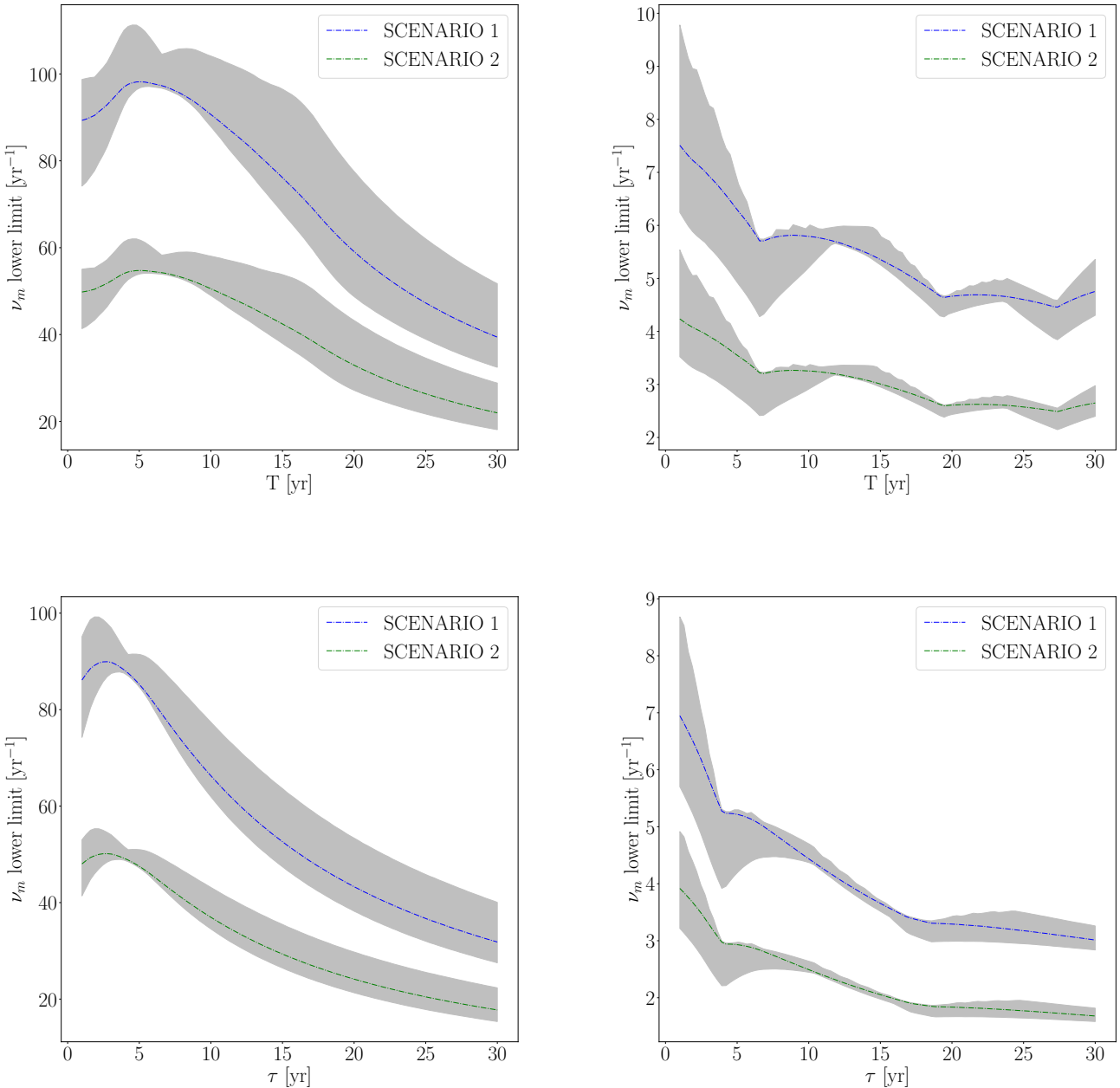


Figure 6.1: **Top:** Magnetar birth rate lower limit plots obtained for the continuous emission model expressed in eq. (6.5) as a function of the time parameter T for PT11 (left) and JF12 (right). **Bottom:** Same as above but for the emission model that goes as a decay law in time, expressed in eq. (6.6)

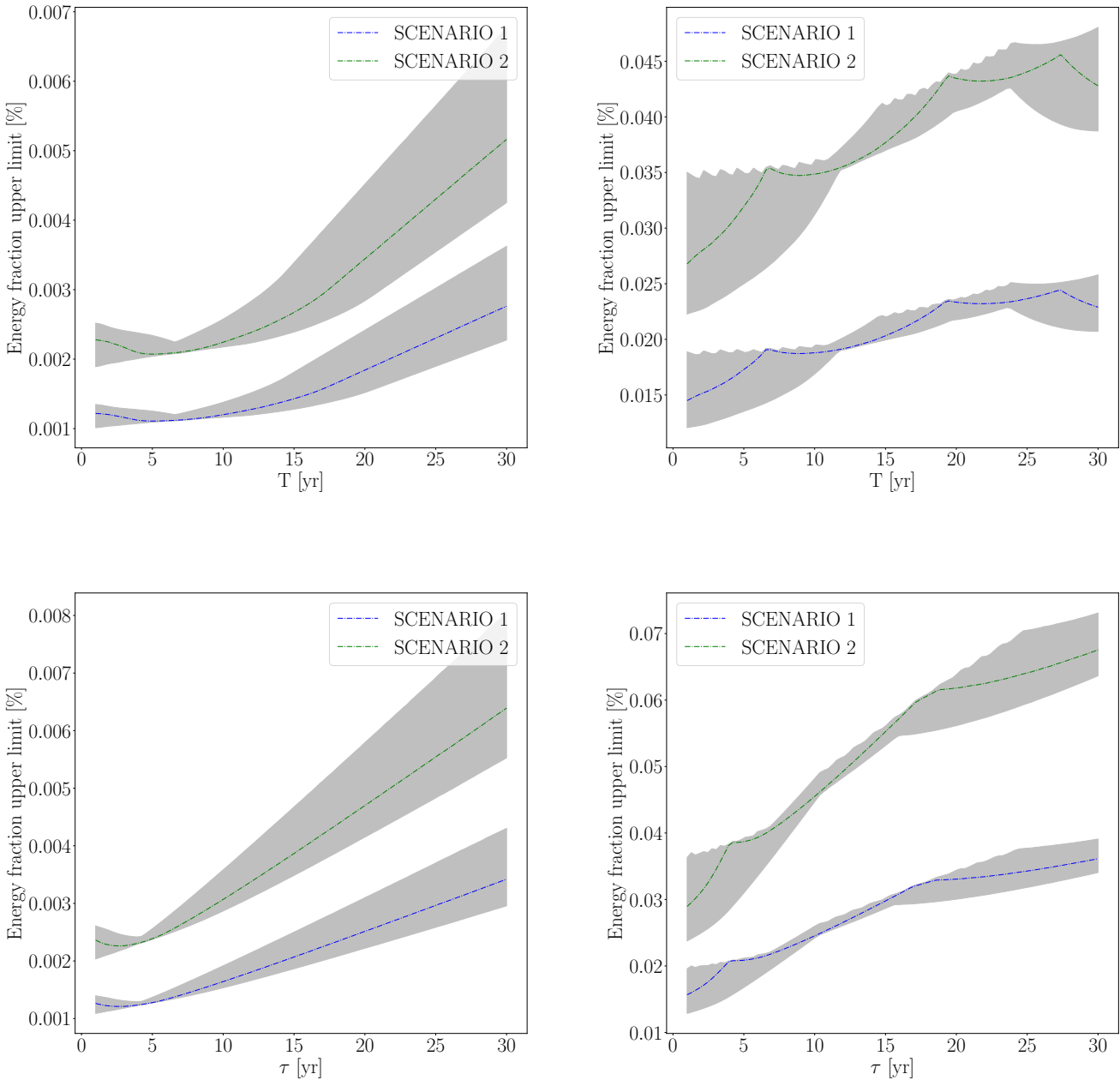


Figure 6.2: Same as fig. 6.1 but for the upper limit on the energy fraction

Chapter 7

Conclusion

With this thesis we have put limits on the UHECR emission made by known magnetars inside of our Galaxy, using the data collected by the Pierre Auger Observatory. The signal coming from each magnetar has been chosen defining a sky region around the neutron star and looking for the upper limit in the Auger data.

We considered two possible emission scenario: one based on the theoretical model proposed by J. Arons in 2003 [64]. This model considers highly rotating magnetars as UHECR emitter at birth. However confronting the parameter predicted by the model and the parameter obtained from the Auger data we have shown that, for the selected Galactic magnetars, the two are incompatible. The parameters of the Auger data are orders of magnitude less than the one obtained in Arons model, considering the present magnetic field of the magnetar. This result does not exclude the Arons model, but strongly neglect that the chosen Galactic magnetars emitted as it has been predicted.

In the second scenario we considered a more general emission model going as a power law in function of the energy, combined with three models in time: an instantaneous emission scenario at birth, a continuous emission for a limited period of time and a model that goes as a decay law in time. We therefore studied the upper limit on fluence at 5 kpc, which is obtained by the Auger data for all the selected magnetars. In the instant emission model the fluence upper limit can be expressed as a function of the spectral index γ , in the emission models time-dependent it is expressed as a function of the time parameter setting the value of γ . The fluence upper limit grows with the spectral index, and that is valid for all the magnetars and all the emission scenarios. However, in the case of the time-dependent emission models it is roughly constant for all the time parameters.

In this section it has been also shown the luminosity upper limit plot. The luminosity is the total energy emitted in cosmic rays by the magnetar in the considered model. Its upper limit increases as a function of γ and for high value ($\gamma = 6$) it reaches $\mathcal{O}(10^{50})$ erg, which is an intense energy value (it is approximately one thousandth of the energy emitted by a core-collapse supernova). However $\gamma = 6$ is an unphysical value since the spectral index in the UHECR spectrum observed at the Earth is ~ 2.7 .

We can now combine the results obtained with both PT11 and JF12 to find the

complete upper limits for the fluence and the luminosity. The upper limit of the combined galactic magnetic fields is defined taking the maximum value between the PT11 result and the JF12 one (i.e. comparing the largest values in the age range analyzed). The final results are shown in figs. 7.1 to 7.4.

In the last part of this work, we have considered the magnetars as extra-galactic sources of cosmic rays, and evaluated the lower limit on their birth rate in galaxies, in order to recreate the observed cosmic ray flux at the Earth. In doing this, we started from the combined fit performed by the Auger Collaboration [50]. We considered an emission model going as the one of the combined fit in which we added the galaxy density (n_g), as measured by the 2MASS catalogue considering a maximum distance to Earth of 250 Mpc, and the magnetar birth rate per galaxy (ν_m), left as a free parameter. Now using the results obtained for SGR 1806-20 we estimated the lower limit ν_m . The best result of the instantaneous emission model is $\nu_m = 3.1 \text{ yr}^{-1}$, which decreases, if we consider an emission model going as a decay law in time, as a function of the decay constant, reaching $\sim 1 \text{ yr}^{-1}$. All this rates are very intense and incompatible with the expected number of magnetars per year in a galaxy $\sim 1.5 \times 10^{-3} \text{ yr}^{-1}$. From the data collected by Auger it seems very unlikely for magnetars to be the main sources in UHECR acceleration, even considering the best scenario possible.

In the last analysis, instead of looking for the birth rate, we set a realistic value of ν_m and found the upper limit on the fraction of energy in the UHECR spectrum that can be justified by magnetars. We imposed $\nu_m = 1.5 \text{ yr}^{-1}$, considering that half of the supernova becomes neutron stars and that 10% of them should become magnetars. We studied both the instantaneous emission and the time-dependent emission finding that the best value is 0.026% in the instantaneous emission case, while the best value for the time-dependent scenarios is for the one going as a decay law, and increases as a function of the decay constant, reaching $\sim 0.07\%$. In conclusion it seems that even considering the best emission model, magnetars can contribute to less than one thousandth of the UHECR energy.

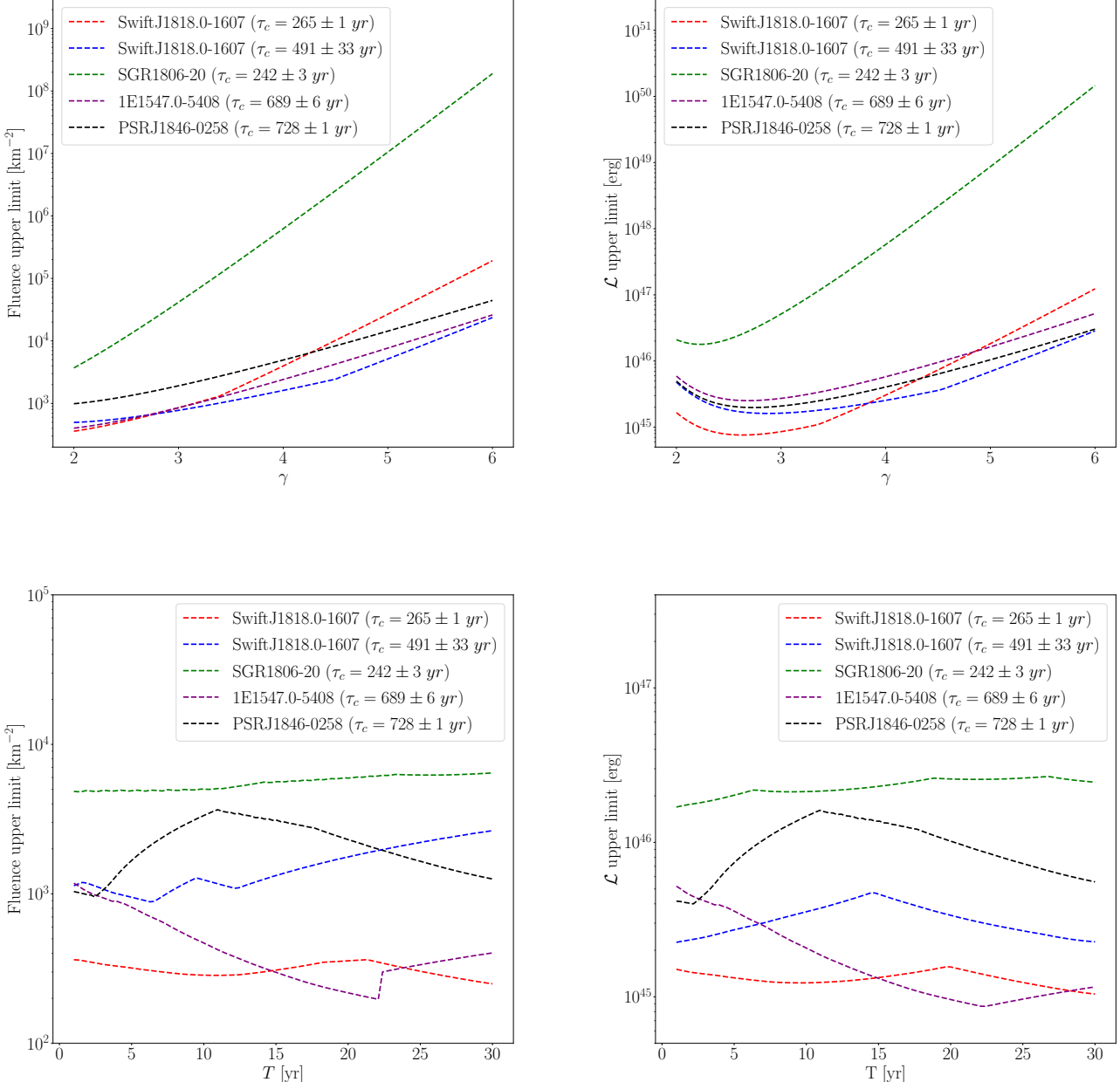


Figure 7.1: **Top:** Upper limits obtained combining the results of PT11 and JF12 for the fluence (left) and the luminosity (right) in the case of an instantaneous emission model. **Bottom:** same as above but in the continuous emission scenario described by eq. (4.10) with $\gamma = 2$

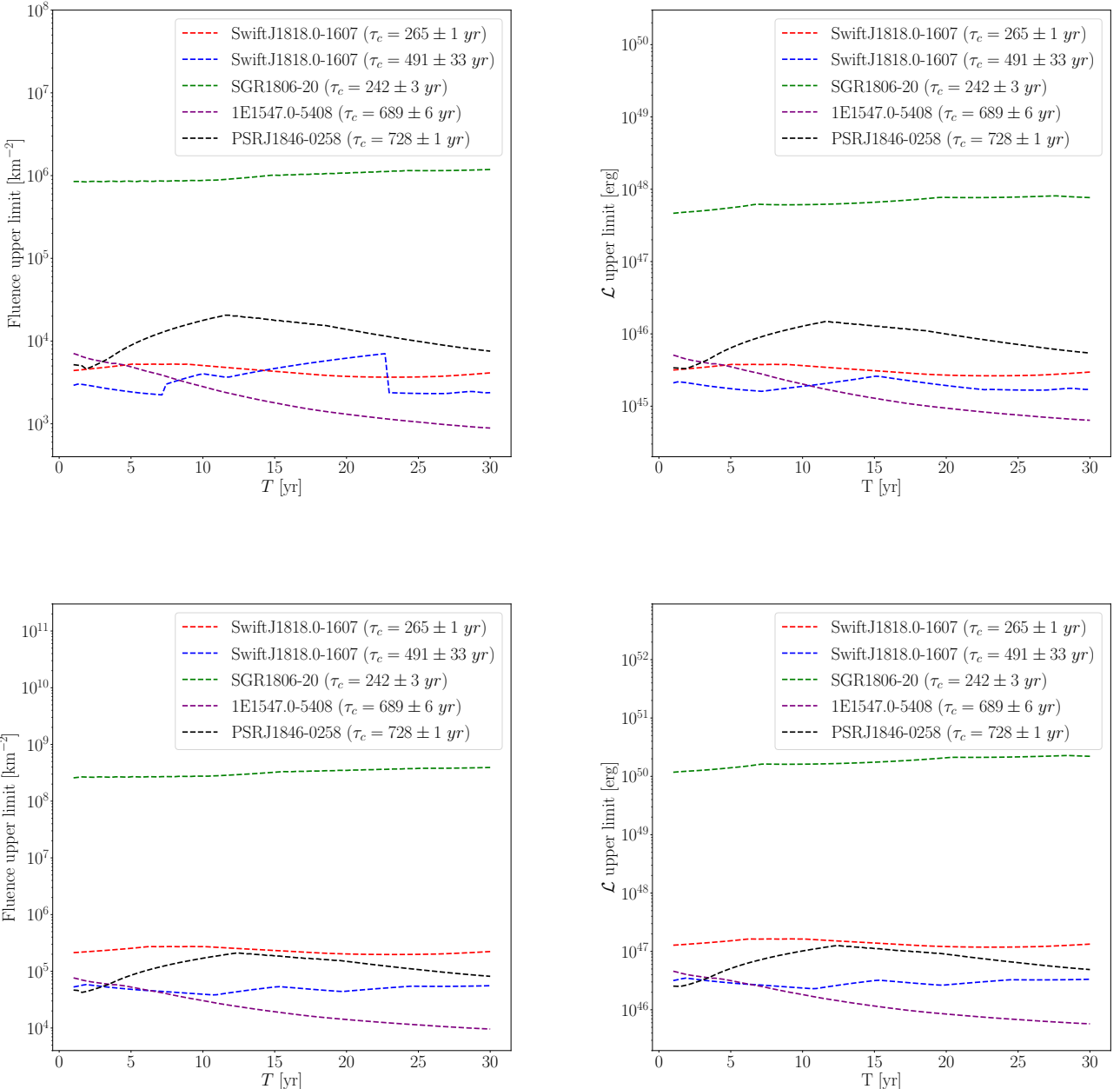


Figure 7.2: Same as fig. 7.1 but for the continuous emission scenario described by eq. (4.10) with $\gamma = 4$ (top) and $\gamma = 6$ (bottom)

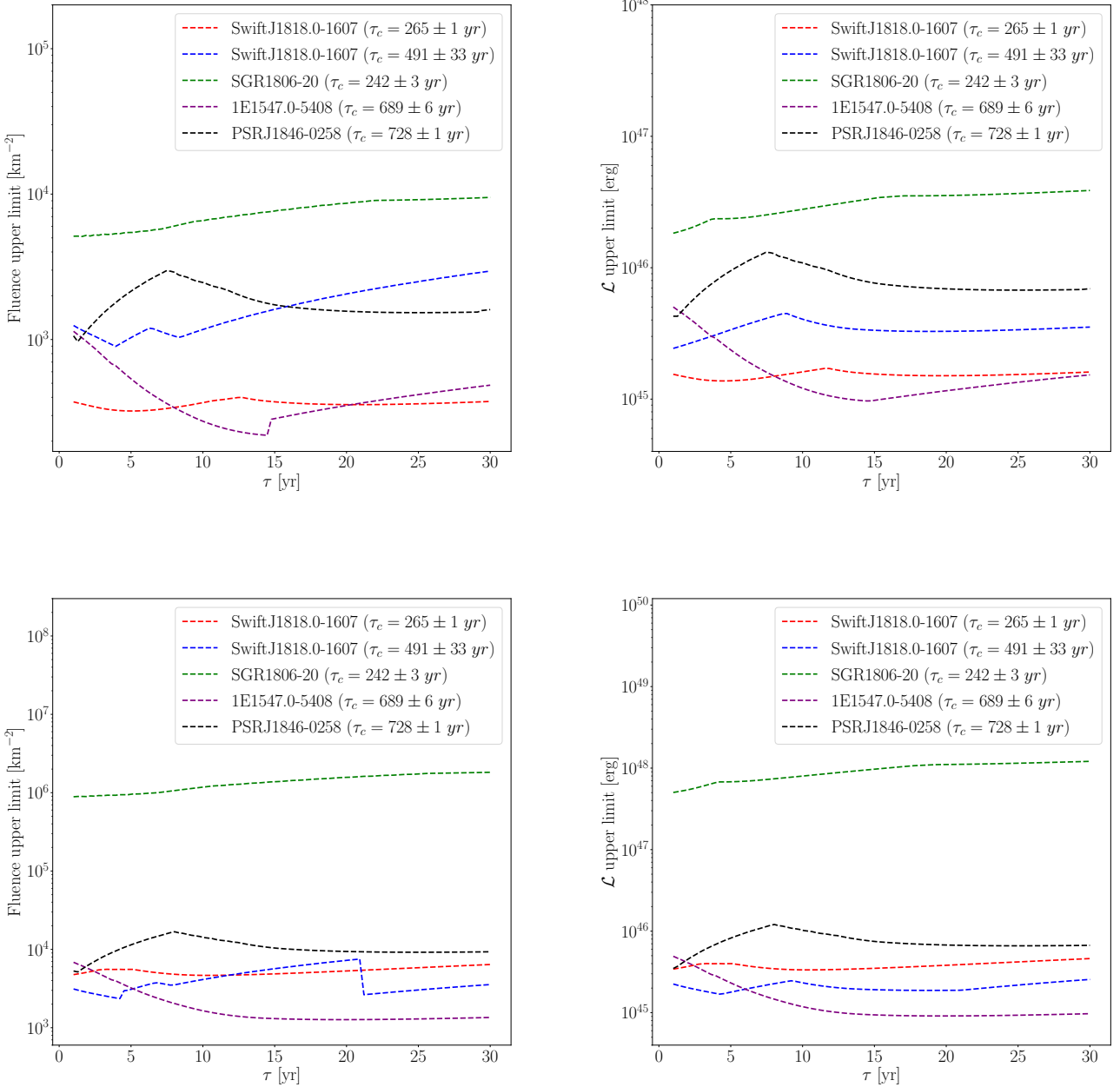


Figure 7.3: Same as fig. 7.1 but for the emission scenario going as a decay law described by eq. (4.11) with $\gamma = 2$ (top) and $\gamma = 4$ (bottom)

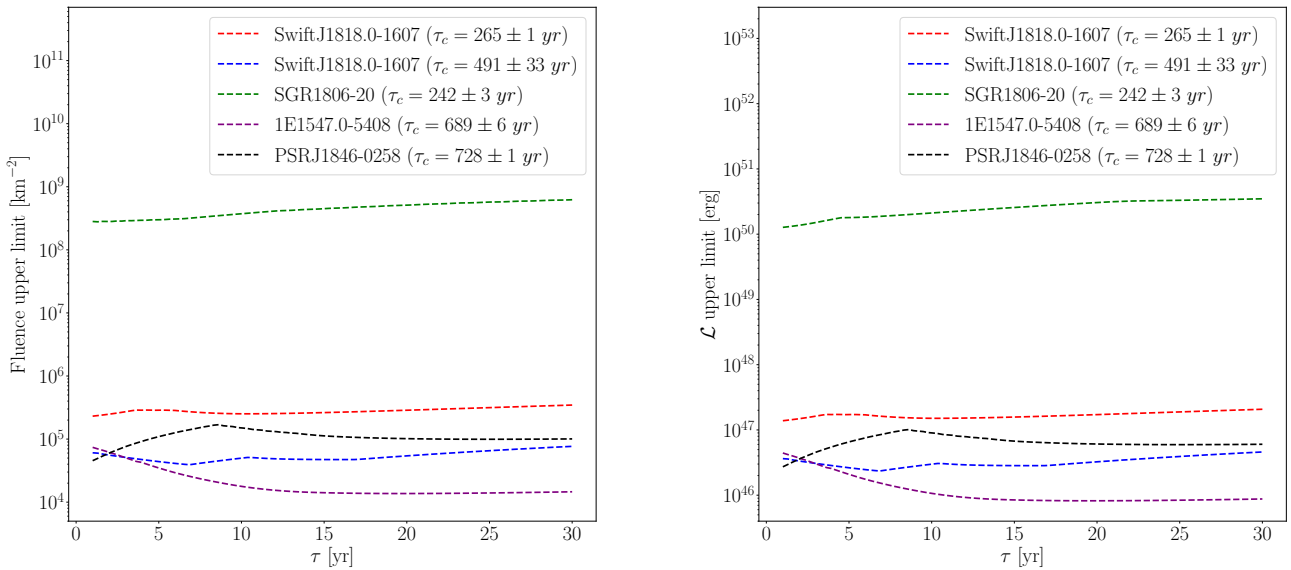


Figure 7.4: Same as fig. 7.1 but for the emission scenario going as a decay law described by eq. (4.11) with $\gamma = 6$

Bibliography

- [1] V. Hess. On the observations of the penetrating radiation during seven balloon flights, 1912.
- [2] M. T. Dova. Ultra-High-Energy Cosmic Rays, 2015.
- [3] E. Amato. The origin of galactic cosmic rays. *International Journal of Modern Physics D*, 23(07):1430013, jun 2014.
- [4] M. Ackermann et al. Detection of the Characteristic Pion-Decay Signature in Supernova Remnants. *Science*, 339(6121):807–811, feb 2013.
- [5] The Pierre Auger collaboration. Observation of a large-scale anisotropy in the arrival directions of cosmic rays above 8×10^{18} eV. *Science*, 357(6357):1266–1270, sep 2017.
- [6] K. Lodders, H. Palme, and H. P. Gail. 4.4 Abundances of the elements in the Solar System. In *Solar System*, pages 712–770. Springer Berlin Heidelberg, 2009.
- [7] J. J. Engelmann et al. Charge composition and energy spectra of cosmic-ray nuclei for elements from Be to Ni - Results from HEAO-3-C2. *Astronomy and Astrophysics*, 233:96–111, jul 1990.
- [8] N. Prantzos. Production and evolution of li, be, and b isotopes in the galaxy. *Astronomy and Astrophysics*, 542:A67, jun 2012.
- [9] E. Fermi. Galactic magnetic fields and the origin of cosmic radiation. *Astrophysical Journal*, 119:1, jan 1954.
- [10] J. L. Han, R. N. Manchester, W. van Straten, and P. Demorest. Pulsar Rotation Measures and Large-scale Magnetic Field Reversals in the Galactic Disk. *The Astrophysical Journal Supplement Series*, 234(1):11, jan 2018.
- [11] M. Haverkorn. Magnetic Fields in the Milky Way. In *Astrophysics and Space Science Library*, pages 483–506. Springer Berlin Heidelberg, oct 2014.
- [12] M. S. Pshirkov, P. G. Tinyakov, and F. R. Urban. New Limits on Extragalactic Magnetic Fields from Rotation Measures. *Physical Review Letters*, 116(19), may 2016.

- [13] A. A. Penzias and R. W. Wilson. A Measurement of Excess Antenna Temperature at 4080 Mc/s. *The Astrophysical Journal*, 142:419–421, jul 1965.
- [14] D. J. Fixsen. The Temperature of the Cosmic Microwave Background. *The Astrophysical Journal*, 707(2):916–920, nov 2009.
- [15] Particle Data Group et al. Review of Particle Physics. *Progress of Theoretical and Experimental Physics*, 2020(8):083C01, 08 2020.
- [16] K. Greisen. End to the Cosmic-Ray Spectrum? *Phys. Rev. Lett.*, 16:748–750, Apr 1966.
- [17] V. A. Kuz'min G. T. Zatsepin. Upper Limit of the Spectrum of Cosmic Rays. *Soviet Journal of Experimental and Theoretical Physics Letters*, 4:78, Aug 1966.
- [18] R. Aloisio, V. Berezhinsky, and S. Grigorieva. Analytic calculations of the spectra of ultra high energy cosmic ray nuclei. II. The general case of background radiation. *Astroparticle Physics*, 41:94–107, jan 2013.
- [19] E. Fermi. On the Origin of the Cosmic Radiation. *Phys. Rev.*, 75:1169–1174, Apr 1949.
- [20] M. Bustamante et al. High-energy cosmic-ray acceleration. *CERN - Latin-American School of High-Energy Physics*, pages 533–540, 2009.
- [21] M. G. Aartsen et al. Astrophysical Neutrinos and Cosmic Rays Observed by IceCube. *Advances in Space Research*, 62, 05 2017.
- [22] G. Ghisellini, G. Ghirlanda, F. Tavecchio, F. Fraternali, and G. Pareschi. Ultra-high energy cosmic rays, spiral galaxies and magnetars. *Monthly Notices of the Royal Astronomical Society: Letters*, 390(1):L88–L92, oct 2008.
- [23] L. A. Anchordoqui. Acceleration of ultrahigh-energy cosmic rays in starburst superwinds. *Physical Review D*, 97(6), mar 2018.
- [24] V. Beckmann and C. R. Shrader. *Active Galactic Nuclei*. 2012.
- [25] A. M. Hillas. The Origin of Ultra-High-Energy Cosmic Rays. *Annual review of astronomy and astrophysics*, 22:425–444, jan 1984.
- [26] V. L. Ginzburg and S. I. Syrovatskii. Origin of Cosmic Rays. *Soviet Physics Uspekhi*, 9(2):223, feb 1966.
- [27] B. L. Fanaroff and J. M. Riley. The morphology of extragalactic radio sources of high and low luminosity. *Monthly Notices of the Royal Astronomical Society*, 167:31P–36P, May 1974.
- [28] K. Kotera and A. V. Olinto. The Astrophysics of Ultrahigh-Energy Cosmic Rays. *Annual Review of Astronomy and Astrophysics*, 49(1):119–153, sep 2011.
- [29] W. Heitler. *Quantum Theory of Radiation*. Oxford University Press, 1944.

- [30] V. S. Kaushik. Electromagnetic Showers and Shower Detectors. 2002.
- [31] J. J. Matthews. A Heitler model of extensive air showers. *Astroparticle Physics*, 22(5-6):387–397, jan 2005.
- [32] Mario Pecimotika. *Transmittance Simulations for the Atmosphere with Clouds*. PhD thesis, 11 2018.
- [33] B. Rossi and K. Greisen. Cosmic-Ray Theory. *Rev. Mod. Phys.*, 13:240–309, oct 1941.
- [34] A. Haungs, H. Rebel, and M. Roth. Energy spectrum and mass composition of high-energy cosmic rays. *Reports on Progress in Physics*, 66(7):1145, jun 2003.
- [35] The Pierre Auger Collaboration. The Pierre Auger Cosmic Ray Observatory. *Nuclear Instruments and Methods in Physics Research Section A: Accelerators, Spectrometers, Detectors and Associated Equipment*, 798:172–213, oct 2015.
- [36] G. Dariusz. The Pierre Auger Observatory: Review of Latest Results and Perspectives. *Universe*, 4(11):128, nov 2018.
- [37] I. C. Maris and The Pierre Auger Collaboration. The AMIGA infill detector of the Pierre Auger Observatory: performance and first data. 2011.
- [38] F. Sanchez and The Pierre Auger Collaboration. The AMIGA detector of the Pierre Auger Observatory: an overview. 2011.
- [39] E. Parizot. The Pierre Auger Observatory: status, results and perspective, sep 2007.
- [40] The Pierre Auger Collaboration. The fluorescence detector of the Pierre Auger Observatory. *Nuclear Instruments and Methods in Physics Research Section A: Accelerators, Spectrometers, Detectors and Associated Equipment*, 620(2-3):227–251, aug 2010.
- [41] Valerio Verzi. The Energy Scale of the Pierre Auger Observatory. In *33rd International Cosmic Ray Conference*, page 0928, 2013.
- [42] M. J. Tueros. Estimate of the Non-calorimetric Energy of Showers Observed with the Fluorescence and Surface Detectors of the Pierre Auger Observatory. In *International Cosmic Ray Conference*, volume 33, page 1713, 2013.
- [43] The Pierre Auger collaboration. The energy spectrum of cosmic rays beyond the turn-down around 10^{17} eV as measured with the surface detector of the Pierre Auger Observatory. *The European Physical Journal C*, 81(11), nov 2021.
- [44] The Pierre Auger Collaboration. The second knee in the cosmic ray spectrum observed with the surface detector of the Pierre Auger Observatory. *PoS, ICRC2023:398*, 2023.

- [45] The Pierre Auger Colaboration. Depth of Maximum of Air-Shower Profiles at the Pierre Auger Observatory: Measurements at Energies above $10^{17.8}$ eV. *Physical Review D*, 90(12), dec 2014.
- [46] E. Amato. Cosmic neutrinos of ultra-high energies and detection possibility. *Astrophys Space Sci*, 32:461–482, jun 1975.
- [47] J. Rautenberg. Limits on ultra-high energy photons with the Pierre Auger Observatory. *PoS*, ICRC2019:398, 2021.
- [48] The Pierre Auger Collaboration. Limits on point-like sources of ultra-high-energy neutrinos with the Pierre Auger Observatory. *Journal of Cosmology and Astroparticle Physics*, 2019(11):004, nov 2019.
- [49] The Pierre Auger collaboration. Arrival Directions of Cosmic Rays above 32 EeV from Phase One of the Pierre Auger Observatory. *The Astrophysical Journal*, 935, jun 2022.
- [50] The Pierre Auger Collaboration. Constraining the sources of ultra-high-energy cosmic rays across and above the ankle with the spectrum and composition data measured at the Pierre Auger Observatory. *Journal of Cosmology and Astroparticle Physics*, 2023(05):024, may 2023.
- [51] R. Aloisio, D. Boncioli, A. F. Grillo, S. Petrera, and F. Salamida. SimProp: a simulation code for ultra high energy cosmic ray propagation. *Journal of Cosmology and Astroparticle Physics*, 2012(10):007–007, oct 2012.
- [52] S. L. Shapiro and S. A. Teukolski. *Black holes, white dwarfs and neutron stars. The physics of compact objects*. 1983.
- [53] H. A. Bethe and G. Brown. How a Supernova Explodes. *Scientific American*, 252(5):60–69, 1985.
- [54] R. Nandi and D. Bandyopadhyay. Magnetised Neutron Star Crusts and Torsional Shear Modes of Magnetars. *Journal of Physics: Conference Series*, 420:012144, mar 2013.
- [55] Feryal Özel and Paulo Freire. Masses, Radii, and the Equation of State of Neutron Stars. *Annual Review of Astronomy and Astrophysics*, 54(1):401–440, sep 2016.
- [56] V. M. Kaspi. Grand unification of neutron stars. *Proceedings of the National Academy of Sciences*, 107(16):7147–7152, apr 2010.
- [57] X. Zhou, H. Tong, C. Zhu, and N. Wang. Dependence of pulsar death line on the equation of state. *Monthly Notices of the Royal Astronomical Society*, 472, aug 2017.
- [58] V. M. Kaspi and A. M. Beloborodov. Magnetars. *Annual Review of Astronomy and Astrophysics*, 55(1):261–301, aug 2017.

- [59] C. Kouveliotou, T. Strohmayer, K. Hurley, J. van Paradijs, M. H. Finger, S. Dieters, P. Woods, C. Thompson, and R. C. Duncan. Discovery of a Magnetar Associated with the Soft Gamma Repeater SGR 1900+14. *The Astrophysical Journal*, 510(2):L115–L118, jan 1999.
- [60] R. C. Duncan and C. Thompson. Formation of Very Strongly Magnetized Neutron Stars: Implications for Gamma-Ray Bursts. *The Astrophysical Journal*, 392:L9, June 1992.
- [61] C. Thompson and R. C. Duncan. The soft gamma repeaters as very strongly magnetized neutron stars - I. Radiative mechanism for outbursts. *Monthly Notices of the Royal Astronomical Society*, 275(2):255–300, 07 1995.
- [62] C. Thompson and R. C. Duncan. The Soft Gamma Repeaters as Very Strongly Magnetized Neutron Stars. II. Quiescent Neutrino, X-Ray, and Alfvén Wave Emission. *The Astrophysical Journal*, 473:322, dec 1996.
- [63] P. Goldreich and W. H. Julian. Pulsar Electrodynamics. *The Astrophysical Journal*, 157:869, aug 1969.
- [64] J. Arons. Magnetars in the Metagalaxy: An Origin for Ultra High Energy Cosmic Rays in the Nearby Universe. *The Astrophysical Journal*, 589(2):871–892, jun 2003.
- [65] D. Champion et al. Spin-evolution of the new magnetar J1818.0-1607. *The Astronomer's Telegram*, 13559:1, mar 2020.
- [66] D. Champion et al. High-cadence observations and variable spin behaviour of magnetar Swift J1818.0-1607 after its outburst. *Monthly Notices of the Royal Astronomical Society*, 498(4):6044–6056, sep 2020.
- [67] P. M. Woods et al. The Prelude to and Aftermath of the Giant Flare of 2004 December 27: Persistent and Pulsed X-Ray Properties of SGR 1806-20 from 1993 to 2005. *The Astrophysical Journal*, 654(1):470–486, jan 2007.
- [68] M. A. Livingstone, C. Y. Ng, V. M. Kaspi, F. P. Gavriil, and E. V. Gotthelf. Post-outburst Observations of the Magnetically Active Pulsar J1846-0258: a new braking index, increased timing noise, and radiative recovery. *The Astrophysical Journal*, 730(2):66, mar 2011.
- [69] R. Dib, V. M. Kaspi, P. Scholz, and F. P. Gavriil. RXTE Observations of Anomalous X-ray Pulsar 1E 1547.05408 During and After its 2008 and 2009 Outbursts. *The Astrophysical Journal*, 748(1):3, feb 2012.
- [70] R. A. Batista et al. CRPropa 3.2 – an advanced framework for high-energy particle propagation in extragalactic and galactic spaces. *Journal of Cosmology and Astroparticle Physics*, 2022(09):035, sep 2022.

- [71] M. S. Pshirkov, P. G. Tinyakov, P. P. Kronberg, and K. J. Newton-McGee. Deriving global structure of the Galactic Magnetic Field from Faraday Rotation Measures of extragalactic sources. *The Astrophysical Journal*, 738(2):192, aug 2011.
- [72] R. Jansson and G. R. Farrar. A New Model of the Galactic Magnetic Field. *The Astrophysical Journal*, 757(1):14, aug 2012.
- [73] T. P. Li and Y. Q. Ma. Analysis methods for results in gamma-ray astronomy. *The Astrophysical Journal*, 272:317–324, September 1983.
- [74] G. Zech. Upper limits in experiments with background or measurement errors. *Nuclear Instruments and Methods in Physics Research Section A: Accelerators, Spectrometers, Detec*, 277:808–610, may 1989.

Acknowledgements

At this point, I concluded my work, and with it also my studies at this University degree, but just before the word *end* could be written in this thesis, I would like to spend some more ink (or Bytes if you are reading the PDF version) to thank who helped me in this path.

First of all, I want to thank my supervisor Lorenzo Caccianiga, for his help in all the physical matters concerning this thesis, for his kindness and patience in discussing my future, and for allowing me to continue my path as one of his Ph.D. students.

Another thank you goes to Claudio Galelli, who, despite being in Paris, has been really helpful in the development of this work. His guidance and advice have always been excellent.

I want to give a special and deep thank you to Federico Mariani, who has been vital through these years, capable of giving me his advice and help in every possible situations, physics and non-physics related.

Un grazie va sicuramente ai miei amici, fondamentali nel permettermi di staccare la spina e nel sapermi distrarre nel momento in cui i pensieri per l'Università diventavano pressanti.

Ringrazio poi la mia famiglia, a partire dai miei zii che si sono sempre interessati al mio percorso, so che avrebbero preferito un altro tipo di *dottore*, ma penso siano ugualmente felici delle mie scelte.

Grazie a mia madre per tutte le incalcolabili cose che ha fatto per me nel corso di questi anni, impossibili da riassumere nello spazio di due righe.

E infine grazie a mia sorella Linda, per essere da sempre stella polare della mia vita.